ABSTRACT

Title of Dissertation: ON THE ORIGIN OF HYDROCLIMATE CHANGE OVER CONTINENTS THROUGH SEASONALLY-STRATIFIED TRENDS

Natalie Paige Thomas, Doctor of Philosophy, 2019

Dissertation directed by: Professor Sumant Nigam
Department of Atmospheric and Oceanic Science

Global hydroclimate has undergone significant changes over the twentieth century. Temperature and precipitation changes have not been uniform in space or time and mechanisms driving many continental changes remain to be understood. Annual-mean changes are the most often cited; in this dissertation, trends in hydroclimate variables (specifically, temperature and precipitation) are examined seasonally to gain physical insights. Century-scale seasonal hydroclimate trends are also used as a new metric for evaluation of a subset of leading global climate models informing the Intergovernmental Panel on Climate Change's Fifth Assessment Report (IPCC-AR5).

Surface air temperature (SAT) trends over Northern Hemisphere continental regions are examined first. Warming over the twentieth century is found to exhibit striking seasonality; it is strong in winter and spring and muted in summer and fall. Examined climate models are unable to reproduce the observed SAT trend

seasonality. Two potential mechanisms are explored for explanation of the observed temperature trend seasonality; one relating to changes in winter circulation and one based on summer changes in land-surface-hydroclimate interactions. To further probe the causes of temperature trend seasonality at the surface, seasonal trends in upper-air temperatures are examined from radiosonde data sets and global reanalysis. It is found that the temperature trend seasonality is greatest at the surface and decreases gradually through the troposphere. The seasonality resumes in the stratosphere.

Seasonal twentieth century hydroclimate trends are next characterized over the African continent. Examination of trends in SAT reveals that heat stress has increased in several regions, including Sudan and northern Africa, where greatest trends occur in the warm season. Precipitation trends are varied but notable declining trends are found in the countries along the Gulf of Guinea. Using a precipitation-based threshold, it is shown that the area of the Sahara Desert expanded significantly over the twentieth century, by 11-18% depending on the season, and by 10% when defined using annual-mean rainfall. Evaluation of climate models reveals difficulty in simulating seasonal century-scale hydroclimate trends over Africa.

These studies together offer support for the use of the seasonal perspective when analyzing changes of the past century, both for its relevance to society and for the potential to gain new process-level insights.

# ON THE ORIGIN OF HYDROCLIMATE CHANGE OVER CONTINENTS THROUGH SEASONALLY-STRATIFIED TRENDS

by

Natalie Paige Thomas

Dissertation submitted to the Faculty of the Graduate School of the
University of Maryland, College Park, in partial fulfillment
of the requirements for the degree of
Doctor of Philosophy
2019

Advisory Committee:
Dr. Sumant Nigam, Chair, Professor
Dr. Alfredo Ruiz-Barradas, Associate Research Professor
Dr. Ross Salawitch, Professor
Dr. Rachel Pinker, Professor
Dr. Eugenia Kalnay, Professor
Dr. Sujay Kaushal, Professor, Dean's Representative

# Acknowledgements

Firstly, I thank my advisor, Dr. Sumant Nigam for his guidance and mentorship. I have learned so much from working with him and I am very grateful for the encouragement, understanding and inspiration he has provided over the course of my graduate studies. Thank you to Dr. Alfredo Ruiz-Barradas for serving on my committee, and for his patience when offering much crucial help on data sets and analysis techniques. I am very appreciative of Dr. Ross Salawitch, Dr. Rachel Pinker and Dr. Eugenia Kalnay for taking the time to be on my committee, and for offering helpful suggestions during the prospectus. Thank you to Dr. Sujay Kaushal for serving as the Dean's Representative on my dissertation defense committee. I am grateful also to the rest of the faculty, staff and fellow students of AOSC for creating a welcoming community and a fun place to learn over the past few years.

I would like to thank Dr. Scott Weaver for support during my first year of graduate studies. I also gratefully acknowledge the support of the National Defense Science and Engineering Graduate Fellowship.

I had several excellent mentors during experiences as an undergraduate student, and I am thankful to have been introduced to research by them: Dr. Harvey Seim, Dr. Greg Gangi, Dr. Serena Chung and Dr. Manoj Nair.

Last but not least, I am endlessly grateful for the amazing support from my parents, Bonnye Hur and Bob Thomas, my brother Clayton, my grandparents, friends, and Keith.

# Table of Contents

# List of Tables

# List of Figures

# List of Abbreviations

| | |
|---|---|
| AMO | Atlantic Multidecadal Oscillation |
| AR5 | Fifth Assessment Report |
| CMIP | Coupled Model Intercomparison Project |
| CRU | Climate Research Unit |
| DJF | December, January and February (Northern Hemisphere winter) |
| DTR | Diurnal Temperature Range |
| ENSO | El Nino-Southern Oscillation |
| GFDL | Geophysical Fluid Dynamics Laboratory |
| GHCN | Global Historical Climatology Network |
| GISS | Goddard Institute for Space Studies |
| GPCC | Global Precipitation Climatology Centre |
| IGY | International Geophysical Year |
| IPCC | Intergovernmental Panel on Climate Change |
| ITCZ | Intertropical Convergence Zone |
| IUK | Iterative Universal Kriging |
| JJA | June, July and August (Northern Hemisphere summer) |
| MPI | Max Planck Institute |
| NASA | National Aeronautics and Space Administration |
| NCAR | National Center for Atmospheric Research |
| NCEP | National Centers for Environmental Prediction |
| NOAA | National Oceanic and Atmospheric Administration |

| | |
|---|---|
| PC | Principal Component |
| PDO | Pacific Decadal Oscillation |
| PDV-NP | Pacific decadal variability–North Pacific |
| RATPAC | Radiosonde Atmospheric Temperature Products for Assessing Climate |
| RCP | Representative Concentration Pathway |
| SAT | Surface Air Temperature |
| SST | Sea Surface Temperature |
| TRMM | Tropical Rainfall Measuring Mission |
| UKMO | U.K. Met Office |
| VIC | Variable Infiltration Capacity |
| WCRP | World Climate Research Programme |
| WGCM | Working Group on Climate Models |

# Chapter 1: Introduction

## 1.1 Climate Change

According to the fifth assessment report (AR5) from the Intergovernmental Panel on Climate Change (IPCC), "warming of the observed climate system is unequivocal, and since the 1950's, many of the observed changes are unprecedented over decades to millennia" (Alexander et al. 2014). Observed climate changes are varied and often characterized by complicated feedbacks; precise mechanisms of many observed changes remain to be understood.

### 1.1.1 Why is the climate changing?

Observed climate change is the result of both natural and anthropogenic drivers (Canty et al. 2013; Lean and Rind 2009; Meehl et al. 2004; Myhre et al. 2014; Thompson et al. 2009). Natural drivers include solar cycles, which have a period of approximately 11 years, aerosols from volcanic eruptions, and natural oscillations in the ocean-atmosphere system, which occur with a wide range of periodicities. A prominent example of such an oscillation is the El Nino-Southern Oscillation (ENSO), which affects climate conditions in remote regions of the world (Dai and Wigley 2000) and occurs with periodicity of 2-7 years. For studies of century-scale climate change, multidecadal variability in sea surface temperature (SST) in the Atlantic and Pacific basins is especially relevant. These oscillations are referred to as the Atlantic Multidecadal Oscillation (AMO) and Pacific Decadal Oscillation (PDO)

and can have significant impacts on large-scale temperatures (Steinman et al. 2015; Stolpe et al. 2017; Zhang et al. 2007).

Anthropogenic drivers of climate change include greenhouse gases, aerosols, and land use change (Stocker et al. 2014). The main greenhouse gases relevant for climate science are Carbon Dioxide ($CO_2$), Methane ($CH_4$) and Nitrous Oxide ($N_2O$) (Stocker et al. 2014). As these greenhouse gases increase in the atmosphere due to human activities, larger amounts of longwave radiation emitted from Earth's surface are trapped in the lower atmosphere. This excess energy affects the climate system in many ways but the focus in this dissertation will be on century-scale trends in observed hydroclimate variables: temperature and precipitation.

### 1.1.2 Temperature Changes

As a result of the increasing energy trapped by greenhouse gases, the lower layer of the atmosphere (the troposphere) warms while the second layer of the atmosphere (the stratosphere) cools (Santer et al. 2013). The stratosphere cools both because excess energy is trapped in the troposphere and cannot reach this layer, and also because of stratospheric ozone depletion (Mitchell 2016).

Surface air temperature (SAT) over continental regions has risen considerably over the twentieth century. Over 1880-2012, the global-mean surface temperature (from both land and oceans) warmed by approximately 0.85°C (Hartmann et al. 2014). In the work described in this thesis, the focus will be on changes in hydroclimate over continental regions rather than oceanic regions.

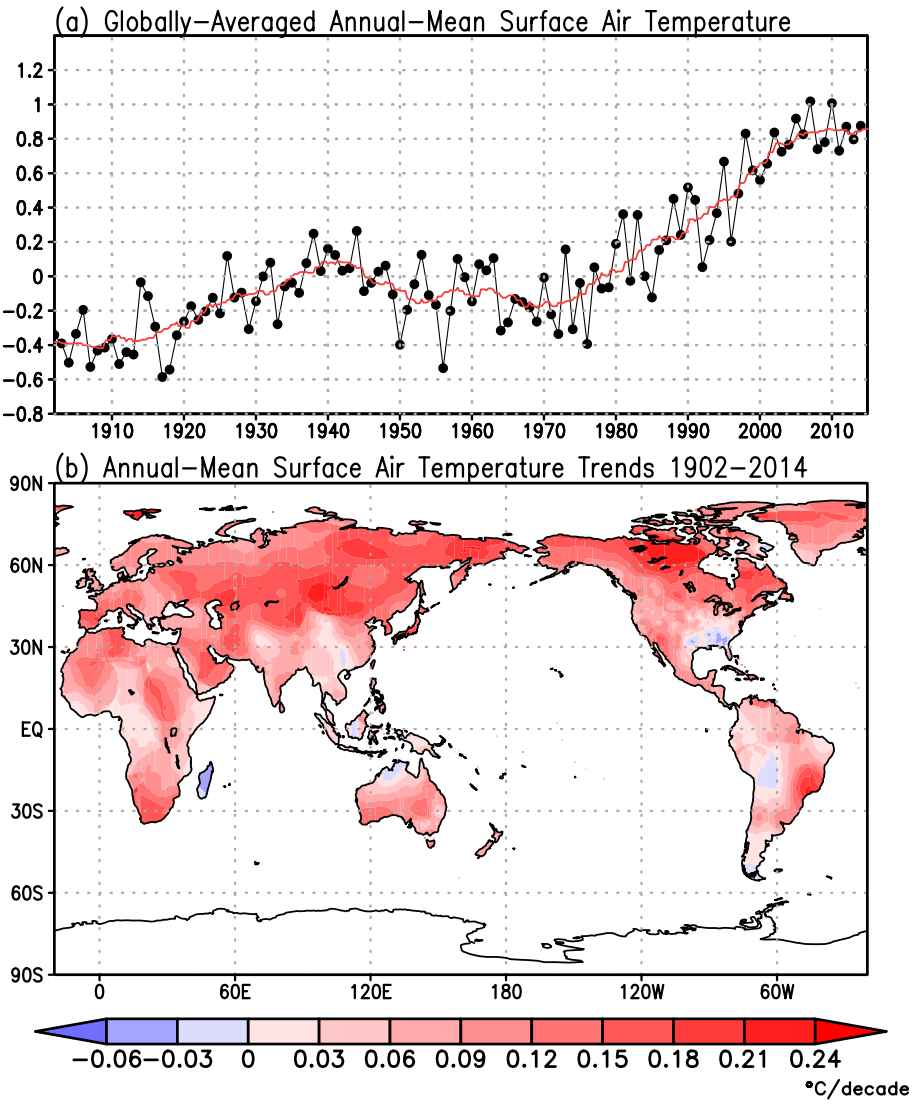


**Figure 1.1** (a) Global-mean, annual-average land surface air temperature (°C) from CRU TS 4.00 over 1902-2014. Temperatures are shown as anomalies relative to the 1961-1990 climatology. The black line and dots show the temperature anomaly every year and the red line shows the 10-year running mean. (b) Trends in global-mean land surface air temperature (°C decade$^{-1}$) over 1902-2014 from CRU TS 4.00.

The top panel of Figure 1.1 shows the global-mean, annually-averaged land SAT over 1902-2014 from the Climate Research Unit's CRU TS version 4.00 data set (Harris et al. 2014). This data set excludes Antarctica, although it has been noted that West Antarctica is among the most rapidly warming regions on earth over the second

half of the twentieth century (Bromwich et al. 2013). The twentieth century record of land temperature is characterized by multidecadal fluctuations superposed on an increasing trend, indicating a role for both secular change and multidecadal natural variability. In fact, modest cooling was seen during the 1940s-70s (Delworth and Knutson 2000) and during the so-called hiatus in warming at the beginning of the twenty-first century (Easterling and Wehner 2009). The recent period of accelerated warming began in the 1970s (Hartmann et al. 2014).

The annual-mean trends in temperature over continental regions for 1902-2014 from CRU TS 4.00 are shown in the bottom panel of Figure 1.1. This figure shows the lack of spatial uniformity in the warming. Generally, warming over continental regions is greater over higher latitudes in the Northern Hemisphere, a phenomenon known as arctic amplification (Cohen et al. 2014a; Serreze et al. 2009). Also noteworthy is the weak cooling in the southeastern US, or the US "warming hole" (Meehl et al. 2012; Pan et al. 2004). In general, the processes generating continental warming remain to be fully understood (Compo and Sardeshmukh 2009; Lu and Cai 2009; Stine and Huybers 2012; Stine et al. 2009; Wallace et al. 2012). While annual-mean temperature change is cited more frequently, in an effort to better understand driving processes, seasonal temperature changes will be the focus of the work described in this dissertation.

### 1.1.3 Precipitation Changes

Precipitation is a much more intermittent variable than temperature, and so large-scale changes in precipitation are more spatially complex. Theoretically, a

warmer atmosphere can hold more water vapor, based on the Clausius-Clapeyron equation (Trenberth 2011). Multiple data sets have shown globally averaged precipitation to have increased over the twentieth century, although large spread in these data sets leads to high uncertainty (Hartmann et al. 2014). Over the twentieth century, increases in precipitation were generally seen in middle and high latitudes of both hemispheres (Hartmann et al. 2014).

In general, climate change is associated with wet regions getting wetter and dry regions becoming drier (Trenberth 2011), although this has been disputed for continental regions (Greve et al. 2014). It is also expected that climate change will alter the character of precipitation, leading to less frequent but more intense precipitation, amplifying the risk of droughts and floods (Trenberth 2011). In terms of seasonal precipitation, Chou et al. (2013) showed that global warming results in an amplification of the seasonal cycle, with wet seasons getting wetter and dry seasons getting drier.

Characterizing and understanding seasonal precipitation trends has great societal value, particularly for agriculturally reliant societies. This will be the focus of the work in this thesis.

## 1.2 Climate Models

Given the climate changes that have been observed over past decades, it is critical to try to understand how the climate will change in the future. For this, the use of climate models is required.

Climate models are important tools for understanding past climate change and predicting future climate change. They provide a controlled environment for investigation of many different mechanisms in the system. Furthermore, the use of multiple ensemble members, or different runs of the same model where only initial conditions are changed, allows for the examination of internal variability and a way to quantify uncertainty (Murphy et al. 2004). Still, model-based estimations do exhibit considerable spread in past and future warming scenarios, in part due to inconsistent treatment of clouds, convection and aerosols (Flato et al. 2014). Another issue is the limited opportunity for validation of projections, given the long time scale inherent to climate studies.

### 1.2.1 IPCC CMIP5

The Coupled Model Intercomparison Project (CMIP) began in 1995 from the World Climate Research Programme (WCRP) Working Group on Coupled Models (WGCM) (Meehl et al. 2005). The CMIP was designed to allow for wide-ranging analysis of multi-model output in standardized format. The fifth phase of this project (CMIP5) was available in 2013. Results from CMIP5 were generally found to be very similar to results from the previous phase, CMIP3 (Knutti and Sedlacek 2013; Knutti et al. 2013). CMIP5 experiments include both century-scale and decadal-scale integrations from modeling centers around the world (Taylor et al. 2012). Historical simulations included in CMIP5 are forced by observed changes over the twentieth century, namely historical gas emissions, aerosol loadings and solar activity. Future projections are made using forcing from four different representative concentration

pathways (RCPs), which estimate radiative forcing in the year 2100 (Taylor et al. 2012).

In the studies covered in this dissertation, historical simulations from five participant models in the IPCC AR5 are analyzed. The model details are in Table 1.1. The model choice reflects representation from the major modeling centers of both the United States and Europe, with the limited selection allowing closer examination of individual model performance.

**Table 1.1** Details of the analyzed CMIP5 historical climate simulations. Trends in the 1902-2004 period are investigated.

| **Model Name** | **Modeling Center** | **Number of realizations (ensemble size)** | **Grid resolution (longitude × latitude)** | **Available time period** | **Reference** |
|---|---|---|---|---|---|
| CCSM4 | NCAR | 6 | 1.25° × 0.942° | 1850-2005 | (Gent et al. 2011) |
| GFDL-CM3 | NOAA-GFDL | 5 | 2.5° × 2.0° | 1860-2004 | (Donner et al. 2011) |
| HadCM3 | UKMO | 9 | 3.75° × 2.5° | 1860-2005 | (Gordon et al. 2000) |
| HadGEM2-ES | UKMO | 4 | 1.875° × 1.25° | 1860-2005 | (Collins et al. 2011) |
| MPI-ESM-LR | MPI | 3 | 1.875° × 1.865° | 1850-2005 | (Giorgetta et al. 2013) |

### 1.2.2 Validation Efforts

In order to gain confidence in future projections of climate, careful evaluation of models' historical simulations is critical. In terms of multi-model ensemble mean projections, the optimal way to weight model members remains an open question. A related issue is the shared components that exist between models, calling their independence into question (Boe 2018; Knutti 2010). Previous studies have used a variety of metrics to evaluate climate models, but there does not exist a standard set of performance evaluators (Baker and Taylor 2016).

The CMIP5 models have been evaluated using many different metrics. The evaluation benchmarks are naturally dependent on the problem that is being addressed. An entire chapter of IPCC AR5 is devoted to evaluation of climate models and it is concluded that the CMIP5 ensemble is generally successful at simulating annual-mean surface temperature, the seasonal cycle of temperature, and the historical global-mean surface air temperature increase (Flato et al. 2014). The simulation of the mean state of precipitation has more biases with respect to observations. Other recent metrics that have been used to evaluate climate models include trends in diurnal temperature range (Lewis and Karoly 2013), regional, seasonal precipitation (Baker and Huang 2014) and spatial variability in the twentieth century trend in annual-mean temperature (Kumar et al. 2013) A focus of this dissertation will be evaluating climate projection models using the seasonality of century-scale hydroclimate trends.

## 1.3 Limitations of observationally-based studies

The work described in this thesis is mostly observationally based. This type of study is not without limitations. Particularly for studies over the full century, data coverage can be sparse in some regions. Various gridded products of SAT use common input data but different interpolation methods (Jones 2016); it is necessary to understand the different assumptions involved. For example, the HadCRUT4 temperature data set (Jones et al. 2012) does not interpolate to estimate temperatures in unsampled regions; this has been found to introduce biases into temperature trends (Cowtan and Way 2014).

The CRU-TS 4.00 monthly analysis from the Climate Research Unit of the University of East Anglia (Harris et al. 2014) will be utilized frequently in this dissertation to analyze SAT trends. For this data set, if a certain grid cell has no station data for a particular month, it is populated with the climatological mean value computed over 1961-1990. Figure 1.2 shows the number of unique values of winter SAT for each grid point from CRU TS 4.00 for 1902-2014, i.e. number of winters in the 113-year period where the SAT is not filled in with the climatology. In general, data coverage is better over the northern hemisphere than over the southern hemisphere. Data coverage is particularly lacking over parts of Africa, the land surrounding the Northwestern Passages and parts of South America. Note that data coverage will be assessed more thoroughly for other SAT data sets for the African continent in section 4.2.1.

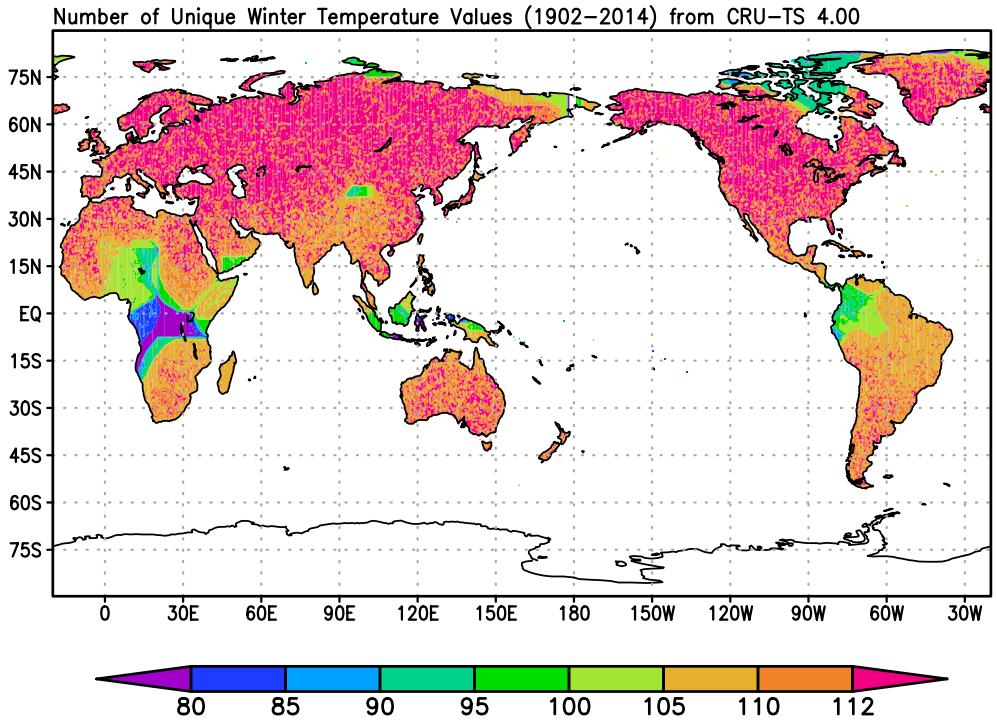


**Figure 1.2** Number of winter SAT values for the 113-year period from1902-2014 containing station data in the CRU TS 4.00 data. This indicates the number of time steps where values are not filled by the 1961-1990 climatology, which is done if a grid cell has no station data (Harris et al. 2014).

Despite sparser coverage in earlier decades, global century-scale temperature trends have been found to be reliable starting in the late 19$^{th}$ century (Karl et al. 1994). For regional or grid-box scale temperature trends, the issue of data coverage becomes much more important (Jones 2016).

For precipitation data, spatial coverage is also a concern. In fact, given the large spatial and temporal intermittency of precipitation, a greater number of stations are required to create a reliable analysis than for temperature (Schneider et al. 2014). Studies described here will largely rely on the precipitation analysis of the Global Precipitation Climatology Centre (GPCC). Data coverage maximizes in June 1986 for this data set, when 47400 stations are included in the global analysis (Becker et al. 2013).

Furthermore, while changes in hydroclimate variables are inextricably linked to clouds, lack of complete observations of clouds over the full twentieth century precludes an observationally based assessment of this connection.

Another limitation of observationally based studies is that the observational record presents just one realization of nature. This makes it challenging to separate forced versus internal climate changes and attribute mechanisms. Furthermore, it is not possible to experiment with how changing one parameter can affect the rest of the system, as can be done with climate system models. The issue of internal variability has been addressed by McKinnon et al. (2017) with the creation of an observational large ensemble used to determine the range of possible past trends that could have occurred if internal variability had been different.

## 1.4 Motivation of Current Work

The studies described in this dissertation use observational analysis to characterize and understand twentieth century climate changes. As mentioned, the annual-mean record of climate consists of just one realization, which limits the ability to gain mechanistic insights from observations alone. However, examining changes in climate *seasonally* expands the phase space for observational investigation of mechanisms.

Seasonal and hemispheric variations have been exploited in previous work to investigate various phenomena. Examples include ocean-atmosphere interaction in the tropics (Mitchell and Wallace 1992; Nigam and Chao 1996; Philander and Chao 1991), the Hadley circulation (Dima and Wallace 2003; Lindzen and Hou 1988; Oort

and Yienger 1996) and the summertime strengthening of the Northern Hemisphere sea level pressure anticyclones (Hoskins 1996; Nigam and Chan 2009). However, the seasonal perspective has yet to be used to provide insights into century-scale hydroclimate change.

The following questions outline the overarching motivation for the studies described.

1. *Can examining century-scale climate changes through a seasonal lens provide a new perspective to understand past changes and predict future ones? What can the seasonal variation of long-term trends reveal about mechanisms of climate change over continental regions?*

Annual-mean changes in temperature and precipitation are the most frequently cited quantities with respect to hydroclimate changes. By shifting away from the annual-mean perspective, the seasonal stratification of hydroclimate trends has the potential to offer new insights and advance process-level understanding. The work described here will compare annual-mean climate changes with seasonally stratified ones to assess whether this affords new information about physical processes involved in the changes.

Furthermore, changes in a seasonal perspective are particularly societally relevant, especially in terms of agriculture. For example, a recent study noted the importance of analyzing seasonal rainfall patterns in the tropics, given the relevant local ecological and social considerations (Feng et al. 2013). In Chapter 4, hydroclimate changes over Africa are studied. Given the prominence of the

agricultural sector in economies of many African nations (Fields 2005), it was hypothesized that a seasonal perspective would be more informative.

Differences in circulation and hydroclimate in each season are superposed on a consistent radiative forcing from greenhouse gases. Thus, seasonal processes are a potentially important way to gain process-level insights into the generation of continental warming. For example, determining whether the spatial variation in long-term annual-mean trends (see Figure 1.1) is due to dominating contributions from a particular season would be insightful.

The studies comprising this thesis will examine different dynamical and thermodynamical processes relevant in different seasons in order to explain seasonal variations in century-scale trends.

2. *How well do current leading climate models capture the observed seasonality in twentieth century seasonal hydroclimate trends?*

This thesis aims to address how models currently reproduce seasonal hydroclimate trends over the twentieth century. Weather models have improved steadily in part due to the routine feedback afforded from evaluating forecasts (Bauer et al. 2015). The same opportunity does not exist for climate models, as long-term projections cannot be verified frequently enough to lead to improvements. Decadal climate predictions provide some evaluative feedback, but these are not without issues and can be computationally burdensome (Meehl et al. 2009; Meehl et al. 2014). Exploiting seasonally stratified hydroclimate trends offers a new metric for evaluation

without need for additional integrations. The work described here attempts to characterize the status of current models in reproducing this observed feature.

While there are many metrics to evaluate climate models (see section 1.2.2), it is argued here that the seasonality of century-scale trends has the potential to be especially informative, given that it allows for multiple validations of the same model with respect to a single variable, but without the need for additional integrations.

## 1.5 Dissertation Structure

This dissertation is organized in the following way. Chapter 2 details the seasonality in surface air temperature over Northern Hemisphere continents, and offers potential explanatory mechanisms for it. A new hypothesis for the observed seasonality is presented, and CMIP5 models are evaluated using SAT trend seasonality as a new metric. Most of this chapter is published as Nigam et al. (2017) in *Journal of Climate*. Chapter 3 is based on Thomas et al. (2018), which is now under review in *Climate Dynamics*. This work is a follow-on study to Nigam et al. (2017) and assesses the seasonality in *upper-air* temperature trends over the regions of greatest surface temperature trend seasonality over North America using both radiosonde data sets and global reanalysis. This study aims to further probe the relative roles of the dynamic and thermodynamic mechanisms outlined in Chapter 2 for SAT trend seasonality. Chapter 4 characterizes seasonality in twentieth century hydroclimate trends over Africa, with a particular focus on the Sahara Desert expansion. CMIP5 models are again evaluated in terms of their ability to simulate seasonal century-scale hydroclimate trends in this region. This work is published as Thomas and Nigam

(2018) in *Journal of Climate*. Chapter 5 summarizes the main results, draws conclusions, and outlines future related research needs.

# Chapter 2: Seasonality in surface air temperature (SAT) trends over Northern Hemisphere continents[1]

## 2.1 Background

Surface air temperature over the Northern Hemisphere continents has risen sharply in recent decades. The seasonal variations in secular warming have been noted in several observational analyses, all of which indicate the winter and spring SAT trends to be stronger than the summer and fall ones. The analyzed regions include the global domain (Balling et al. 1998; Kusunoki et al. 2009), the Northern Hemisphere (Robeson et al. 2014; Stine and Huybers 2012; Stine et al. 2009; Wallace et al. 1995; Wallace et al. 2012), the continental United States (Redmond and Abatzoglou 2014; Wang et al. 2009), the western United States (Abatzoglou and Redmond 2007), the Pacific Northwest (Abatzoglou et al. 2014; Mote 2003), and Alaska, Canada, and Mexico (Redmond and Abatzoglou 2014). The recent period (1979–2005) SAT trends, stratified by season in IPCC AR4 (Trenberth and Jones 2007), also show two clear maxima: winter warming over North America and spring warming over north-central Asia (see their Fig 3.10).

The seasonality in secular warming has also been studied using climate simulations: Lu and Cai's (2009) analysis of the IPCC AR4 simulations showed the clear-sky downward longwave radiation at the surface to be important for the larger winter warming signal in the polar region; Dwyer et al. (2012) also examined AR4

[1] Most of this chapter is published as Nigam, Thomas, Ruiz-Barradas and Weaver (2017), although there has been some slight re-organization, update of data sets and addition of supporting details in this chapter.

models and concluded that stronger winter warming in the Arctic was attributable to increasing sea ice loss. Other studies used atmospheric general circulation models (AGCM) forced by historical sea surface temperatures (SSTs) and greenhouse gas concentrations to study seasonal temperature changes. Kusunoki et al. (2009) found the model they examined to be unable to simulate observed seasonality in SAT trends. Wang et al. (2009) attributed observed seasonal trends in SAT over the US to multidecadal SST variability in the Pacific and Atlantic basins.

Finally, it is worth noting that while the seasonally distinct climate base states can serve as a prism for viewing the processes generating secular warming, each of these states is associated with different levels of internal variability (or dynamical noise), leading to different signal detection thresholds. Stine et al. (2009) argue that although warming is stronger in winter, the winter SAT trends are less significant on account of the larger variance of monthly temperature in boreal winter.

The seasonal perspective has been useful in advancing understanding of several climate variability phenomena (see section 1.4) but it has yet to be used to provide insights on the origin of regional and seasonal variations of secular warming, especially the centennial trends over the northern continents. The present analysis is motivated by these possibilities.

## 2.2 Data and Methods

### 2.2.1 Observed SAT

Four different analyses of near-surface air temperature (SAT) are used to characterize the seasonality of SAT trends. The CRU-TS 4.00 monthly analysis from the Climate Research Unit of the University of East Anglia (Harris et al. 2014) is

available on a 0.5° continental grid for the January 1902-December 2014 period from http://www.cru.uea.ac.uk/cru/data/hrg/cru_ts_4.00/.

The CRUTEM4 analysis from the UK Met Office's Hadley Centre provides monthly near-surface air temperature anomalies relative to the 1961-90 baseline (Jones et al. 2012). It is available on the coarser 5.0° land-ocean grid for the January 1850-September 2015 period from http://www.cru.uea.ac.uk/cru/data/temperature/#datdow. There is no spatial interpolation applied to this data set to estimate values of grid points with no station data, so there is a fair amount of missing data through the middle part of the twentieth century.

Berkeley Earth's monthly analysis of surface temperature (Rohde et al. 2013) is available on a 1.0° land-ocean grid from 1850-2015 and can be downloaded at http://berkeleyearth.org/data/. Data are provided as anomalies relative to the 1951-80 climatology.

Finally, the NASA Goddard Institute for Space Studies (GISS) analysis of near-surface temperature (Hansen et al. 2010) is available on a 2.0° land-ocean grid for the January 1880-September 2015 period from http://www.esrl.noaa.gov/psd/data/gridded/data.gistemp.html. Monthly anomalies relative to the 1951-80 baseline are provided.

#### 2.2.2 Observed continental precipitation

The Global Precipitation Climatology Centre (GPCC) provides a monthly analysis of precipitation from quality-controlled station gauge data (Becker et al. 2013). GPCC's full data reanalysis version 7 data, available on a 0.5° continental

grid for the January 1901-December 2013 period, are used here (see http://www.esrl.noaa.gov/psd/data/gridded/data.gpcc.html#detail). From the several available analyses of continental precipitation (including CRU-TS), the GPCC analysis was chosen because of the larger number of stations used in the development of this gridded product, especially relative to CRU-TS and the Global Historical Climatology Network (GHCN). The monthly precipitation database informing the GPCC analysis is, perhaps, the largest among the competing analyses (Schneider et al. 2014; their Figure 2), prompting its use in constraining NASA's Tropical Rainfall Measuring Mission (TRMM) precipitation.

### 2.2.3 Evapotranspiration

Evaporation measurements are sparse and generally confined to subgrid-scale basins, such as the U.S. Department of Agriculture watersheds, the Oklahoma Mesonet, and the Illinois Water Survey field sites. Sparse pan measurements of evaporation do exist but inferring terrestrial evapotranspiration from them is challenging (Brutsaert 2006). For these reasons, evapotranspiration is often diagnosed, residually, from the atmospheric water balance (Ruiz-Barradas and Nigam 2005).

Evapotranspiration from the University of Delaware's Terrestrial Water Budget Data Archive (version 4.01) is analyzed (Willmott and Matsuura 2015). Monthly data on a 0.5° continental grid from http://climate.geog.udel.edu/~climate/html_pages/Global2014/README.GlobalWbTs2014.html are available for the January 1900-December 2014 period. Evapotranspiration was diagnosed at the University of Delaware from the monthly

water budget, which was estimated from the monthly averaged temperature and precipitation fields following modification of the Thornthwaite water budget procedure (Willmott et al. 1985).

Given the challenging nature of the diagnosis of evapotranspiration, a recent independent estimate from Princeton University's global land surface hydroclimate simulations with the Variable Infiltration Capacity (VIC) land surface model (Sheffield and Wood 2007; Sheffield et al. 2006) is intercompared with the University of Delaware's diagnosis. Monthly data on a 1.0° continental grid from an offline simulation are available at http://hydrology.princeton.edu/data.lsm.php. Evapotranspiration was calculated using a Penman-Monteith formulation with adjustments to canopy conductance to account for environmental factors. This model- based evapotranspiration was not part of the main analysis as it is available only for the second half of the twentieth century (1948-2000). However, for comparison, Figure 2.1 shows the summer-minus-winter evapotranspiration trends from both the University of Delaware dataset and the VIC model for the common period.

There are regional differences between these two products in their estimation of evapotranspiration trends. These inconsistencies are due to the different methods used to estimate evapotranspiration. The modified Thornthwaite water budget used in the University of Delaware data set estimates evapotranspiration from observed temperature and precipitation. The Penman-Monteith formulation, used in the VIC estimates, calculates evapotranspiration as a function of temperature, wind speed, relative humidity, and solar radiation. Still, the regional differences in

evapotranspiration trend shown in Figure 2.1 are embedded in a broadly similar pattern that includes larger values over the Northwest Territories in Canada and over the central and southern Great Plains.

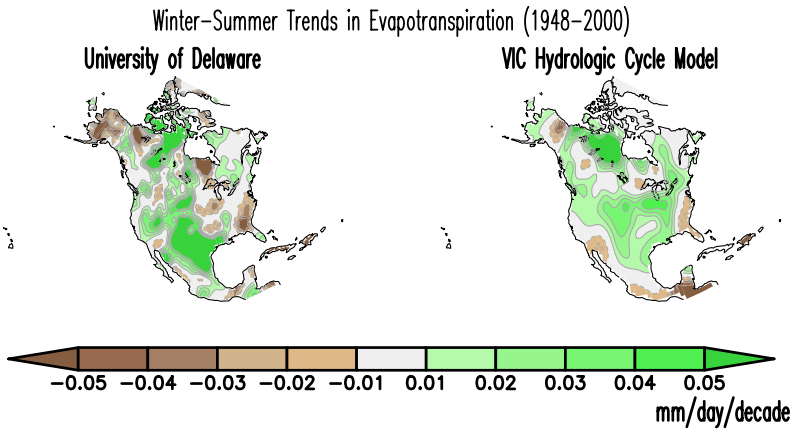


**Figure 2.1** Intercomparison of the winter-minus-summer evapotranspiration trends (mm day$^{-1}$ decade$^{-1}$) from two independent evapotranspiration diagnoses, in their common period (1948-2000). Data from the University of Delaware's Terrestrial Water Budget Archive are used in the left panel, and from Princeton University's Global Land Surface Hydrology Simulations with the VIC land surface model in the right panel. The contour interval for both is 0.01 mm day$^{-1}$ decade$^{-1}$.

### 2.2.4 Historical climate simulations

Historical simulations from five participant models in the IPCC's AR5 are analyzed in this study; the model details are in Table 1.1. Trends are ensemble-averaged for historical simulations. The averaging was undertaken to attempt to preclude any model-generated ultra-low-frequency (centennial and longer time scale) variability from aliasing the twentieth-century trend.

### 2.2.5 Analysis method

The Grid Analysis and Display System (GrADS) toolkit is used for most analyses. The linear trend is computed using the least squares fitting. Seasons are

defined in a customary manner [e.g., boreal winter is defined as the average of December–February (DJF)]. Seasonal averages are constructed prior to the computation of linear trend. Although not commutative, reversing the order of operations has a negligible impact; for example, it leads to a trend difference of $10^{-7}$ °C decade$^{-1}$ in the century-long seasonal SAT trend. In the analysis of historical simulations, the linear trend in each ensemble member is averaged to yield the ensemble-mean trend. Again, reversing this process (i.e., computing linear trend in the ensemble-mean) led to very small differences. A 9-point smoother (the smth9 function in GrADS) is applied to most figures in order to minimize noise and highlight the large-scale spatial features of the seasonal trends. Geographical averages are computed using area-weighted means. The seasonal SAT trend plotted for each region is the trend in the regionally averaged SAT.

The dynamical contribution to the SAT trend is assessed by inferring the geostrophic wind trend ($V_{g\_trend}$ in units of m s$^{-1}$ decade$^{-1}$) from the gradients in sea level pressure (SLP). Advection of the climatological surface temperature ($T_{clim}$) by $V_{g\_trend}$ yields the thermal advection trend ($V_{g\_trend} \cdot \nabla T_{clim}$) in units of °C s$^{-1}$ decade$^{-1}$. The resulting SAT trend ($T_{t\_dyn}$) is estimated by balancing this thermal advection trend with Newtonian damping of temperature, $V_{g\_trend} \cdot \nabla T_{clim} \approx -\gamma T_{t\_dyn}$, where the right-hand side represents thermal damping of lower tropospheric temperature by synoptic transients; $\gamma$ is taken as (3 days)$^{-1}$ following (Lau 1979; Table 1 therein). The above two terms represent the dominant balance in the thermodynamic equation in the middle to high latitudes; ignoring diabatic heating (e.g., radiative forcing in context of secular warming) here is not problematic given

the focus on diagnosis of just the dynamical contribution to warming. A similar strategy was used in analysis of the extreme 2013/14 North American winter where thermal advection by the North Pacific Oscillation–west Pacific teleconnection was implicated in the extreme cold (Baxter and Nigam 2015).

The statistical significance of the fitted trends is estimated from the ratio of the slope and its standard error. Significance at the 95% level is evaluated from the Student's t distribution using an effective sample size computed from the lag-1 autocorrelation of the detrended time series, as in the adjusted standard error and adjusted degrees of freedom method (AdjSE + AdjDF) (Santer et al. 2000).

## 2.3 Seasonal trends in observed SAT

Surface air temperature exhibits a warming trend over the northern continents. The warming is pronounced in boreal winter and spring (Figure 2.2) when the statistically significant century-long trend exceeds 0.2 °C decade$^{-1}$ over continental regions extending from the Gobi Desert to central Siberian uplands in Asia, and from the northern Great Plains to the western-central Canadian provinces in North America. Interestingly, SAT trends are considerably weaker in boreal summer and fall, with the Asian continent devoid of any significant warming in summer and the North American continent in fall, leading to slight attenuation of seasonal SAT variability. A notable exception is the Middle East and Saharan Africa where the warming SAT trend is most impressive in boreal summer, amplifying the seasonal cycle and heat-related stresses (see Chapter 4). Other noteworthy features in Figure 2.2 include the following:

- the coherent subcontinental scale structure, with the winter–spring SAT trends

neither longitudinally uniform nor latitudinally monotonic,

- the continental interior (and not Arctic rim) location of the maximum winter–spring SAT trends, and
- the weak trends over south central-eastern United States in all seasons.

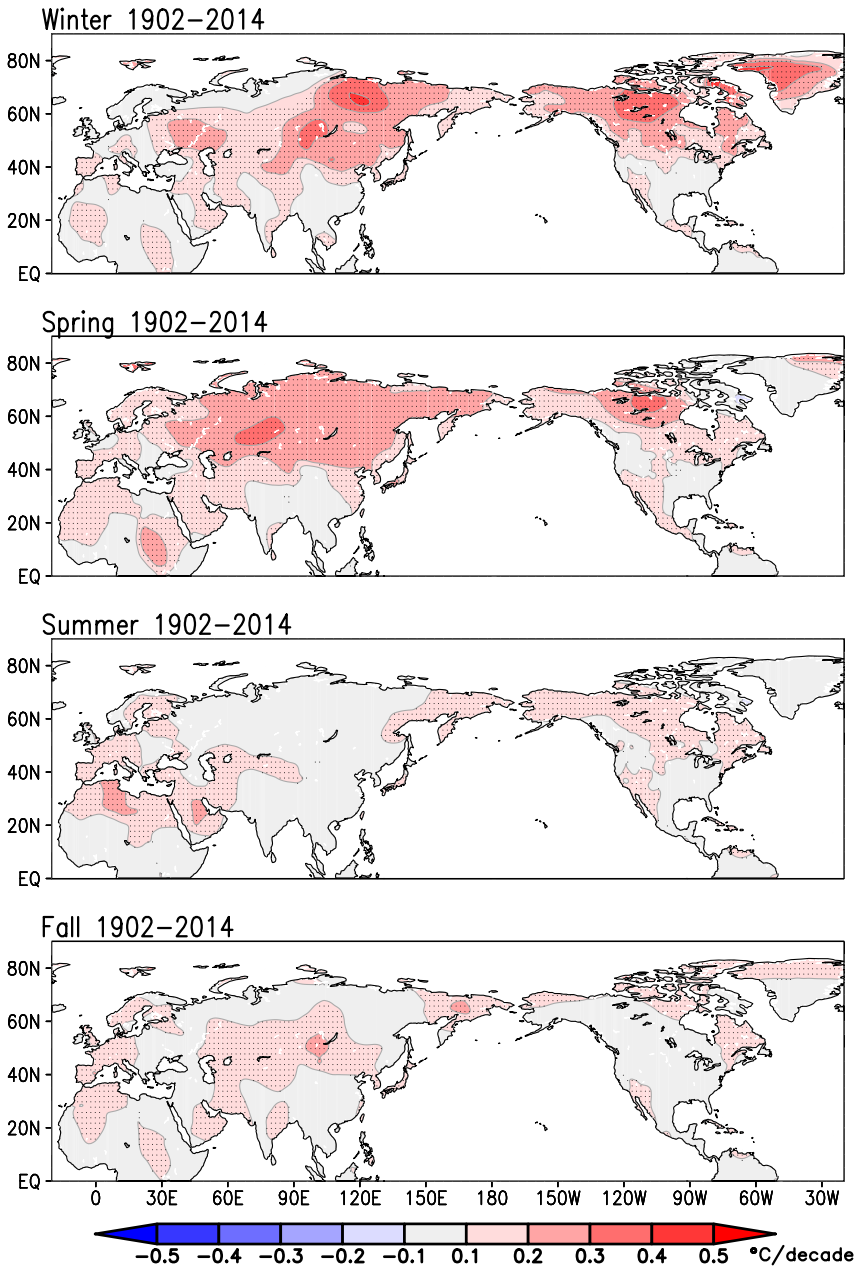


**Figure 2.2** The linear trend in seasonal SAT over the Northern Hemisphere continents during 1902-2014 from the 0.5° resolution CRU TS4.00 data set. Contour interval and shading threshold is 0.1°C decade$^{-1}$. The fields are shown after nine applications of the nine-point smoother (*smth9*) in GrADS. Trends significant at the 95% level are stippled.

The robustness of century-long SAT trends in the CRU-TS4.00 analysis is assessed by examining the corresponding trends in three independent analyses of

SAT—CRUTEM4, Berkeley Earth, and NASA-GISS— in Figure 2.3. Comparison of the winter trends (left column) indicates broad agreement over North America, Eastern Europe, and Asia. The average trend from the four SAT analyses—the observation ensemble mean (Figure 2.3, bottom panels)—confirms the striking seasonal variation of SAT trends over vast stretches of Asia and North America that were noted earlier. The bottom panel of Figure 2.3 shows the standard deviation in seasonal trends from the four analyses. Variability between analyses is greatest over central Asia in both winter and summer, and to a lesser extent also over Northwest North America.

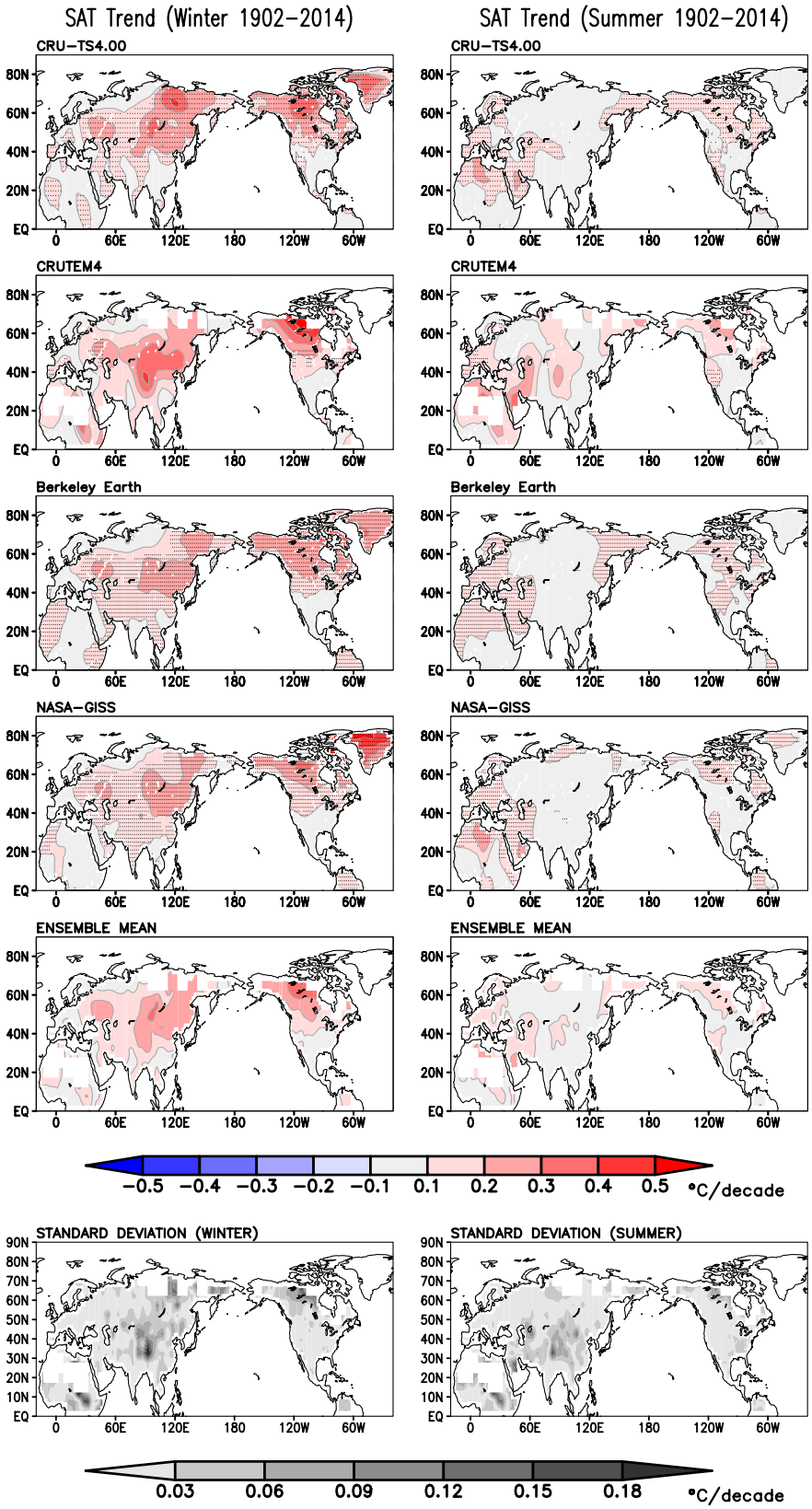


**Figure 2.3** The linear SAT trend in (left) winter and (right) summer during 1902-2014 in four observational analyses, and the average trend and standard deviation.

From top to bottom, the four analyses are: 0.5° resolution CRU TS 4.00, 5.0° resolution CRUTEM4, 1.0° resolution Berkeley Earth, 2.0° resolution NASA-GISS. The mean and standard deviation of the four linear trends are shown in the bottom two rows. Contour interval and shading threshold is 0.1°C decade$^{-1}$. The fields are displayed after 9,1,1 and 1 applications, respectively of 'smth9'. Trends significant at the 95% level are stippled.

## 2.4 Seasonal SAT trends in historical climate simulations

Historical simulations serve an important evaluative role for models whose projections of climate change constitute the backbone of the IPCC AR5 assessment (Flato et al. 2014). The canonical evaluation from an intercomparison of the annual-mean warming trends is expanded upon here by analyzing the simulation of seasonal warming trends. The ensemble mean of the century-long SAT trends in historical simulations generated by the five selected IPCC AR5 participant models is shown in Figure 2.4, for both winter and summer. The winter SAT trend in the five historical simulations has varied, and often, unrealistic strength or structure (Figure 2.4, left column): the GFDL-CM3 and UKMO HadCM3 and HadGEM2 simulations exhibit much weaker winter SAT trends (less than 1.0 °C century$^{-1}$, the shading threshold) almost everywhere. On the other hand, the NCAR CCSM4 and MPI-ESM-LR simulations contain fairly realistic expressions of winter warming over Asia and North America. These simulations also exhibit weaker trends in summer, but not as weak as those observed.

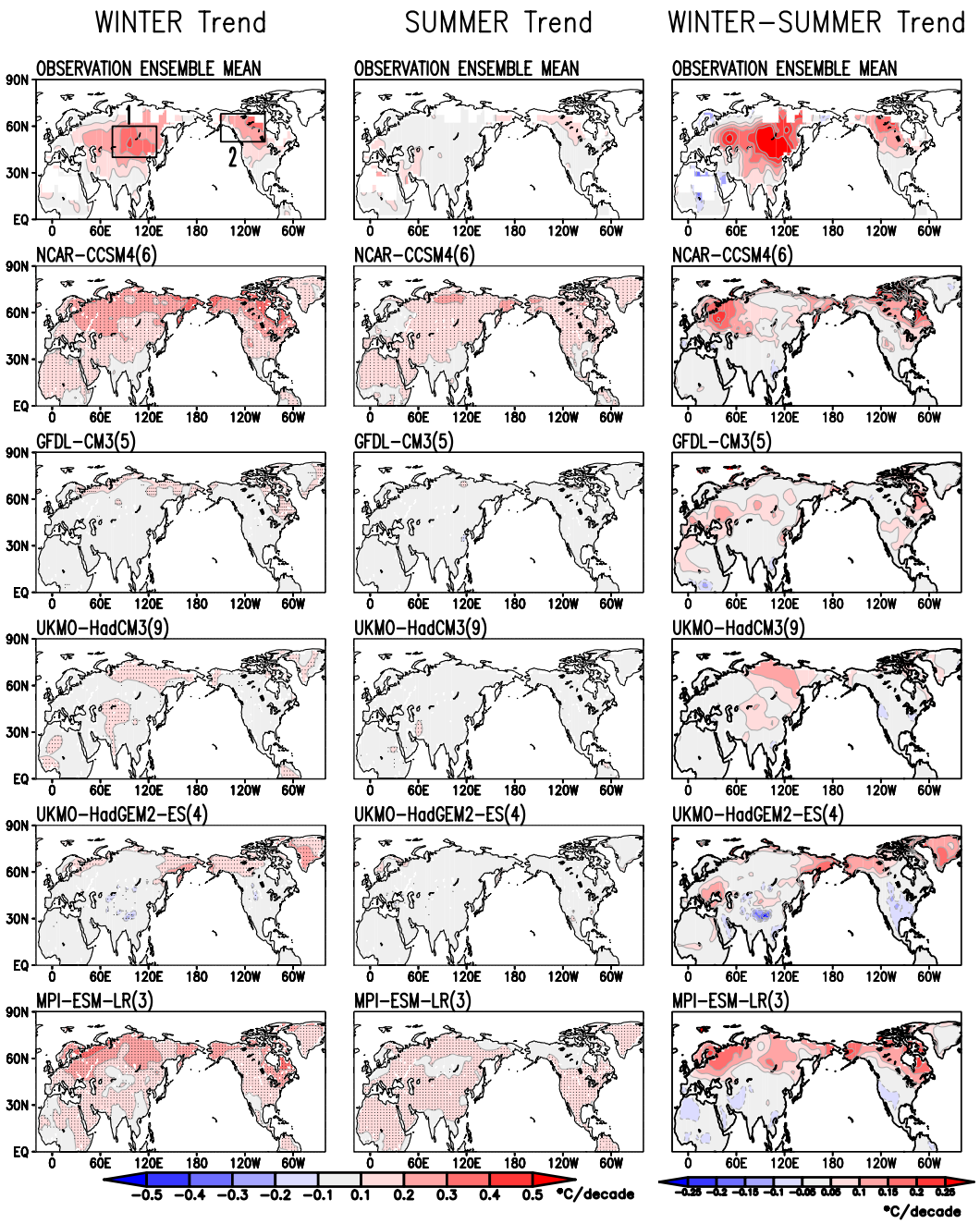


**Figure 2.4** The linear SAT trend in (left) winter and (center) summer (JJA) in five IPCC-AR5 model simulations of twentieth century climate (1902–2004). The seasonal amplitudes in SAT trends, i.e., winter-minus-summer trends, are shown in the right column with half the interval used in the left ones. The number of ensemble members in each simulation is noted in parentheses, and the average trend across all ensemble members is shown. The average linear trend in the same period in four analyses of SAT observations (CRU-TS4.00, CRUTEM4, Berkeley Earth, and NASA-GISS)—the observation ensemble and simulation target—is shown in the top row. As the model fields are on a relatively coarser grid (see Table 1.1), smth9 is applied only once on them. Shading and contouring are as in Figure 2.2 for the left

and center columns. Trends significant at the 95% level are stippled. The two regions exhibiting large winter trends in observations are marked in the top-left panel for later analysis.

### 2.4.1 Seasonal amplitude of SAT trends

The winter–summer difference, or the ‘‘seasonal amplitude’’ of SAT trends, is displayed in the right column of Figure 2.4 using a lower contour interval to facilitate assessment of all five historical simulations. The observed amplitude (the target) is in the top panel, as before. The much weaker seasonality of SAT trends in the GFDL CM3 and HadCM3 (and even HadGEM2-ES) historical simulations is now readily apparent, especially in the northern Great Plains and northwestern Canada. The amplitude of SAT trends is more realistic in the NCAR CCSM4 and MPI-ESM-LR simulations but the spatial structure is at some variance with the observed one. For example, these simulations exhibit large amplitude over North America in the region around Hudson Bay but the observed amplitude (top panel) is large southwestward of this region (i.e., just eastward of the Canadian Rockies). Over Asia, large amplitudes are focused on European Russia and Scandinavia in the simulations and over eastern Russia, Siberia, and Mongolia in observations.

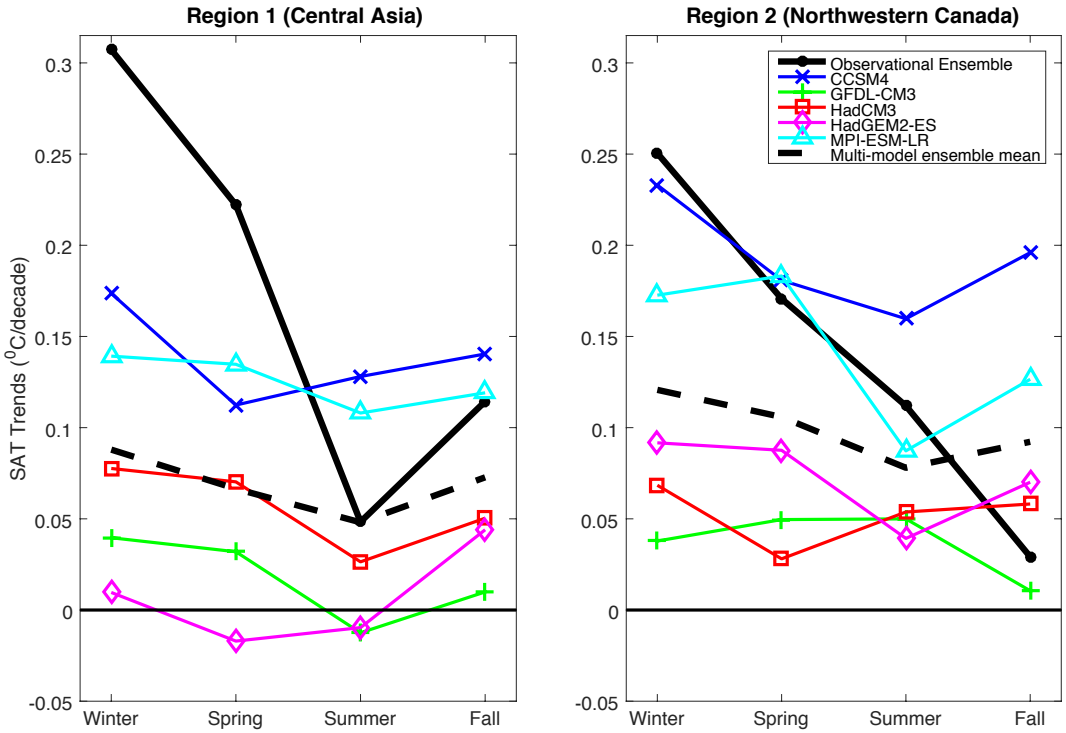


**Figure 2.5** The area-averaged seasonal SAT trends in region 1 (Mongolia and south-central Russia) and region 2 (Alaska and western-central Canada) for the 1902–2004 period; both regions are marked in Figure 2.4 (top-left panel). The linear trend averaged across four observational analyses—the simulation target—is plotted using the thick black solid line, while the corresponding trend, averaged across all historical simulations (27 in number from 5 models), and referred to as the multimodel ensemble-mean trend, is shown by the thick black dashed line. The trends from individual models are shown using colored lines; see the legend.

### 2.4.2 Seasonal variation of regional SAT trends

The seasonal variation of SAT trends in two geographical regions exhibiting large winter warming in twentieth-century observations (regions 1 and 2 marked in the top-left panel of Figure 2.4) is shown in Figure 2.5. Over Alaska and western-central Canada (region 2), the observed SAT trend (thick solid black line) is largest in winter (~2.5 °Ccentury$^{-1}$) and weakest in fall, when it is less than 0.5°C century$^{-1}$, or weaker by a factor of 4 compared to the winter value—a remarkable seasonal variation. In contrast, the multimodel ensemble-mean SAT trend (thick dashed black

line), obtained by averaging the trends in all historical simulations, shows much weaker seasonal variability, by at least a factor of 2. Of the constituent models, NCAR CCSM4 and the MPI-ESM-LR exhibit fairly realistic seasonal variations but for the increasing SAT trend in fall. The other three models generate weak SAT trends in all seasons, with the season of maximum (and minimum) trend at variance with observations. Over Mongolia and south-central Russia (region 1), the observed SAT trend is strongest in winter and weakest in summer; the winter-to-summer decline is by a factor of 4 or more, as before. In contrast, the multimodel ensemble-mean SAT trend is almost seasonally invariant.

The examined IPCC AR5 models are not viable investigative tools for analyzing the origin of the impressive seasonality in observed SAT trends in view of deficiencies in their representation of this feature; Stine et al. (2009) reached similar conclusions in the context of the IPCC AR4 models.

### 2.4.3 Robustness of century-long SAT trends

The robustness of winter SAT trends in the models is evaluated by dividing the ensemble-averaged trend (the signal) by the intraensemble standard deviation of the century-long trends (the noise); the signal-to-noise ratio is shown in Figure 2.6. The heavier shading (smaller ratios) identifies the subregions where the indicated secular winter warming is, in fact, not robust on account of the large regional ‘‘dynamical’’ noise in historical simulations. As the ensemble size varies considerably (from 3 to 9), intermodel comparisons of the shaded regions are not appropriate. The GFDL and NCAR models, however, have similar ensemble size (5 and 6, respectively) but pronouncedly different ratios: Over northern Asia, dynamical

noise overwhelms the secular warming signal in the GFDL-CM3 historical simulations but not in the NCAR-CCSM4 ones. The signal-to-noise ratio is larger than 1.333 almost everywhere in the NCAR simulations, as it is in the MPI-ESM-LR ones. The analysis suggests some caution in the use of unweighted multimodel ensemble-average for characterization and attribution of secular warming.

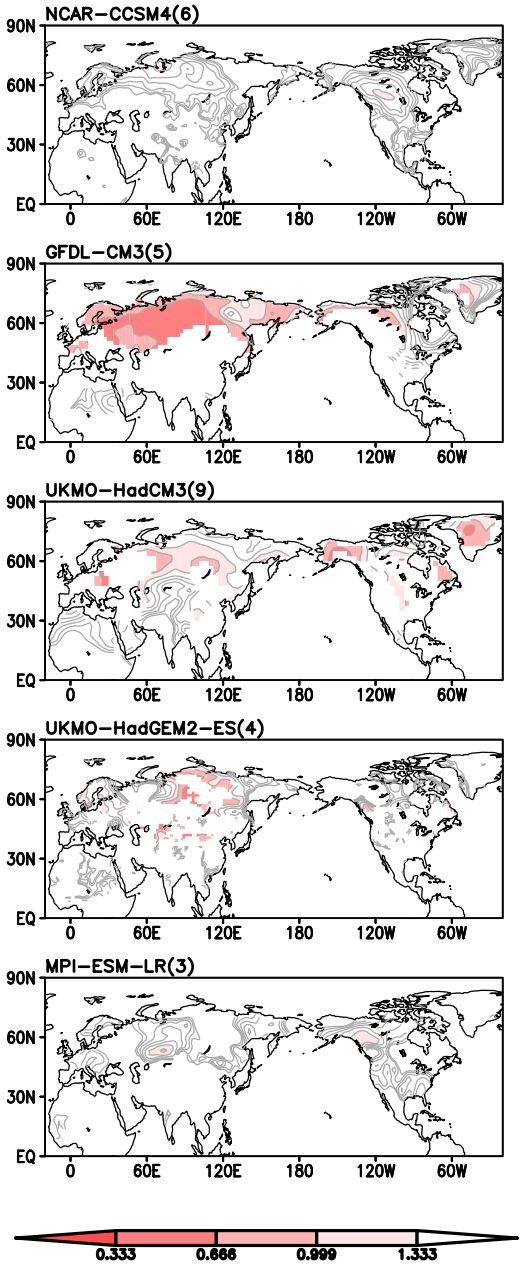


**Figure 2.6** Ratio of the ensemble-averaged winter SAT trend to the intra-ensemble standard deviation of the winter trend. The ratio is plotted only where the ensemble-

averaged winter trend is ≥ 0.5°C century$^{-1}$, i.e., only in the model-indicated secular warming regions. The linear trend over the 1902–2004 period is computed in all cases. The contour interval is 0.333, with values ≤ 1.333 shaded and heavier shading for smaller values. Smaller values (more reds) denote regions where the ensemble mean SAT trend is less robust. Smoothing is as in Figure 2.4.

### 2.4.4 Intra-ensemble spread of seasonal SAT trends

To assess the impact of period length on linear trends, the ensemble spread of the linear SAT trend in historical simulations from two IPCC AR5 climate system models—one from the United States (GFDL-CM3, with a 5-member ensemble) and the other from Europe (UKMO HadCM3, with a 9-member ensemble)—is displayed in Figure 2.7. The ensemble-averaged winter SAT trend is shown in the upper panels for the 1902–2004 (103 years, referred to as century-long) and 1860–2004 (145 years, referred to as century-plus) periods. Although weaker linear trends were expected in the longer period from the more limited aliasing of low-frequency variability (of natural or anthropogenic origin), the century-long period was itself viewed as being long enough to accommodate (and average out) the decadal-to-multidecadal-scale low-frequency variability such as Pacific decadal variability (Guan and Nigam 2008; Mantua et al. 1997) and Atlantic multidecadal variability (Guan and Nigam 2009; Kavvada et al. 2013), two widely documented and analyzed decadal–multidecadal climate variabilities. As such, further weakening of the linear trend in the longer, century-plus period, notably in polar latitudes of the GFDL simulations, was somewhat unexpected, especially for the ensemble-averaged trend since ensemble averaging can additionally filter low-frequency variability assuming a sufficiently large ensemble size (Sardeshmukh et al. 2000). The corresponding trends in the

HadCM3 simulations (Figure 2.7, right panels), in contrast, are relatively stable to the change in analysis period.

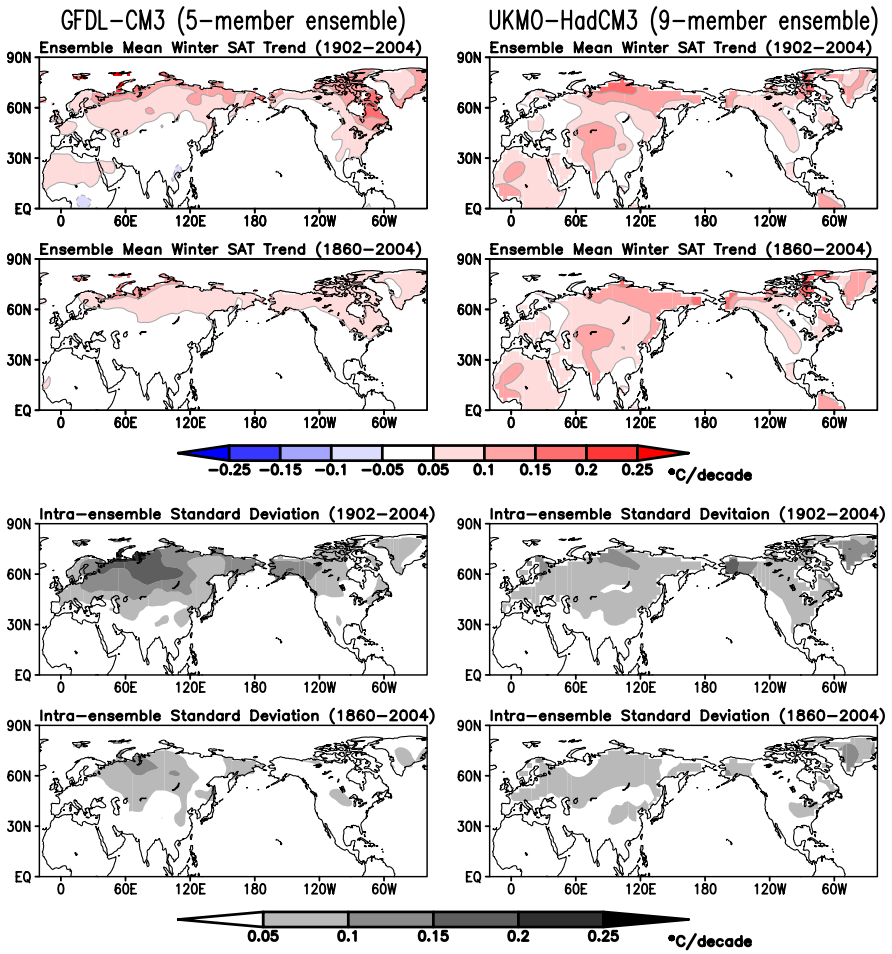


**Figure 2.7** Ensemble mean and intra-ensemble spread of the winter SAT trend in the GFDL-CM3 and UKMO-HadCM3 historical climate simulations (a 5- and 9-member ensemble, respectively). Two periods are analyzed: the twentieth century (1902–2004) as before, and the longer 1860–2004 period spanning the nineteenth and twentieth centuries to reduce potential aliasing of multidecadal variability in linear trends. The ensemble-mean SAT trends for the two periods are shown in color while the intra-ensemble spread of SAT trends is shown in black and white, with the GFDL ones always on the left. A uniform contour interval of 0.05°C decade$^{-1}$ is used in all panels, with contouring and shading threshold at 0.05°C decade$^{-1}$.

The intraensemble standard deviation (SD) of the century-long linear trend in the GFDL simulations is about twice as large as in the HadCM3 simulations,

especially over northern Eurasia, but the SD of the century-plus trend is quite comparable (Figure 2.7, lower panels). The impressive decline in the SD of the linear trend with increasing period length in the GFDL case indicates the presence of longer-than-centennial-scale low-frequency variability (or ultra-low-frequency variability) in its historical simulations, with related phase varying across ensemble members. The aliasing of this variability component into the century-long linear trend will depend on its phase in that century, but as all linear trends were computed for the same century (1902–2004), the ultra-low-frequency variability in the GFDL historical simulations is likely to be of ‘‘internal’’ origin (i.e., unforced).

The large intraensemble SD of the century-long linear SAT trend in the GFDL simulations, with the SD often larger than the ensemble-averaged trend in the middle-to-high northern latitudes (i.e., the very regions exhibiting the strongest ensemble-averaged trend or potential secular warming) is concerning as the large SD is indicative of significant internal variability in the modeled climate. Is this unforced component of climate variability (‘‘dynamical’’ noise) overwhelming the twentieth-century secular warming signal in the GFDL historical simulations?

The century-long linear winter SAT trends in each ensemble member of the GFDL historical simulations are shown in Figure 2.8 along with the ensemble-averaged trend (top panel) for easy reference. Of the five historical simulations, only run 2 yields quasi-realistic winter SAT trends. None of the simulations exhibit the pronounced winter warming trend over western-central Canada seen in observations (Figures 2.2 and 2.3). It would be interesting to examine the amplitude and phase of ultra-low-frequency variability in run 2 (quasi-realistic trends), run 4 (largely devoid

of trends), and run 5 (cooling trend over northwestern Eurasia).

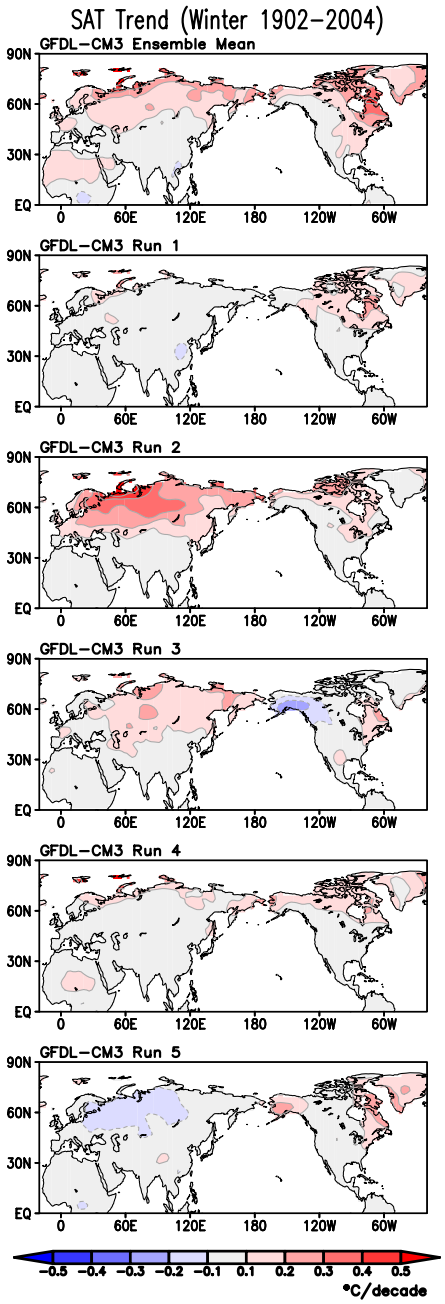


**Figure 2.8** Ensemble spread in the century-long winter SAT trend in GFDL-CM3's historical simulations of twentieth-century climate. The five-member ensemble-mean trend, as shown in Figure 2.7, is displayed at the top for easy reference. Contouring and shading are as in Figure 2.7.

## 2.5 Origin of the striking seasonality in observed SAT trends

The origin of the large seasonality of SAT trends over the northern continents is intriguing. Clearly, it is not the reduced $CO_2$ concentration in the agriculturally active summer season because this reduction, besides being small (~10ppm or ~3% of the average twentieth-century concentration), occurs each year, and thus cannot account for the smaller trend in summer SAT. Surface albedo feedback from continental snow and ice cover also cannot account for the larger winter trends notwithstanding their high-latitude focus as this feedback is muted in winter because of diminished solar radiation. Although this feedback is robust in summer, it is incapable of generating a delayed warming over continents (unlike oceanic regions, where heat sequestration leads to larger surface warming in winter). There is no corresponding heat storage and delayed release mechanism operative over continental regions (Manabe and Stouffer 1980).

The mechanisms generating regional and seasonal variation of the century-long SAT trends have yet to be elucidated. Most previous attributions of the seasonality of warming are based on the change and/or trends over multidecadal periods, ranging from 36 years (Wallace et al. 2012) to 60 years (Stine and Huybers 2012). Because of the potential for aliasing low-frequency climate variability into multidecadal trends (as discussed in section 2.4) and the winter robustness of this variability (manifest in circulation footprints as well), related thermal advection is implicated in the generation of stronger SAT trends over northern continents in boreal winter (Stine and Huybers 2012; Stine et al. 2009; Wallace et al. 2012; Wang et al. 2009). Multidecadal SAT trends have been attributed also to humidity advection (by

the same low-level circulation anomalies) and ensuing radiative impacts (Compo and Sardeshmukh 2009).

Two mechanisms for the striking seasonality in observed SAT trends are discussed: A new mechanism rooted in land surface–hydroclimate interactions is proposed in section 2.5.1 and a dynamical mechanism based on thermal advection by the secular change in circulation in section 2.5.2.

### 2.5.1 Land surface-hydroclimate interaction mechanism

A mechanism grounded in land surface–hydroclimate interactions is proposed for the large seasonality in SAT trends over the northern continents. In a column perspective, the change in the downward longwave radiative flux at Earth's surface from increased greenhouse gas concentrations—estimated at ~7W $m^{-2}$ per °C of annual mean warming from the IPCC AR5 models (Stephens et al. 2012)—must be offset, with the offsetting processes determining the new equilibrium surface air temperature. In winter when the hydrologic cycle over the northern continents is dormant (from a frozen land surface), this excess incident energy would have to be offset, primarily, by increased surface longwave emission (i.e., by raising surface temperature); any offsets by increased upward sensible heat flux would also entail raising surface temperature. If the same amount of excess longwave radiation was incident in summer, it could be disposed of, additionally, by increased continental evapotranspiration and snowmelt, that is, without raising the surface temperature as much as in winter. If this were the case, a larger secular trend in summer evapotranspiration, and late spring and fall snowmelt, should be found in regions exhibiting large seasonality in SAT trends (Figure 2.4, top-right panel).

Of the two, longer historical records are available for evapotranspiration (1902–2014); snow cover extent records begin only in the mid-1960s (Estilow et al. 2015) and snowmelt records remain unavailable, precluding their use in this preliminary investigation of the large seasonality in century-long SAT trends. Although evapotranspiration estimates are available since the early twentieth century, the diagnosis of evapotranspiration is not without some uncertainties (Nigam and Ruiz-Barradas 2006). For these reasons, trends in precipitation—a directly measured/ monitored quantity—are examined first. Figure 2.9 indeed shows larger century-long precipitation trends in summer over some of the pertinent North American regions. However, as the regional atmospheric water cycle also involves moisture transports (Nigam and Ruiz-Barradas 2006), the larger summer precipitation trends noted above are not necessarily indicative of increasing regional evapotranspiration but certainly encouraging of further analysis.

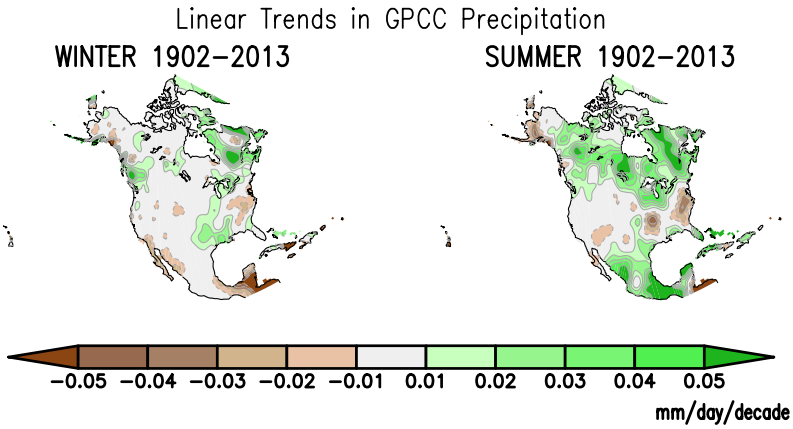


**Figure 2.9** Linear trends in winter (left) and summer (right) precipitation over 1902-2013 from GPCC. Fields are shown after nine applications of smth9.

The century-long (1902–2014) winter and summer evapotranspiration trends from the University of Delaware diagnosis (Willmott et al. 1985) are shown in Figure 2.10, and the summer-minus-winter difference in Figure 2.11 in green/brown. The

differences are large over western-central Canada and the northern-central Great Plains, notably the southern Mackenzie Plain (i.e., southward of Great Slave Lake and westward of Lake Athabasca), the Canadian Shield, and the northern Great Plains—interestingly, the very regions where the seasonal difference in SAT trends is large. To facilitate recognition of the extent of overlap of the regions exhibiting large seasonality in the evapotranspiration and SAT trends, the winter-minus-summer SAT trends are overlaid in red in Figure 2.11. The extent of geographical overlap is impressive, particularly in terms of the broad overlap of red contours with the green shaded region in western-central Canada. Although spatial correlation, which quantitatively measures the correspondence of field departures from their regional average (i.e., of more granular structures), is not a suitable measure of regional-scale overlap, note that it is 0.33 for region 2 (marked in Figure 2.4, top-left panel), for reference. Nonetheless, this is promising for the attribution of the winter–summer differences in century-long SAT trends to land surface–hydroclimate interactions permitted by the seasonal hydrologic state of the middle- to high-latitude continents.

The proposed mechanism is energetically viable: The average summer-minus-winter evapotranspiration trend in the overlap regions of Figure 2.11 is estimated to be ~0.175mm day$^{-1}$ century$^{-1}$, a value in between the second and third green contours. The energy needed for fueling additional evapotranspiration in summer is estimated using the latent heat of condensation as $\{0.175\ mm\,day^{-1}century^{-1}\}\times\{1000\ kg\,m^{-3}\}\times\{2.5\times10^{6}\ J\,kg^{-1}\}$, yielding $4.375\times10^{5}\ Jm^{-2}day^{-1}$ or $\sim5.0\ Wm^{-2}century^{-1}$.

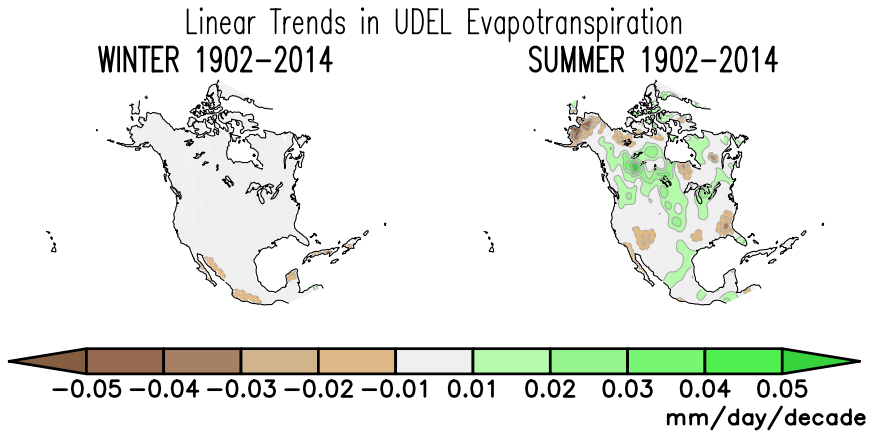


**Figure 2.10 Linear** trends (mm day$^{-1}$ decade$^{-1}$) in winter (left) and summer (right) evapotranspiration over 1902-2014 from University of Delaware. Fields are shown after nine applications of smth9.

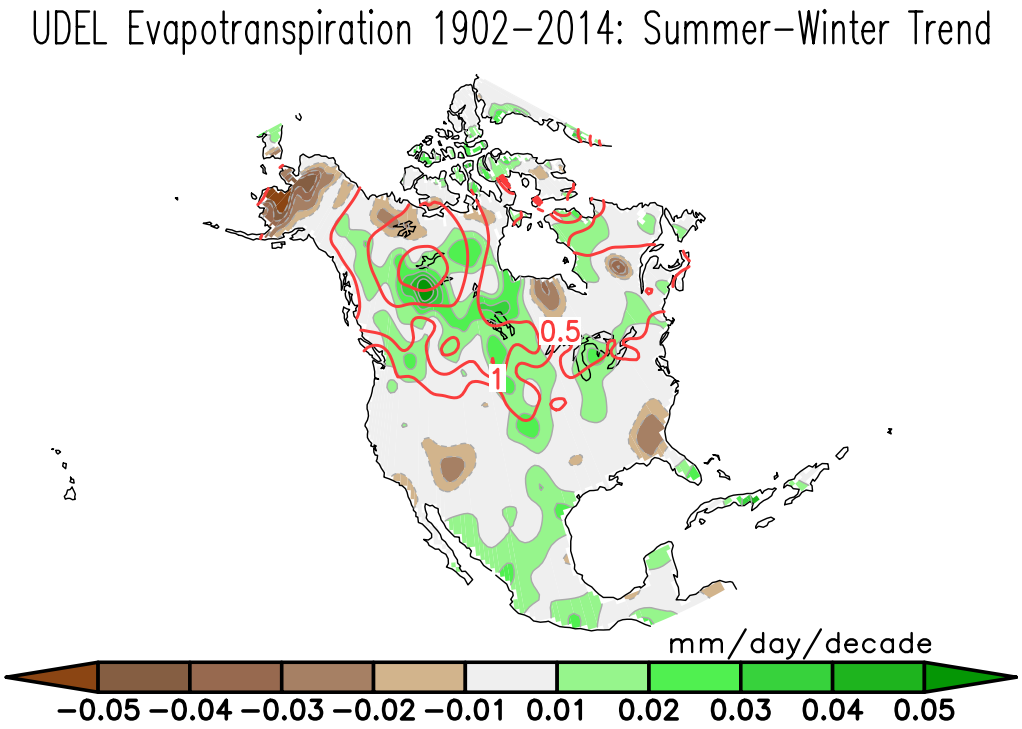


**Figure 2.11** Summer-minus-winter evapotranspiration trends (shaded green/brown) with overlaid winter-minus-summer SAT trends (contoured in red) for the same 1902–2014 period. Note the opposite seasonal differencing of the two trends. Evapotranspiration is from the University of Delaware while the surface air temperature is from the CRU TS4.00 dataset and contoured with an interval of 0.5°C century$^{-1}$. All fields are shown after nine applications of smth9.

Is this latent energy consumption energetically consistent with the summer reduction in SAT trends (by ~1.25 °C century$^{-1}$ in the overlap regions)? The complexity of the climate system and the absence of extended records of surface energy flux measurements preclude an observationally rooted answer. We thus seek the assistance of climate models, notwithstanding their imperfections (cf. Figure 2.4), in relating surface energy consumption/deposition with SAT trends. The IPCC AR5 models indicate a ~7W m$^{-2}$ increase in downward surface longwave radiative flux for every 1.0 °C century$^{-1}$ of warming (Stephens et al. 2012). Using this measure, albeit for global and annual-mean model responses, a 1.25 °C century$^{-1}$ reduction of winter SAT trend (to bring it down to the summer value) will require latent disposition of ~8.75W m$^{-2}$ century$^{-1}$, that is, more than the ~5.0Wm$^{-2}$ century$^{-1}$ estimated from the observed winter-to-summer increase in evapotranspiration trends. Interestingly, this discrepancy, especially the larger winter-to-summer latent disposition estimate, was anticipated because the winter warming has been attributed both to radiative and dynamical effects but with the dynamical contribution deemed insufficient in accounting for the seasonal differences in SAT trend over the northern continents (Stine et al. 2009). Without the dynamical contribution, which is significant only in winter, the winter-minus-summer SAT trend would be smaller, leading to a smaller winter-to-summer latent disposition requirement—one more in line with the ~5.0W m$^{-2}$ century$^{-1}$ estimate developed from seasonal differences in evapotranspiration trends.

The winter dormancy of the continental hydrologic cycle is central to the proposed mechanism. The correspondence between the seasonal differences in SAT

and evapotranspiration trends is thus sought only over the middle- to high-latitude continents where the winter dormancy condition is met. As such, the lack of overlap of the trend differences over the southern tier states, Mexico, and Central America in Figure 2.11 does not undermine the proposed mechanism.

The strikingly different seasonal states of the hydrologic cycle over the middle- to high-latitude continents—winter dormancy and summer vigor—can impart a pronounced seasonality to the secular warming of these continental regions, as indicated by this analysis of the century-long observational datasets. Clearly, this mechanism needs corroboration, in addition to the evaluation of other impacts on long-term SAT trends (e.g., from the cloud cover, specific humidity, snow cover extent, snowmelt, and permafrost variations and trends).

### 2.5.2 Dynamic contribution to the century-long SAT trends

The dynamical contribution to secular warming refers to the warming component arising from circulation change rather than radiative forcing (Wallace et al. 2012). Most previous estimates of this contribution are based on analyses of the changes/ trends over multidecadal periods ranging from 36 to 60 years (Compo and Sardeshmukh 2009; Stine and Huybers 2012; Stine et al. 2009; Wallace et al. 2012; Wang et al. 2009), and, as such, are prone to the aliasing of low-frequency climate variability into multidecadal trends. The dynamical contribution to multidecadal SAT trends is, in part, rooted in this aliasing, and its seasonal sensitivity rooted in the winter robustness of low-frequency variability and related thermal advection.

The attribution of the seasonality in century-long trends should be more straightforward, in part, from the reduced aliasing of low-frequency variability into

centennial trends. The 113-yr period analyzed here is longer than the known periods of low-frequency climate variability (subdecadal to multidecadal), limiting potential aliasing. The dynamical contribution to the century-long SAT trends could, however, still be significant, not from continued aliasing but from the secular trends in seasonal circulation—the basis for dynamical contribution in this analysis.

The dynamical contribution to multidecadal (1965–2000) SAT trends was evaluated by Wallace et al. (2012), who used regressions of monthly sea level pressure on the hemispheric-averaged (40°–90°N) continental winter SAT to identify the influential SLP pattern. Projections of monthly SLP on this pattern generated an SLP index, which was then regressed out of SAT, with the deficit revealing the dynamical contribution. This strategy was not adopted here for the following reasons:

- The influential SLP pattern cannot be a surrogate for just the dynamical contribution, as it must include a component from the secular warming of the planetary boundary layer, that is, a thermal part reflecting hydrostatic balance. Removing this SLP pattern's entire influence from SAT is overkill. [Targeting SLP gradients, i.e., circulation directly, would have been preferable.]
- The SLP pattern, obtained from contemporaneous regressions (Wallace et al. 2012), cannot be entirely viewed as a ‘‘predictor’’ of the dynamical influence on concurrent SAT.
- The century-long SAT trends exhibit coherent, regional structures (Figure 2.2); extensive spatial averaging (e.g., hemispheric) can thus weaken the contribution of regional thermal advection.

The dynamical contribution is assessed here by focusing directly on the SLP trend, from whose gradients the geostrophic wind trend ($V_{g\_trend}$ in units of m $s^{-1}$ $decade^{-1}$) is inferred. The climatological SLP from the HadSLP2 dataset (Allan and Ansell 2006) with its prominent winter features—the Siberian high (>1028 hPa), Aleutian low (<1008 hPa), and Icelandic low (<1006 hPa)— is displayed in Figure 2.12 (top panel), along with the century-long trends (shaded). The SLP trends exhibit coherent regional structure, suggesting a slight northeastward shift of the Aleutian low in view of the 1–2 hPa drop-off of SLP over Alaska and the Yukon Territory, and modest weakening of the Icelandic low by 2–3 hPa over the twentieth century; in contrast, SLP trends are weak over Europe and Asia. The structure of the twentieth-century SLP trends in the Western Hemisphere indicates a southeasterly geostrophic wind trend over northern North America, with the exception of Alaska and the Yukon Territory, where the wind trends are northwesterly to westerly.

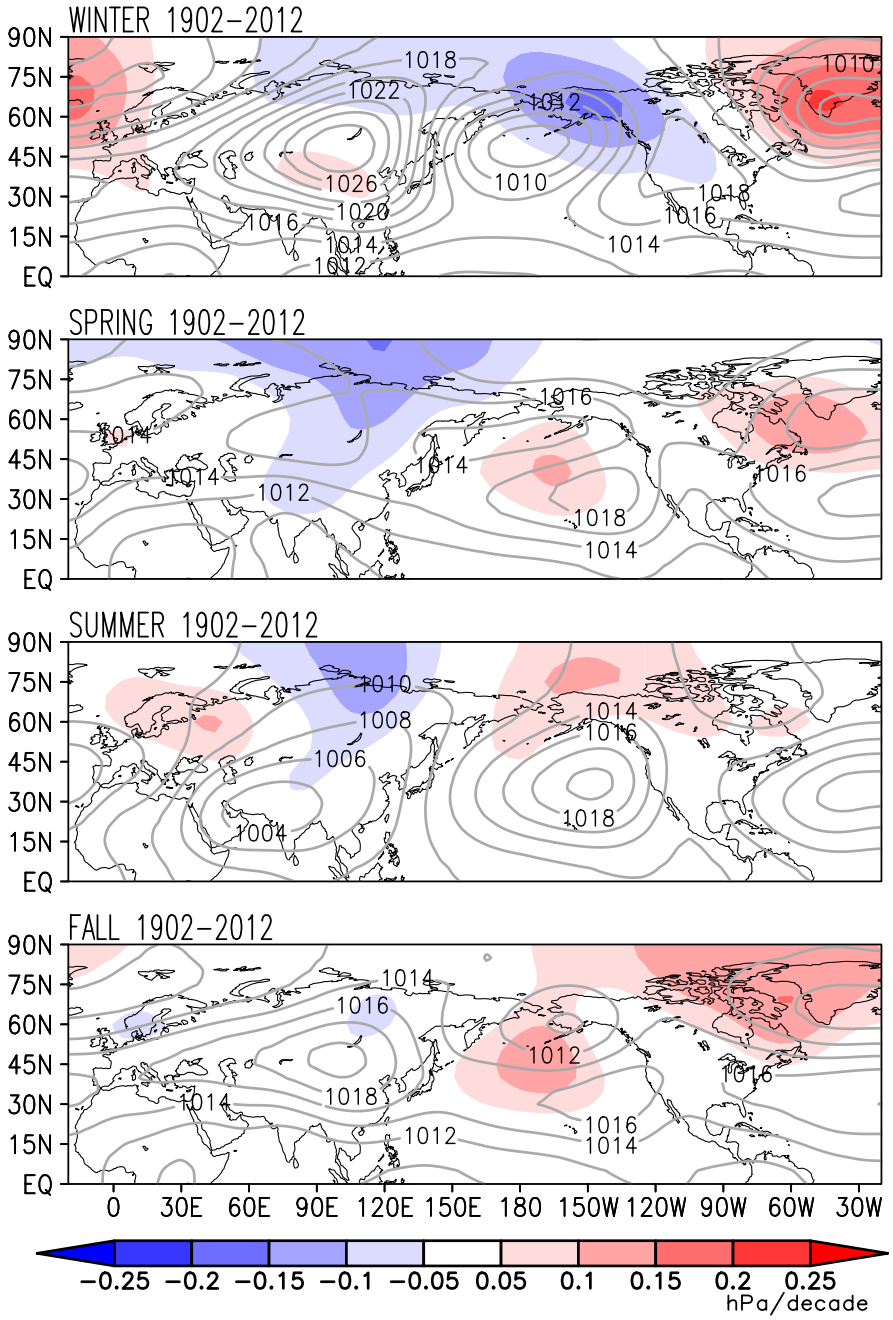


**Figure 2.12** Climatological SLP and SLP trend in the Northern Hemisphere. The climatological (1902–2012) SLP is contoured with a 2.0-hPa interval, while the SLP trend is shaded with an interval of 0.05 hPa decade$^{-1}$. The HadSLP2 data are analyzed and plotted after nine applications of the nine-point smoother (smth9).

The SLP trends are much weaker in spring and summer over northwest North America (Figure 2.12), a region exhibiting notable seasonal differences in century-

long SAT trends (the red contoured region in Figure 2.11, or top right panel in Figure 2.4). The weakness of SLP trends and, more importantly, their horizontal gradients in spring and summer indicate the relative insignificance of the dynamical contribution to SAT trends in these seasons. This too is interesting as it provides a discriminating seasonal phase space for resolving the contributions of land surface–hydroclimate interactions and dynamical advection in seasonal secular warming over northern North America.

Thermal advection anomaly $(-V \cdot \nabla T)$ is the sum of three terms: $(-V_{trend} \cdot \nabla T_{clim})$, $(-V_{trend} \cdot \nabla T_{trend})$, and $(-V_{clim} \cdot \nabla T_{trend})$, where $V_{trend}$ and $T_{trend}$ are the low-frequency variability related low-level wind and temperature anomaly, and $V_{clim}$ and $T_{clim}$ are the climatological low-level wind and temperature. The first and third terms are linear in anomaly while the second (self-advection) is nonlinear and, often, much smaller than the other two. Interestingly, $T_{trend}$ can be reasonably reconstructed from thermal advection during winter variability episodes (Baxter and Nigam 2015). The essentially linear thermal advection is thus a surrogate for $T_{trend}$, with the first term being a clear dynamical contribution to the temperature anomaly. The same cannot be said for the second and third terms, especially if diabatic heating (e.g., radiative forcing in context of secular warming) is also contributing in generation of the temperature anomaly $T_{trend}$. The dynamical contribution is positive for warm advection (i.e., when the low-level circulation anomalies are from southward latitudes or adjoining oceans). The impact of the low-level circulation anomalies on SAT trends is often referred as the dynamical contribution.

Figure 2.13 plots the first term of the thermal advection tendency $(-V_{trend} \cdot$

$\nabla T_{clim}$), or the advection of climatological temperature by the trend in winds. As inferred from the SLP trends (Figure 2.12), southerly flow in central Canada in winter leads to a warm thermal advection tendency in this region. In summer, thermal advection tendency is minimal over northwestern North America, with contributions only in the southwestern United States and Mexico.

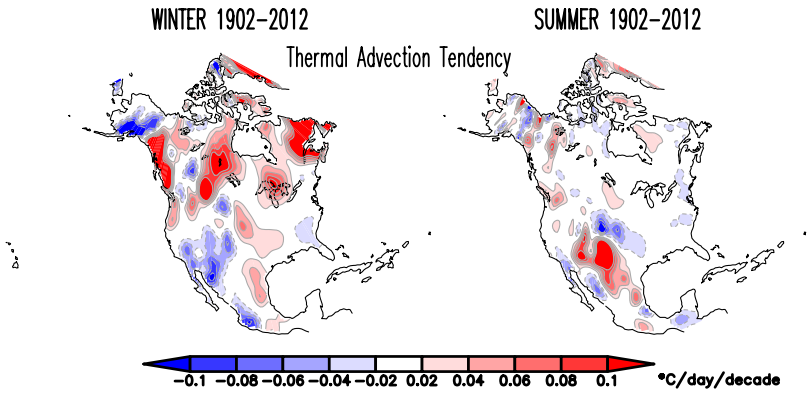


**Figure 2.13** Thermal advection tendency ($-\boldsymbol{V_{trend}} \cdot \boldsymbol{\nabla T_{clim}}$) for winter (left) and summer (right) 1902-2012. Contour and shading interval is 0.02 °C day$^{-1}$ decade$^{-1}$.

As discussed in section 2.2.5, a linear damping of temperature is assumed to convert thermal advection tendency to the dynamical contribution to temperature trends. The dynamical contribution to the seasonality of secular warming over North America ($T_{t\_dyn}$) is shown in Figure 2.14 with red-blue contours. The contribution to the winter-minus-summer SAT trends is distributed widely over the continent; that is, it extends well beyond the northern half where the seasonality of century-long SAT trends is concentrated (red contoured region in Figure 2.11) and where the winter–summer difference of evapotranspiration trends is also focused (green/browns in Figure 2.11 or 2.14). Interestingly, the dynamical component often complements the

evapotranspiration one over the northern continent, as indicated by the structure of the two contributions in Figure 2.14:

- Focusing on the prominent feature of the dynamical contribution—the warming extending southwestward from the Nunavut Territory into Saskatchewan and Montana, with a prominent center over the Reindeer Lake (Figure 2.13)—one notes the weakness of the evapotranspiration contribution around Reindeer Lake and over northern Nunavut, the regions where it was unable to account for the observed seasonality of SAT trends (~1°C century$^{-1}$, cf. Figure 2.11). The complementary dynamical contribution remedies this accounting deficit.
- Focusing now on the prominent feature of the evapotranspiration contribution—the regional maximum centered on the southern Mackenzie Plain (i.e., southward of Great Slave Lake and westward of Lake Athabasca; Figure 2.13)—one notes the weakness of the dynamical contribution, especially over the southwestern Mackenzie Plain where this contribution is not only weak but also offsets the evapotranspiration contribution. In this region, where the seasonality of SAT trends is strongest (~2°C century$^{-1}$; cf. Figure 2.11), the dynamical contribution is insignificant and the evapotranspiration one dominant. Farther to the south, however (i.e., over southwestern Saskatchewan and northern Montana), the two contributions become comparable.

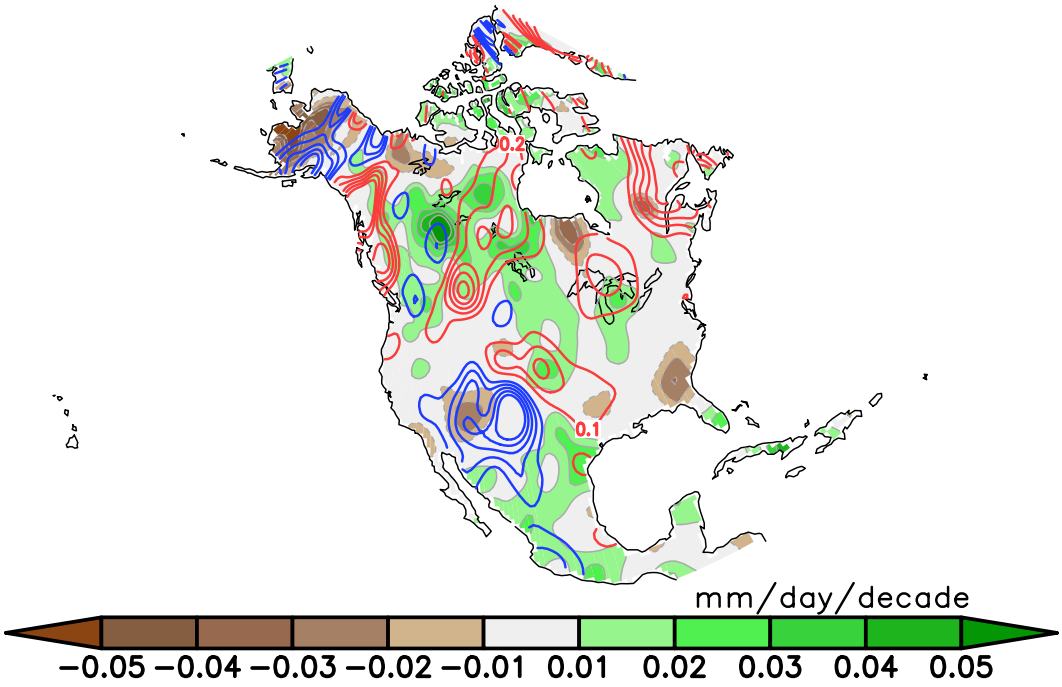


**Figure 2.14** The dynamical contribution to the 1902–2012 winter-minus- summer SAT trend is shown in red (positive) and blue (negative) contours, with an interval of 0.1°C decade$^{-1}$. It is superposed on the evapotranspiration contribution (shaded green/brown, exactly as in Figure 2.11) to recognize regions of complementary and supplementary contributions.

## 2.6 Conclusions

Secular warming of the northern continents is a well-studied topic as it typically involves computation of the linear trend—an elemental mathematical operation—on the near-surface air temperature (SAT) record, a meteorological variable measured with varying degrees of precision since the eighteenth century. The twentieth century linear trend in annual SAT is a widely used marker of secular warming, and its sensitivity to SAT analysis, analysis period, and computation methodology (e.g., minimization of least squares or absolute distance) have all been assessed in numerous studies.

Somewhat less studied is the striking seasonality of the observed twentieth-

century SAT trends, the focus of this analysis. Why is this easily characterized seasonality of interest? To begin with, the large seasonal variation of climate over the Northern Continents provides multiple base states for the expression of secular warming. The resulting seasonal variation in century-long SAT trends—shown to be remarkable, especially over North America and central-eastern Asia—can provide rare insights into the dynamical and thermodynamical processes generating secular warming over the land surface. No less important is the exceptional opportunity provided by this seasonality—an expanded climate phase space—for vetting climate projection models without additional model integrations, a cost effective evaluative opportunity that remains largely untapped.

Two mechanisms for the large seasonality of the century-long SAT trends over the northern continents are investigated, including a new one based on land surface–hydroclimate interactions. The new mechanism posits the relative weakness of the summer trends to the ‘‘awakened’’ hydrologic state in summer, following winter–spring dormancy. An active hydrologic cycle brings into play land surface processes that can potentially offset the additional longwave radiation incident on the land surface from increasing greenhouse gas concentrations. Whereas the offset is primarily from increased surface longwave emission in winter (thereby raising surface air temperature), observational evidence is presented for latent disposal in summer through increased evapotranspiration (i.e., without necessarily raising surface temperature); this disposal mechanism is, of course, not available in winter when the hydrologic cycle is dormant. An estimate of the power needed to fuel the observed positive trend in summer evapotranspiration was, moreover, shown to be in accord

with estimates of the additional longwave radiative energy incident on Earth's surface from increasing greenhouse gas concentrations. The land surface–hydroclimate interaction mechanism merits closer scrutiny from analysis of additional observational and simulation datasets.

The seasonality of SAT trends was hitherto attributed to the warming component generated by circulation variability and change (the dynamical contribution) rather than to greenhouse radiative forcing (Wallace et al. 1995; Wallace et al. 2012); the contribution is seasonally sensitive in view of the winter robustness of low-frequency variability and related thermal advection. Most previous assessments of the dynamical contribution were, however, in the context of multidecadal (and not century-long) SAT trends and, as such, impacted by aliasing of low-frequency variability. The dynamical contribution, calculated here, from century-long trends in low-level circulation, was found to be relatively modest and, interestingly, often complementary to the evapotranspiration contribution.

The spring-to-summer reduction in the century-long SAT trends over North America (Figure 2.2), that is, across two seasons exhibiting insignificant SLP trends over the continent (Figure 2.12), reiterates the limited reach of the dynamical mechanism in generating the seasonality in SAT trends.

According to this analysis, the leading climate models (whose simulations inform the IPCC's Fifth Assessment Report) are currently unable to generate realistic and robust (large signal-to-noise ratio) twentieth-century winter and summer SAT trends over the northern continents. Is this due to deficiencies in representation of dynamic or thermodynamic processes, or both? Answering this will require detailed

analysis of various model outputs. As a preliminary investigation, Figure 2.15 shows the ensemble mean of the century-long precipitation trends in the five AR5 models for both winter and summer. Comparing the spatial structure of these trends with the observed ones (Figure 2.9) reveals varied and often unrealistic representations. There are no increases in summer precipitation in the GFDL CM3 or either of the UKMO models. The CCSM4 and MPI-ESM-LR do show increased summer precipitation over North America, but it is displaced northwestward relative to observations. Again, this does not necessarily imply that evapotranspiration trends are not represented well in the models, but offers some indication that thermodynamic processes may be lacking. Elucidating why the observed models do not capture the observed SAT trend seasonality will require further research.

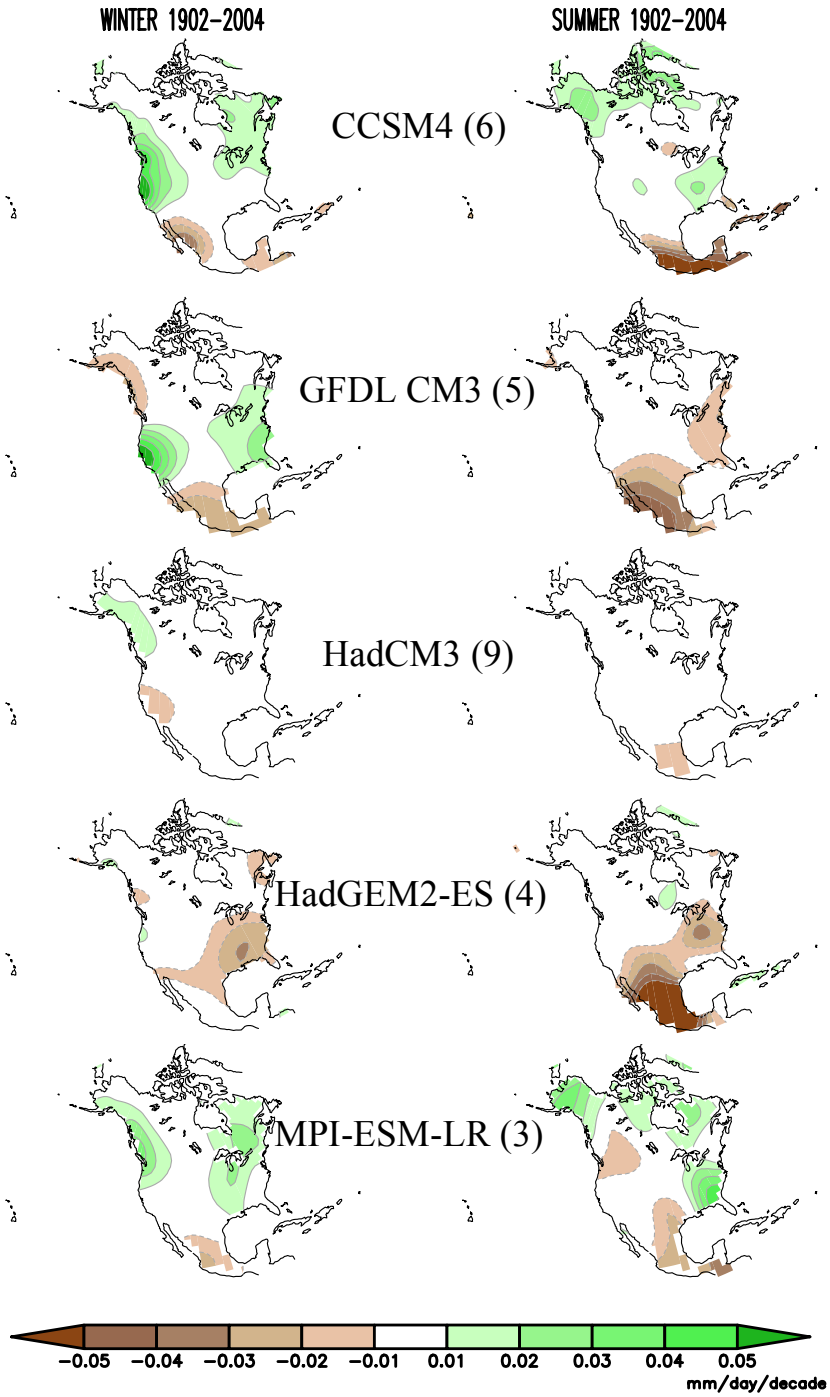


**Figure 2.15** The linear precipitation trend (mm day$^{-1}$ decade$^{-1}$) for (left) winter and (right) summer in five IPCC-AR5 model simulations of twentieth century climate (1902–2004). The number of ensemble members in each simulation is noted in parentheses. Shading and contour interval is 0.01 mm day$^{-1}$ decade$^{-1}$.

The relative contribution of both mechanisms to the observed seasonality in century-long SAT trends needs further assessment because of uncertainties in the diagnosis of evapotranspiration and sea level pressure from the century-long observational records. Climate system models—ideal tools for investigation of mechanisms through controlled experimentation—are unfortunately not yet ready given their inability to simulate the seasonality of trends in historical simulations.

# Chapter 3: Seasonality in upper-air temperature trends over North America[2]

## 3.1 Background

The steep warming trend in surface air temperature (SAT) during recent decades and its origin are being actively investigated (DelSole et al. 2011; Stolpe et al. 2017). A noteworthy feature of this trend is the lack of uniformity across seasons, with some regions exhibiting a striking difference in the winter and summer SAT trends (Chapter 2; Nigam et al. 2017). For example, the winter trend relative to other seasons is notably large in the middle-to-high latitudes of the Northern Continents (Wallace et al. 2012), particularly over northwestern North America and northern Eurasia. In Chapter 2, the SAT trend seasonality was attributed to both dynamic and thermodynamic mechanisms. Dynamically, changes in winter circulation and related thermal advection strengthen winter SAT trends (Stine et al. 2009; Wallace et al. 2012). Thermodynamically, increased evapotranspiration in summer leads to a latent disposition of energy, reducing temperature trends in summer as compared to winter, when the hydrologic cycle is dormant (Nigam et al. 2017).

Here, the seasonality of the secular trend in *upper-air* temperatures is characterized over northern Canada, a region exhibiting pronounced seasonal variation in SAT trends (see Figure 2.2). Specifically, the goal is to further examine the causes of the surface seasonality via trends in temperatures aloft.

[2] This chapter has been submitted to *Climate Dynamics* as Thomas, Ravi and Nigam (20XX). It is currently under review.

The annual-mean temperature trend over recent decades is generally positive in the troposphere and negative in the stratosphere (Hartmann et al., 2013) – the canonical secular warming structure. The cooling trend in the stratosphere is well documented (Ramaswamy et al. 2001; Randel et al. 2009; Seidel et al. 2011) as is its seasonal variation: In Polar Regions, strong springtime cooling and weak wintertime warming lead to large seasonality in stratospheric temperature trends (Ivy et al. 2016; Randel et al. 2009; Seidel et al. 2011; Thompson and Solomon 2005). The seasonality is weaker in the tropical stratosphere, with minimal cooling in spring and maximum cooling in winter and fall (Free 2011; Fu et al. 2010; Thompson and Solomon 2005). The seasonality in stratospheric trends has been attributed to both radiative and dynamic causes (Bohlinger et al. 2014). The strengthening (weakening) of the Brewer-Dobson Circulation (Cohen et al. 2014b) in boreal winter (spring) leads to enhanced (reduced) downwelling at high latitudes and thus less (more) stratospheric cooling (Fu et al. 2010; Ivy et al. 2016; Young et al. 2012). Ozone loss in summer is the main driver of summer cooling trends in Polar Regions (Ivy et al. 2016). Sea surface temperatures have also been implicated in stratospheric temperature trends. Garfinkel et al. (2015) found that about half of the spring cooling trend in the polar stratosphere could be attributed to SST forcing.

Tropospheric temperature trends have also drawn attention, particularly with regard to why they differ from the surface temperature trends (Thorne et al. 2011). Frierson (2006) examined AR4 simulations and found that, as a result of global warming, the upper troposphere warms more than the lower troposphere in the mid-latitudes. In the tropical troposphere, there has been debate about whether

observations and models agree (Douglass et al. 2008; Santer et al. 2008). Due to a better understanding of uncertainty, it was concluded that there is no evidence of disagreement between models and observations on the enhancement of warming in the tropical upper troposphere (Thorne et al. 2011). Screen et al. (2012) examined tropospheric warming in the Arctic, noting more pronounced warming in fall and winter than in spring and summer. Lanzante et al. (2003a) studied upper-tropospheric trends over 1979-1997 and found greater warming during fall for the Northern Hemisphere. Apart from a few regional studies on the seasonality of tropospheric trends (Gevorgyan 2014; Kothawale and Singh 2017; Zhang and Zhou 2013), their seasonal structure in the Northern Extratropics remains largely undocumented.

## 3.2 Data and methods

### 3.2.1 Observational Data

Multiple analyses of upper-air temperature were analyzed in this study. Primary focus is on the UK Met Office's HadAT2 dataset (Thorne et al. 2005). This dataset provides monthly temperature anomalies for 850-hPa up to 50-hPa relative to the 1966-95 climatology and is available from https://www.metoffice.gov.uk/hadobs/hadat/hadat2.html. Data are available at 676 stations worldwide for the 1958-2012 time period. Stations were excluded if they 1) were in coastal areas, 2) were missing 10 or more years of data in either winter or summer, or 3) were outside the region of maximum surface temperature trend seasonality in Northwestern Canada (i.e., where the difference between near-surface temperature trends in winter and summer is ~0.5° C decade$^{-1}$). Thus, the five stations

used in this study are Fort Nelson (WMO-71945), Fort Smith (WMO-71934), Whitehorse (WMO-71964), Normal Wells (WMO-71043) and The Pas (WMO-71867).

The RAOBCORE-v1.5 data set (Haimberger 2007; Haimberger et al. 2012) provides adjusted temperature anomalies on a 10° resolution grid for 1958-2014 and is available at http://www.univie.ac.at/theoret-met/research/raobcore/. The IUK (iterative universal kriging) Radiosonde Analysis Project (Sherwood and Nishant 2015), version 2.01 is also analyzed. This dataset provides monthly temperature estimates at 527 stations worldwide for the 1960-2015 time period and is available from http://web.science.unsw.edu.au/~stevensherwood/radproj/index.html.

Finally, upper-air temperatures were examined from the National Climatic Data Center's RATPAC-B (Radiosonde Atmospheric Temperature Products for Assessing Climate B) dataset (Free et al. 2005; Lanzante et al. 2003a, 2003b). This monthly dataset combines 00Z and 12Z observations for 85 stations around the globe and is available from http://www1.ncdc.noaa.gov/pub/data/ratpac/ratpac-b/ for the 1958–present period. The RATPAC-B data set does not have stations in the main region of interests for this study, so comparison is done at alternative stations.

Upper-air temperatures and geopotential heights were also obtained from NOAA's National Centers for Environmental Prediction (NCEP) atmospheric reanalysis (Kalnay et al. 1996) which is available at monthly resolution from January 1949 to present from http://iridl.ldeo.columbia.edu/SOURCES/.NOAA/.NCEP-NCAR/.CDAS-1/.MONTHLY/.

Near-surface air temperature trends over continental regions are calculated using the monthly Climate Research Unit Time Series (CRU-TS) version 4.00 dataset (Harris et al. 2014) – see section 2.2.1.

### 3.2.2 Analysis Method

Seasonal data is analyzed with the seasons defined in the boreal sense: winter is the average of December, January and February (DJF), and summer is the average of June, July and August (JJA). Linear trends are computed from linear least squares regression. We examine trends in temperature averaged over the five chosen HadAT2 stations rather than at individual stations. Trends over the five stations were computed by taking the trend of the average seasonal temperature from the stations. We found that reversing this computation (i.e., taking the average of the individual seasonal trends from each station) yielded minimal differences.

### 3.3.3 Statistical Significance

Statistical significance of trends was estimated at confidence levels from the ratio of the slope and its standard error, accounting for temporal autocorrelation in the temperature time series by using an effective sample size in both the computation of the standard error and in the indexing of the critical t-value (Santer et al. 2000). Significance is noted at both the 95% and 90% levels in this study. Statistical significance of trend differences was estimated by determining whether the trend in the difference time series is significantly different from zero at a given confidence level, as in Santer et al. (2000).

## 3.3 Seasonality of surface temperature trends over Northern Hemisphere continents

The pronounced seasonality in the 20$^{th}$-century (1902-2014) surface air temperature (SAT) trends, especially over North America and parts of Eurasia, is extensively documented in Nigam et al. (2017) and in Chapter 2 of this thesis. The focus in this chapter is on the region in Northwestern Canada, given the very robust SAT trend seasonality. On a century-long time scale, this seasonality in secular surface warming was attributed to land-surface–hydroclimate interactions and to changes in low-level atmospheric circulation (see section 2.5). At the surface in this middle-high latitude region, the hydrologic cycle is active in summer and dormant in winter. The positive trend in summer evapotranspiration in this region, as documented in Nigam et al. (2017), leads to latent disposition of energy and hence summer temperature trends that are reduced relative to other seasons. Furthermore, the secular change in low-level atmospheric circulation and related thermal advection simultaneously leads to increased winter trends in this region (Wallace et al., 2012; Nigam et al., 2017). Thus, the seasonality at the surface in northwestern Canada is consistent with both thermodynamically reduced summer trends and dynamically increased winter trends.

The present analysis, targeting upper-air temperature trends in this region, is of necessity restricted to the post-International Geophysical Year (IGY; http://www.nas.edu/history/igy/) period (1958-2012) when upper-air meteorological data began to be routinely collected. It is instructive to examine if the linear SAT trends in this comparatively shorter time period continue to exhibit the large

seasonality over Northern Continents that was highlighted in Chapter 2. Figure 3.1 displays the winter-minus-summer difference in SAT trends in this period from both CRU-TS4.00 data and NCEP Reanalysis. Over this shorter (55-year) period, northwestern North America has warmed more in winter, as evident from the large winter-summer trend difference (as much as 0.5°C decade$^{-1}$) there. A comparison with Figure 2.2 shows that the trend seasonality is, if anything, more intense in the shorter period.

The right panel in Figure 3.1 displays the winter-summer trend difference in the 925-hPa temperature from NCEP Reanalysis – whose upper-air analysis we seek to tap in addition to the HadAT2 radiosonde data. The two show broad similarities in the winter-minus-summer temperature trend structure over Northern Continents, and especially northwestern North America.

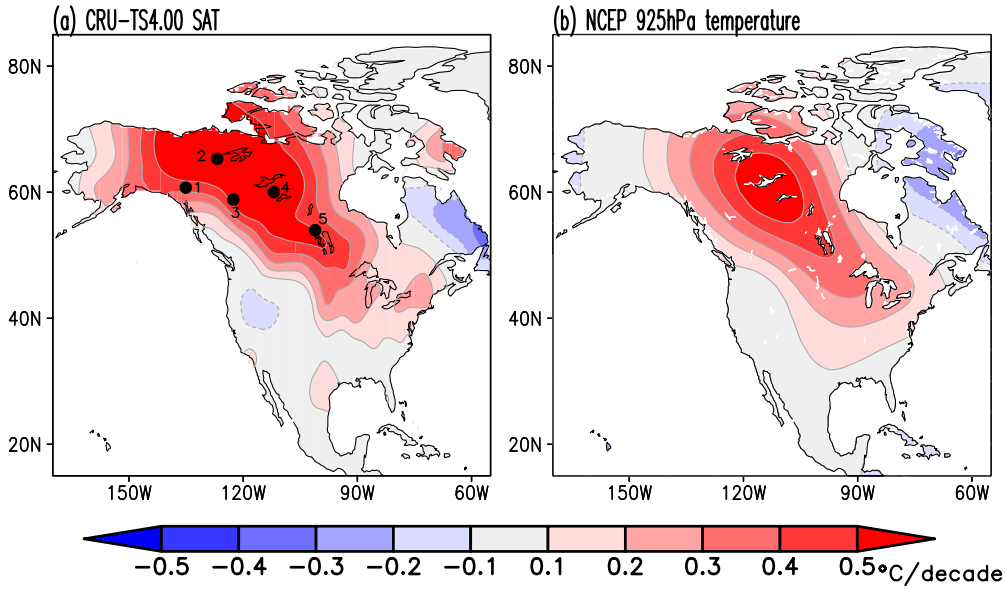


**Figure 3.1** Difference between the winter and summer temperature trends in the 0.5° resolution CRU-TS4.00 surface air temperature (SAT, left) and 2.5° resolution NCEP 925-hPa temperature (right) over North America during 1958-2012. Contour interval and shading threshold is 0.1°C decade$^{-1}$. The fields are shown after 9 applications of the 9-point smoother (*smth9*) in GrADS. The black dots mark the locations of the five HadAT2 radiosonde stations analyzed in this study: Whitehorse (1; WMO#71964), Norman Wells (2; WMO#71043), Fort Nelson (3; WMO#71945), Fort Smith (4; WMO #71934), and The Pas (5; WMO#71867).

## 3.4 Vertical structure of seasonal temperature trends from radiosonde soundings

### 3.4.1 Comparison of HadAT2 and RATPAC-B

In order to assess the reliability of the HadAT2 radiosonde data, we compared it with the independently analyzed RATPAC-B data. The stations used for comparison are Annette Island (WMO-70398), Baker Lake (WMO-71926), Moosonee (WMO-71836), and Dodge City (WMO-72451). These locations were chosen, despite being on the periphery of the region of interest, because they are the closest ones that have data from both RATPAC-B and HadAT2. Figure 3.2 shows the winter and summer temperature trends from each of these four stations from both radiosonde data sets.

There are differences in the stratosphere in winter at station 70398 (B) and in the troposphere in winter at station 71926 (A). However, apart from these discrepancies, the general structure of winter and summer trends is consistent between the two data sets throughout the troposphere and stratosphere.

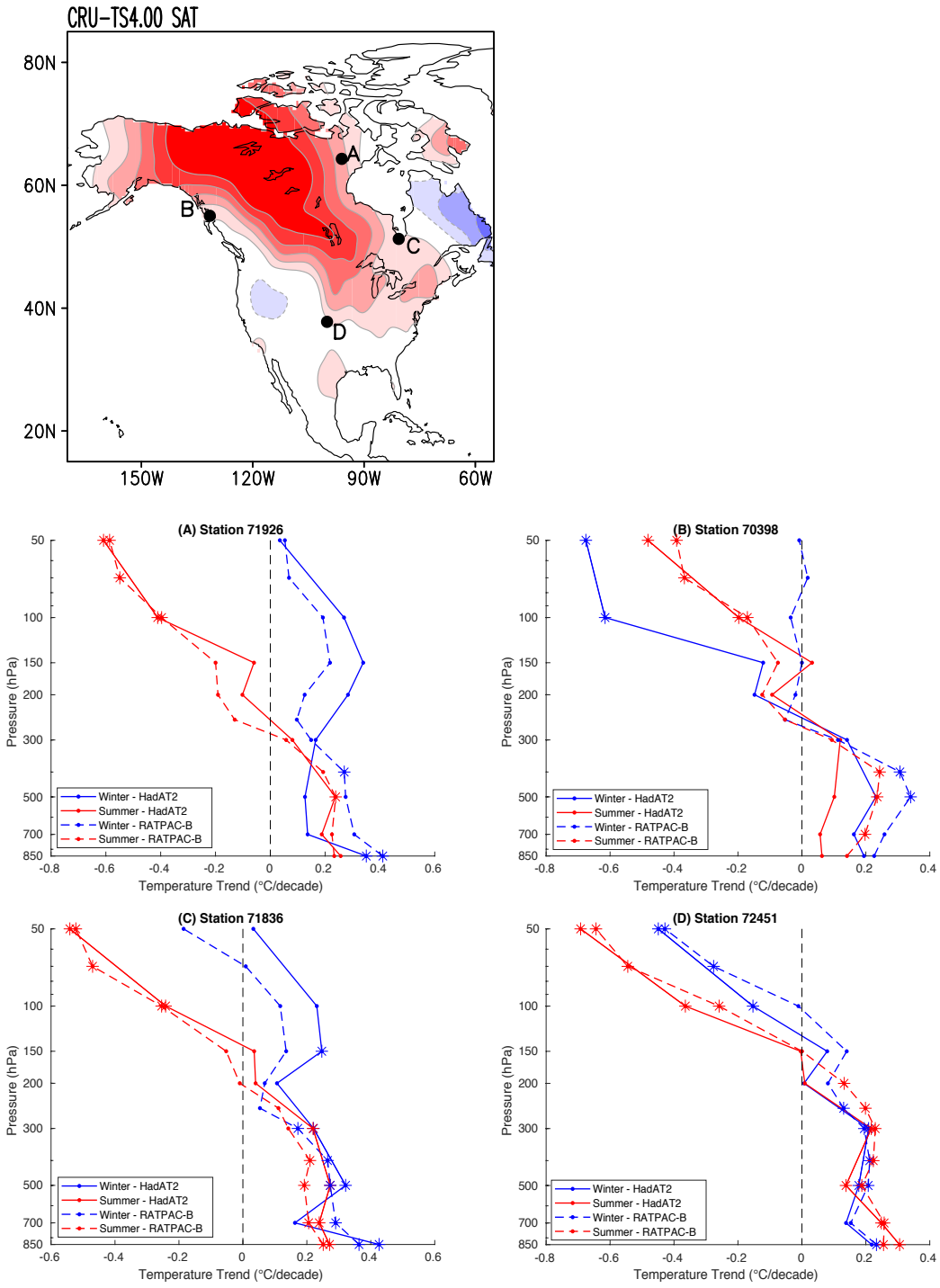


**Figure 3.2** Winter (blue) and summer (red) temperature trends over 1960-2012 for HadAT2 (solid lines) and RATPAC-B (dashed lines) at the four stations shown in the map: Baker Lake (A; WMO#71926), Annette Island (B; WMO#70398), Moosonee (C; WMO#71836), and Dodge City (D; WMO#72451). Trends significant the 95% level are denoted by star symbols.

### 3.4.2 Focus on HadAT2

The investigation of upper-air temperature trends now focuses on the analysis of radiosonde soundings from HadAT2. Five HadAT2 stations located within the region of interest are marked with black dots in Figure 3.1. The vertical profile of the seasonal temperature trends from each of these five stations is shown in Figure 3.3 for the 1958-2012 period. All stations show a similar structure of seasonal warming: notably stronger winter trends at the surface and through the troposphere, and pronounced spring and summer cooling in the stratosphere.

The vertical profile of seasonal temperature trends averaged over the five stations is plotted in Figure 3.4 for the same period. The trend at the surface is positive in all four seasons, with the winter-summer difference of ~0.4°C decade$^{-1}$ consistent with the estimate from the independent CRU-TS4.00 analysis (Figure 3.1). Winter trends are greater than summer ones throughout the entire atmosphere; they are closest at 300hPa, near the tropopause, where all seasonal trends are within 0.1°C decade$^{-1}$ of each other.

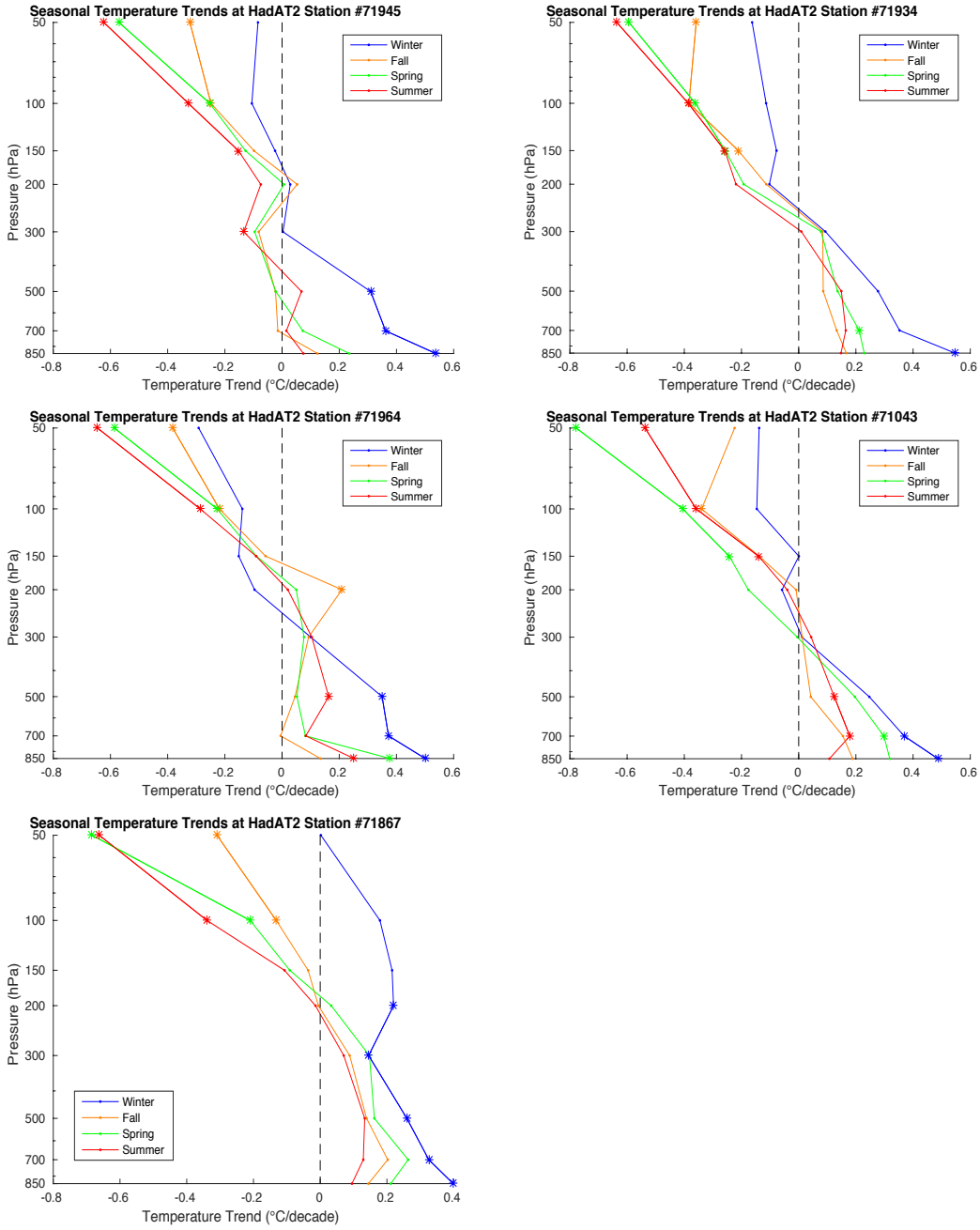


**Figure 3.3** The linear trend in seasonal temperatures (°C decade$^{-1}$) at each of the individual HadAT2 stations; station locations are marked by black dots in Figure 3.1. Trends are for the time period 1958-2012. Trends significant at the 95% level are indicated with star symbols.

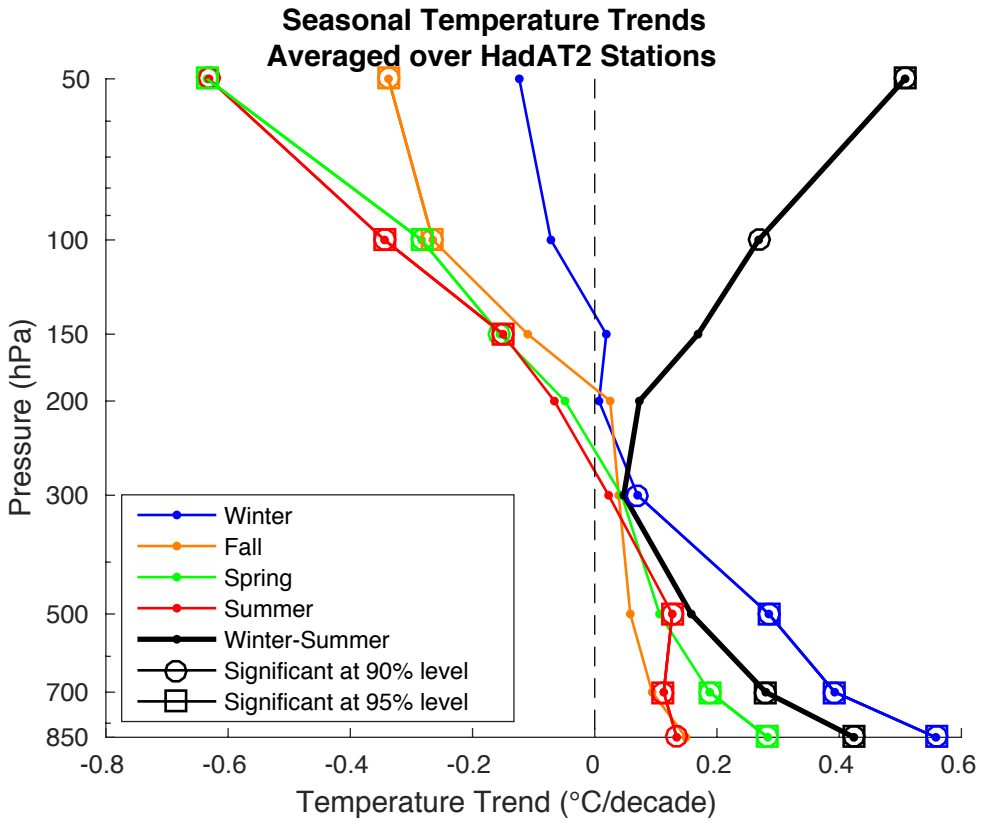


**Figure 3.4** The linear trend in seasonal temperatures (°C decade$^{-1}$) at various vertical levels in the troposphere and lower stratosphere, averaged over the five HadAT2 stations; station locations are marked by black dots in Figure 3.1. Trends are for the time period 1958-2012. Trends (and trend differences, in the case of winter-summer, black line) significant at the 90% (95%) confidence level are indicated with open circle (square) symbols.

In the stratosphere, trends become negative and the seasonality resumes, with strong cooling in all seasons except for winter. Note that displayed summer trends are not significant in the mid-troposphere (200hPa and 300hPa) and winter trends are only significant at altitude levels below 200hPa. The difference between winter and summer trends (black line, Figure 3.4) is statistically significant at the 95% level only at 850hPa, 700hPa and 50hPa. Thus, while the winter trend is greater than the summer one throughout the entire atmosphere, the difference is only statistically significant near the surface and in the stratosphere.

To further investigate the origin of these seasonal trends, Figure 3.5 shows time series of winter and summer temperatures averaged over the five HadAT2 stations at four vertical levels: mid-stratosphere (Figure 3.4a), near-tropopause (Figure 3.5b), mid-troposphere (Figure 3.5c), and near-surface (Figure 3.5d). Winter temperatures are consistently characterized by greater natural variability than summer temperatures, as noted before (Stine et al., 2009). As was seen in Figure 3.4, winter temperature trends are positive throughout the troposphere (Figure 3.5b-d) and weakly negative in the stratosphere (Figure 3.5a). Summer trends are weakly positive throughout the troposphere (Figure 3.5b-d) and strongly negative in the stratosphere (Figure 3.5a).

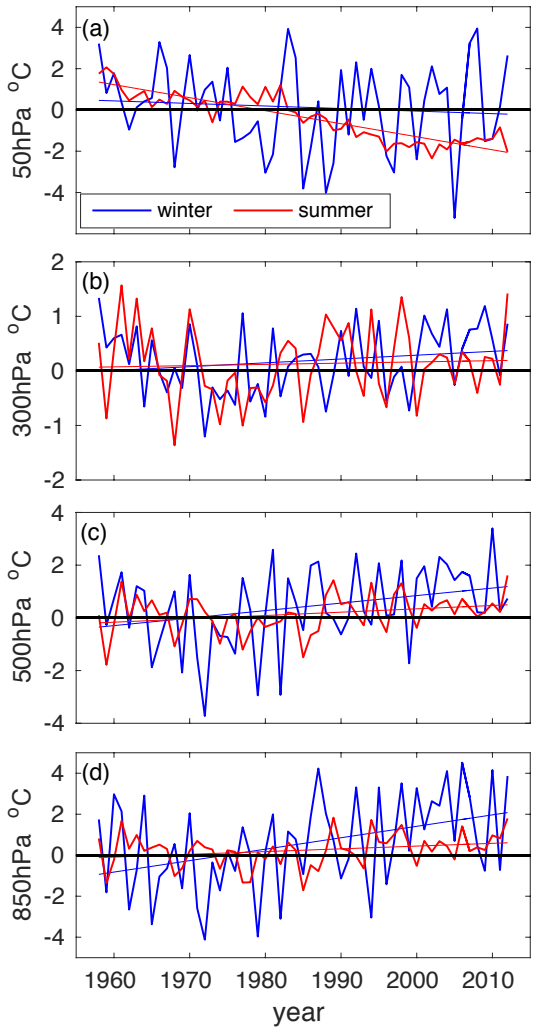


**Figure 3.5** Time series of winter (blue) and summer (red) temperature anomalies (°C) over 1958-2012 for various vertical levels (marked on the left) averaged over the five HadAT2 stations marked in Figure 3.1. Thin straight lines indicate the linear fits to the time series.

The stratospheric temperature trends observed in this region (Figures 3.4 and 3.5) align with previous work. The relatively weak cooling in stratospheric winter temperature trends is consistent with previous work on high-latitude stratospheric temperature trends (Bohlinger et al. 2014; Ivy et al. 2016; Thompson and Solomon 2005). Prior studies have found changes in the strength of the Brewer-Dobson circulation (BDC) to be a primary cause of the weak warming in stratospheric winter

trends. The annual-mean BDC is shown to have strengthened over recent decades (Fu et al. 2015) as a result of greenhouse-gas-induced warming of the tropical troposphere and subsequent increases in meridional temperature gradient, westerly zonal winds, and wave driving in the tropical lower stratosphere (Eichelberger and Hartmann 2005; Garcia and Randel 2008). In the Northern Hemisphere, the strengthening of the BDC is most pronounced in winter but there is a slight weakening trend in spring (Fu et al. 2010; Li et al. 2008; McLandress and Shepherd 2009). The intensified winter BDC leads to increased downwelling in high latitudes, and hence reduced stratospheric cooling.

Radiative effects due to ozone variations have also been shown to influence stratospheric temperatures. The seasonal cycle of ozone is fairly muted in the Northern Hemisphere polar regions (compared to the Southern Hemisphere polar regions) but with slightly higher values in late winter/early spring (Hassler et al. 2013). Ozone depletion, the long-term decline in ozone concentration, leads to cooling in the stratosphere. The depletion is attributable to the same halogen chemistry mechanisms in polar regions of both hemispheres, although the warmer Arctic and the larger influence of dynamics in the Northern Hemisphere prevent losses of the same magnitude (Solomon et al. 2014).

The analysis is complicated by the link between the dynamic and radiative processes controlling stratospheric temperatures: the increased downwelling over the Arctic due to a strengthening BDC also leads to greater ozone transport into the high latitudes, and hence radiative heating (Bednarz et al. 2016). Figure 3.4 indicates that in this particular region in northwestern Canada, the dynamic warming associated

with the strengthened BDC is the main control on the stratospheric winter temperature trends, while summer and fall experience strong enough radiative cooling from ozone depletion to compensate for any dynamically-induced warming. In spring, the weakening BDC (Fu et al. 2010) and the peak in ozone depletion (Ivy et al. 2016) combine to generate the strong cooling trends. These results are consistent with previous findings (Bohlinger et al. 2014; Ivy et al. 2016).

Given that the causes of seasonal stratospheric trends in this region agree with explanations advanced in previous work for high-latitude stratospheric trends, the remainder of this chapter will focus on tropospheric trends, and seasonal variations in them.

## 3.5 Assessment of vertical trends in NCEP reanalysis

### 3.5.1 Vertical Profiles

Although comparison of the surface/925-hPa temperature trends in Figure 3.1 is encouraging, additional affirmation for the viability of NCEP Reanalysis for characterization of upper-air trends is sought in this section. NCEP Reanalysis is interpolated to the five HadAT2 station locations, and the winter, summer, and winter-minus-summer temperature trends, averaged over these locations, are plotted from the interpolated NCEP Reanalysis and HadAT2 soundings in Figure 3.6. For additional comparison, the profiles are also plotted from the IUK data. Note that trends shown in this figure are for 1960-2012, due to the IUK data being unavailable prior to 1960. Furthermore, the IUK dataset does not have data at station 71043 (station #2 in Figure 3.1), so the trends shown here for this data set are from the average of the other four stations.

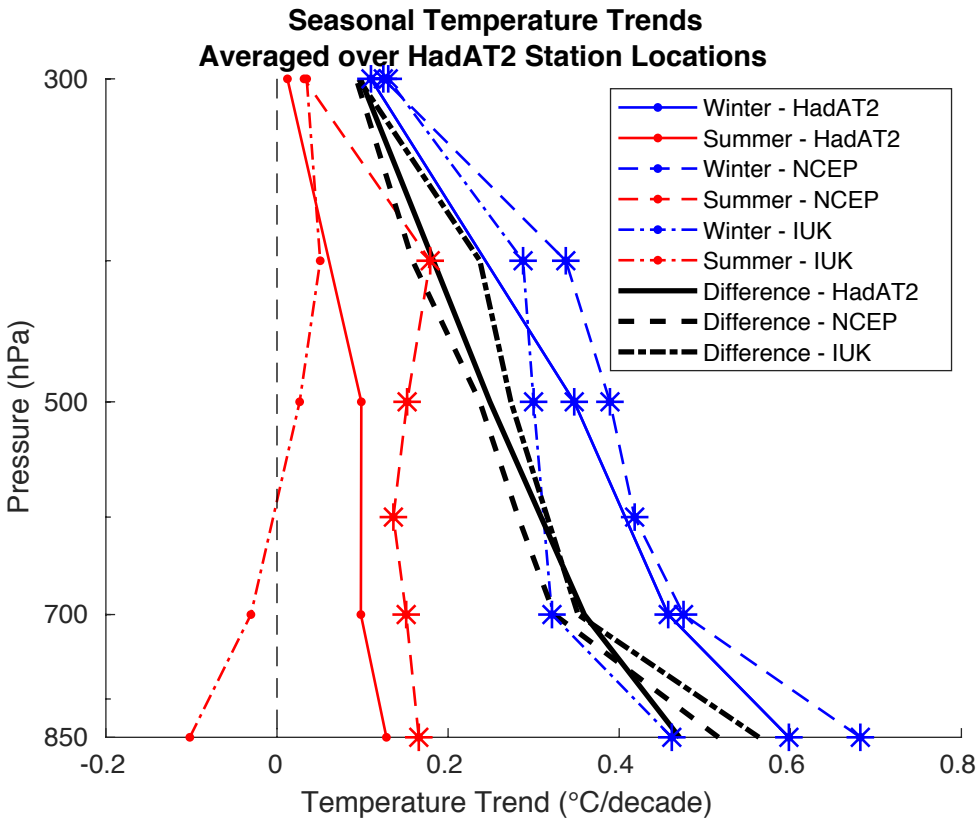


**Figure 3.6** Winter (blue lines), summer (red lines), and winter-minus-summer (black lines) temperature trends (°C decade$^{-1}$) averaged over the five HadAT2 stations for the 1960-2012 period; station locations are marked by black dots in Figure 3.1. The solid lines are from HadAT2 data, the dashed lines are from NCEP Reanalysis interpolated to the station locations, and the dotted-dashed lines are from the IUK data set. Trends significant at the 95% confidence level are indicated with star symbols.

The vertical structures of the winter and summer trends are very similar except for slight overestimation by NCEP in both seasons at all levels. Importantly, the HadAT2, IUK, and NCEP reanalysis show remarkable agreement in their vertical profile of winter-summer temperature *difference* (black lines), reflecting a reasonable assimilation of the radiosonde profiles.

### 3.5.2 Spatial distribution

Given this confidence in the ability of the NCEP reanalysis to produce realistic seasonal temperature trends at the surface and through the troposphere, it is used to examine the spatial pattern of trends throughout the atmosphere. For further comparison, the RAOBCORE-v1.5 radiosonde temperature data set is also used to examine spatial patterns. The spatial pattern of the winter-minus-summer difference in temperature trends over the entire North American continent are displayed in Figure 3.7 at various vertical levels in the troposphere from both RAOBCORE (left) and NCEP Reanalysis (right). The two show very similar structure of temperature trend seasonality at all levels, except for 300hPa where NCEP shows negative seasonality in the southeastern United States while RAOBCORE shows positive seasonality. The bottom panel shows the 850-hPa temperature trend seasonality, which displays a similar spatial structure to that of 925-hPa (Figure 3.1b). Moving through the mid-troposphere, the maximum in seasonality persists over northern Canada, although the winter-summer trend difference weakens dramatically across the continent. At 300-hPa (tropopause), the seasonality is weak over the entire continent, including northern Canada, consistent with Figure 3.4.

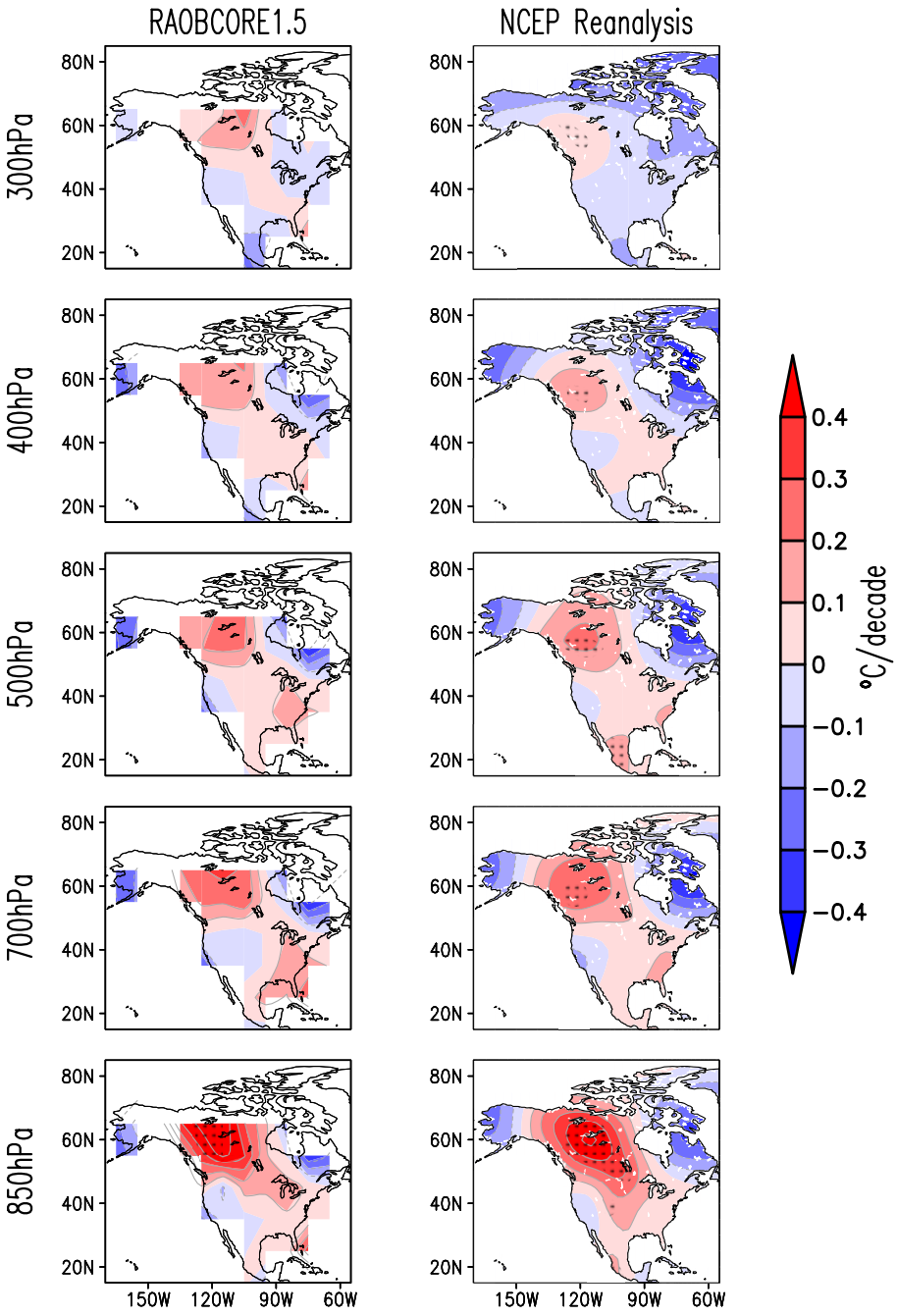


**Figure 3.7** *Winter-minus-Summer* trends in temperature (°C decade$^{-1}$) over the period 1958-2012 from the 10° resolution RAOBCORE-v1.5 adjusted temperature anomaly (left) and the 2.5° resolution NCEP Reanalysis (right). Contour and shading interval is 0.1°C decade$^{-1}$. Trend differences are shown at the 300-hPa (top), 400-hPa (second from top), 500-hPa (middle), 700-hPa (second from bottom), and 850-hPa (bottom) levels. The fields are displayed after 9 applications of the 9-point smoother (*smth9*) in GrADS. The black dots indicate trend *differences* significant at the 95% level.

As can be seen in Figure 3.4, the reduction in temperature trend seasonality when moving from the surface through the troposphere is due to weakening winter trends; summer trends do not change much with height. Previous work has attributed the relatively strong winter trends in this region to circulation changes (Wallace et al. 2012). Figure 3.8 shows the trends in 850-hPa geopotential height from NCEP reanalysis, with the HadAT2 station locations indicated by red dots. It can be seen that in winter, the circulation trends over 1958-2012 lead to the onshore advection of warmer marine air in northwestern Canada, enhancing winter temperatures in this region. As expected, circulation trends are much weaker in summer. Thus, the winter-minus-summer trends in circulation (Figure 3.8c) lead to strong positive seasonality in the region shown in Figure 3.7. Although this circulation trend pattern continues through the troposphere (not shown), the effect of the land-sea contrast is reduced with height. Thus, the dynamically strengthened winter temperature trends reduce with height in the troposphere.

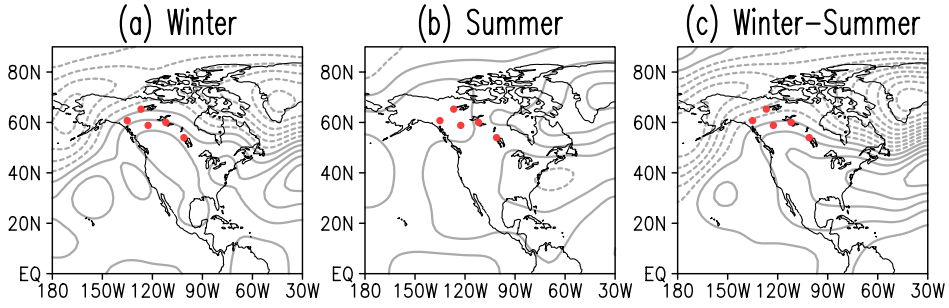


**Figure 3.8** Winter (left), summer (middle) and winter-minus-summer (right) trends in 850hPa geopotential height (m decade$^{-1}$) over the period 1958-2012 from NCEP Reanalysis. Contour interval is 1m decade$^{-1}$. Red dots indicate the locations of the HadAT2 stations analyzed in this study. The fields are displayed after 9 applications of the 9-point smoother (*smth9)* in GrADS

## 3.6 Discussion

The analysis is a continuation of the topics addressed in Chapter 2 – here the goal was to expand the characterization of the secular change signal in the temperature field, notably its seasonality, which is large at the surface of the Northern Continents. The seasonal analysis of upper-air temperature trends has not previously been done for this region, and it provides an opportunity for the further investigation of mechanisms underlying the different seasonal responses.

The reported analysis is different from Chapter 2 in its focus on upper-air temperature trends. Troposphere and lower stratosphere trends over northwestern North America – a focal point of the notable seasonality in surface air temperature trends (Nigam et al. 2017) – are analyzed from radiosonde soundings and atmospheric reanalysis. A key motivation for this analysis was the assessment of the viability of the hypotheses that have been previously advanced for the seasonality in surface temperature trends (Nigam et al. 2017; Stine et al. 2009; Wallace et al. 2012).

In the region of largest winter-summer difference in *surface* temperature trends (northern Canada), it is shown that:

- The seasonality in trends diminishes with altitude, becoming a minimum at the tropopause, and increasing again in the stratosphere. The difference between winter and summer temperature trends is statistically significant in the lower troposphere and stratosphere.
- Although cooling trends are found in all seasons in the stratosphere, the winter trends are warmer than those in other seasons (which closely track each other), consistent with the findings of Ivy et al. (2016). The seasonality in

stratospheric temperature trends is well documented and their origin discussed in the literature. Both radiative cooling from ozone depletion and dynamic changes in the strength of the Brewer Dobson circulation have been implicated (Fu et al. 2010; Ivy et al. 2016), with unique levels of contribution from each in the different seasons.

- At the surface, the strong seasonality is consistent with both thermodynamic reduction of summer trends (the land surface-hydroclimate interaction hypothesis of Nigam et al. (2017)) and the dynamic strengthening of winter trends due to changes in circulation. The vertical structure of seasonal temperature trends throughout the troposphere offers support for both of these mechanisms. The winter trends are gradually reduced when moving away from the surface, indicating a smaller role for circulation-induced thermal advection when moving away from the strong land-sea contrast at the surface. The summer trends are less variable in the lower troposphere, remaining close to 0.1 °C decade$^{-1}$ until 500-hPa.

Natural variability can also contribute to these trends, and the separating of natural from forced variability in these 55-year trends would be worthwhile. The possibility of multidecadal natural variability getting aliased into linear trends is considered in the context of surface air temperature trends in Chapter 2 (see section 2.4.3 and 2.4.4). Interestingly, however, the 55-year linear trends documented here exhibit a winter-summer seasonality at the surface that is similar to that present in the century-long trends in that study. Further elucidation of the mechanisms generating the seasonality in surface and upper-air temperature trends will require

comprehensive analysis of the surface energy balance and the regional atmospheric and terrestrial water cycles.

# Chapter 4: Seasonal hydroclimate trends over Africa[3]

## 4.1 Background

Climate change has footprints across the planet; however, certain regions are disproportionately affected. Africa is less responsible for the occurrence of anthropogenic climate change than any other continent (Fields 2005) but more vulnerable to its effects on account of its high population, low adaptive capacity, and multiple converging stressors (Busby et al. 2014; Fields 2005; Niang et al. 2014). Africa is furthermore an interesting case study for climate change due to its unique climatological features. It is the only continent that has almost equal parts in the Southern and Northern Hemispheres (Collins 2011) and thus is home to a wide variety of climate zones. It consists of the Sahara Desert and Sahel in northern Africa, the Namib-Kalahari Desert in southern Africa, tropical rain forest in equatorial Africa, and grasslands and savanna in between. The prevalence of land surface effects, internal climate variability, and sensitivity to global sea surface temperatures make the continent climatically complicated (Hulme et al. 2001).

Several studies have investigated the trends in precipitation and surface air temperature over the continent. Precipitation variability occurs on a range of climate time scales; low-frequency variability, characteristic of West Africa and the Sahel, is associated with multidecadal changes in sea surface temperature (SST) and

[3] Most of this chapter is published as Thomas and Nigam (2018), with the exception of some additional supporting details and slight re-organization for clarity.

atmospheric circulation (Nicholson 2001; Nigam and Ruiz-Barradas 2016; Zhang and Delworth 2006) whereas higher-frequency variability, seen in eastern and southern Africa (Nicholson and Kim 1997; Schreck and Semazzi 2004) is connected to El Nino-Southern Oscillation (ENSO) and other subdecadal processes (Hulme et al. 2001; Nicholson 2001; Omondi et al. 2013).

Precipitation trends have been particularly well studied over the Sahel region. Rainfall in the Sahel is linked strongly to the West African Monsoon (Thorncroft et al. 2011), which drives the annual cycle in precipitation. The drying trends in the Sahel have been related to land surface processes, including amplification of meteorological drought from biophysical (Charney 1975) and surface hydrologic feedbacks (Nicholson 2000). Regional and global patterns of SST anomalies have also been implicated (Folland et al. 1986; Giannini et al. 2003) as have sulfate aerosols in the Northern Hemisphere through their effect on Atlantic SSTs (Biasutti and Giannini 2006). The 1980s Sahel drought – the most intense episode of the twentieth century – has been attributed to the circulation change associated with Indian Ocean warming (Hagos and Cook 2008), and the drought recovery linked to higher levels of greenhouse gases in the atmosphere (Dong and Sutton 2015). Sahel rainfall has also been linked to AMO variability (Knight et al. 2006; Martin and Thorncroft 2014; Mohino et al. 2011; Nigam and Ruiz-Barradas 2016; Nigam et al. 2011; Zhang and Delworth 2006), with the cold AMO phase coincident with extended droughts over the Sahel. The mechanisms of this connection have been attributed to the impact of AMO on the West African monsoon annual cycle (Martin and Thorncroft 2014).

Causes of surface temperature variability are less well established (Collins 2011), although an amplified warming signal has been detected over the Sahara Desert in recent decades (Cook and Vizy 2015; Vizy and Cook 2017; Zhou 2016).

The importance of agriculture in the African economies warrants a seasonally resolved analysis of hydroclimate variability and change over the African continent. Here, the analysis is on African hydroclimate as represented by temperature and precipitation. The seasonality of trends in temperature and precipitation over Africa has been briefly examined in earlier studies. Temperature trends over the continent as a whole were found to be greater in summer and fall than in winter and spring (Collins 2011; Hulme et al. 2001), with significant winter warming in northern tropical Africa and significant summer warming across the continent, and specifically the Sahara (Collins 2011). Documented precipitation trends, other than over the Sahel, include the decreasing spring rainfall trend over East Africa (Maidment et al. 2015; Rowell et al. 2015; Williams and Funk 2011) and continental-scale seasonal precipitation trends (Hoerling et al. 2006); the latter have been plotted but not extensively discussed. The need to analyzing seasonal rainfall in tropical regions has been noted (Feng et al. 2013).

Global climate change often leads to the wet regions getting wetter and the dry ones drier (Chou et al. 2013), suggesting adverse impacts on deserts. The impact on the Sahara is of great importance for the proximal countries in northern Africa as well as for remote regions through the influence of Saharan dust on SSTs and Atlantic hurricane activity (Evan et al. 2016). Previous studies have estimated the size of the annual-mean Sahara Desert using a vegetation index (Tucker and Nicholson 1999;

Tucker et al. 1991) but only over the recent satellite-era periods ranging from 10 to 17 years. The century-long seasonal trends in the expanse and extent of the Sahara Desert, whose structure and mechanisms concern this study, have hitherto remained undocumented. A seasonally stratified perspective is at some variance with the classical notion of the desert (based on an annual-mean view) but is nonetheless pursued in the interest of agriculture and water resource planning. It is, of course, complemented by analyses of the annual-mean hydroclimate trends, yielding twentieth century expansion rates for the conventionally defined Sahara Desert.

## 4.2 Data and methods

This chapter focuses on centennial trends rather than multidecadal variability (a more common analysis focus) of African hydroclimate. Linear trends in temperature and precipitation are computed from least squares fitting using seasonally averaged data. To avoid confusion given Africa's expansive footprints in both hemispheres, seasons are referred using their boreal definition: winter is the average of December, January, and February (DJF), and so on. For the historical climate simulations, linear trends are computed by averaging the linear trends manifest in the ensemble members of that model.

### 4.2.1 Observational Data Sets

Three independent analysis of the observed SAT are examined: CRU-TS 4.00, Berkeley Earth and NASA-GISS. These are described in more detail in section 2.2.1.

The datasets are converted to a common 0.5° resolution using bilinear spatial interpolation. Each data set handles data interpolation and infilling differently.

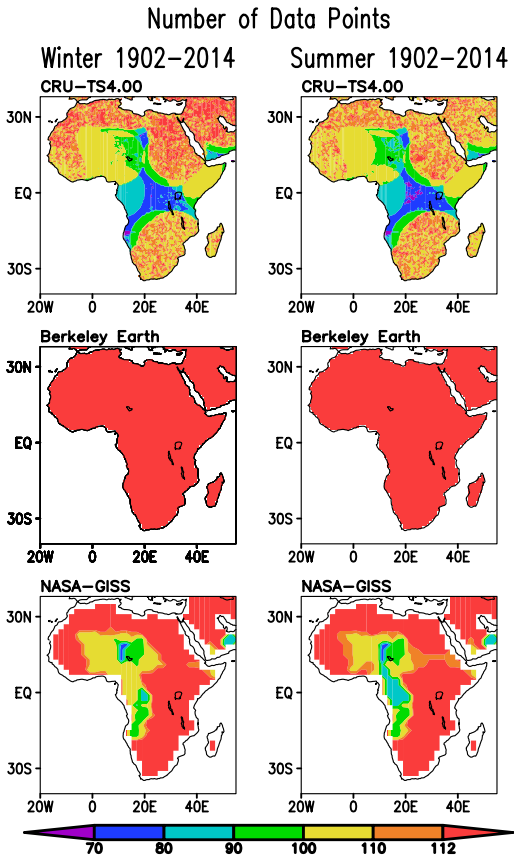


**Figure 4.1** Winter (DJF) and (center left) summer (JJA) number of data points with station data (rather than climatological in-fill) over the 113-year period (1902-2014) in three independent analyses of observed SAT: (top) the 0.5° resolution CRU TS4.00, (middle) the 1.0° resolution Berkeley Earth, and (bottom) the 2.0° resolution NASA GISS.

The Berkeley Earth analysis uses a kriging procedure for interpolation (Rohde et al. 2013), so the amount of infilling is not possible to ascertain. For the CRU TS 4.00 and NASA GISS, grid points with no station data are filled with the climatology (1961-1990 for CRU TS and 1951-1980 for NASA GISS). Thus, while data are not reported as "missing" in the analyses, it is possible to estimate how many time steps

in the 113-year record are filled in with the climatology. This is shown for each SAT analysis for both winter and summer in Figure 4.1. Both the CRU TS 4.00 and NASA-GISS have climatological infilling in western Saharan Africa. The CRU TS 4.00 data set also has areas of infilling in equatorial Africa.

The GPCC product is again used for precipitation analysis (see section 2.2.2). Sahel rainfall is defined as the area-averaged rainfall within 20°W-40°E and 10°N-20°N, following Held et al (2006). To assess spatial coverage of this data set over time, Figure 4.2 shows the station coverage of the GPCC v7 data set in July of 1902, 1920, 1986 and 2013. The number of stations used in GPCC's monthly precipitation analysis peaks in 1986 (Schneider et al. 2014; their Figure 2).

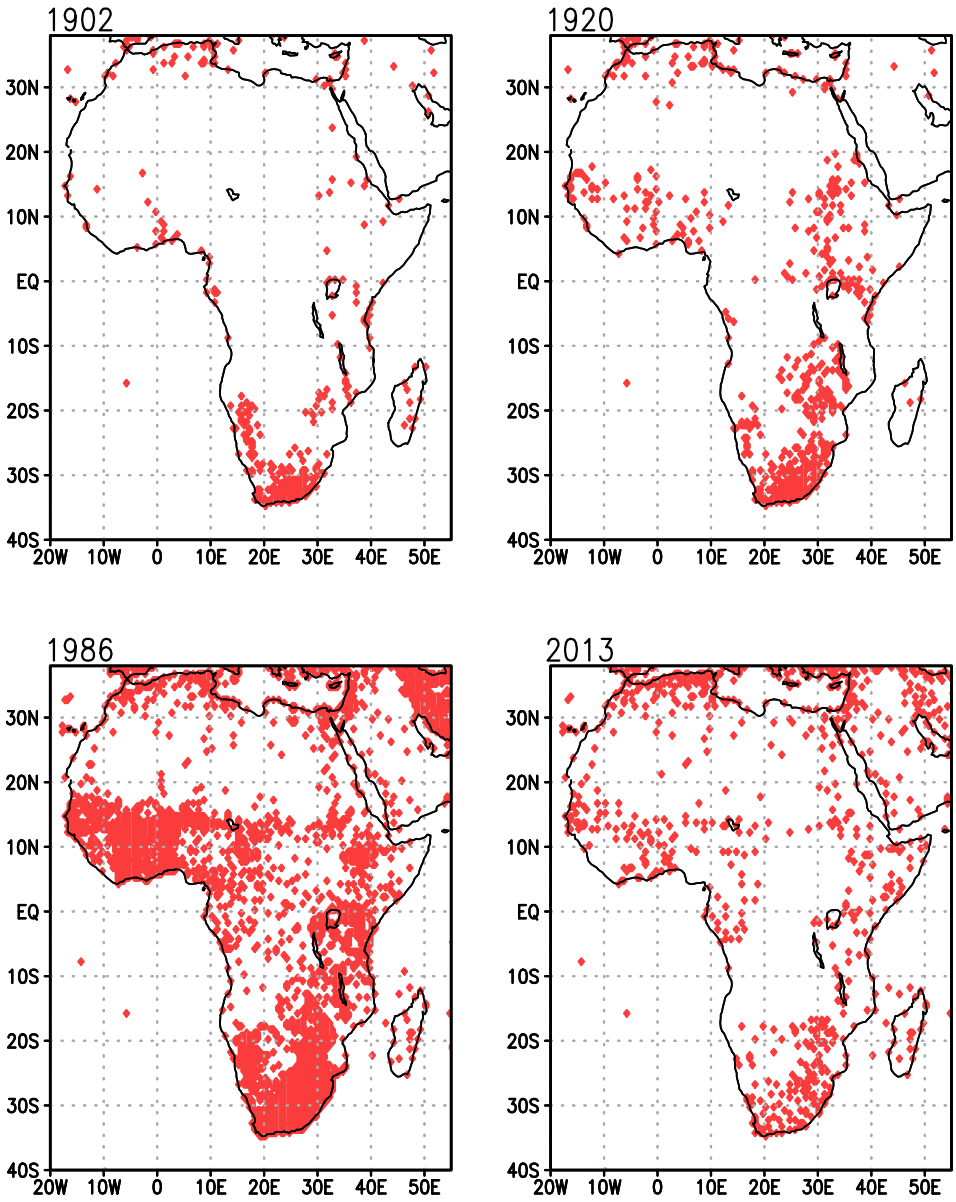


**Figure 4.2** Spatial distribution of station observations used in the GPCC analysis for the month of July for 1902 (top left), 1920 (top right), bottom left (1986) and bottom right (2013).

For comparison, the precipitation analysis from the University of Delaware (Willmott and Matsuura 2015) is also briefly examined.

The NCEP-NCAR reanalysis (Kalnay et al. 1996) is used for calculating the core latitude of the subtropical tropospheric jet in northern winter, following the method of Archer and Caldeira (2008) with integration over the latitude band 15°N-

45°N. Figure 4.3 shows the time series of the latitude of the NH jet averaged over 30W-60E using this method. For comparison, Figure 4.3 also shows the jet latitude computed using two other reanalyses: ERA40 (Uppala et al. 2005) and NOAA 20CR (Compo et al. 2011). All show a similar representation of jet latitude; over 1958-2001, NCEP/NCAR and ERA40 have a correlation of 0.99 and over 1949-2011, NCEP/NCAR and NOAA20CR have a correlation of 0.93.

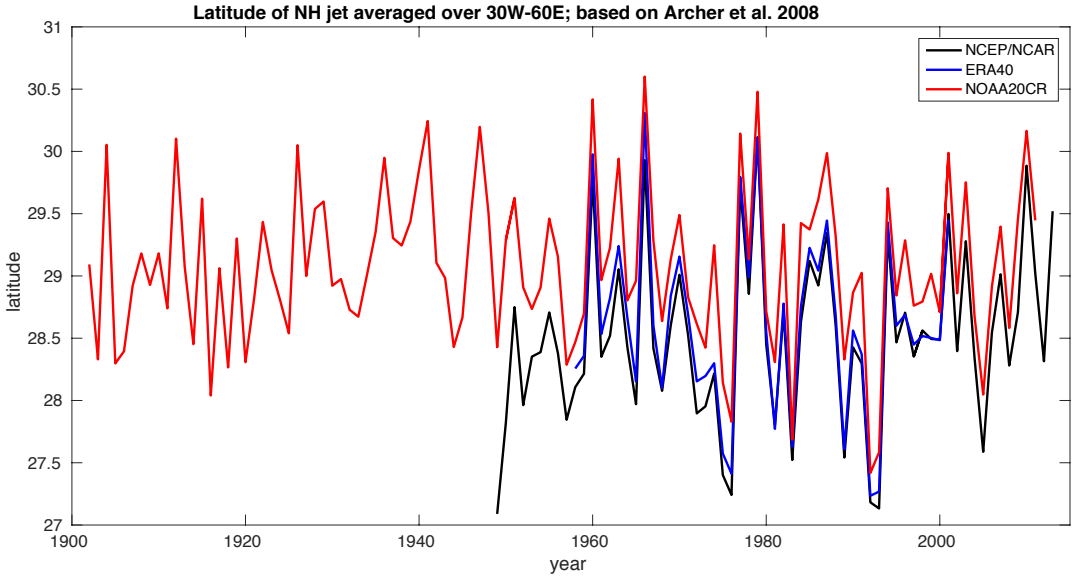


**Figure 4.3** Latitude of the subtropical tropospheric jet in northern winter averaged over 30W-60E, computed using the method of Archer and Caldeira (2008). This method involves integration of winds; this calculation is done using winds from three different reanalysis products over three different periods: the NCEP/NCAR (black line; 1949-2013), ERA40 (blue line; 1958-2001) and NOAA20CR (red line; 1902-2011).

Several climate indices are used in this chapter. The AMO (Enfield et al. 2001; Kavvada et al. 2013) index was computed as the linearly detrended seasonal SST anomaly over the North Atlantic (0°-60°N, 5°-75°W), following (Enfield et al. 2001); SST from the HadISSTv1.1 analysis (Rayner et al. 2003) was used. An additional marker of AMO variability was the principal component extracted from an

extended empirical orthogonal function (Weare and Nasstrom 1982) analysis of HadISSTv1.1 SST data (Guan and Nigam 2009). The PDO index was obtained from http://jisao.washington.edu/data/pdo/ where it is defined as the leading principal component of monthly SST anomalies in the North Pacific (poleward of 20°N) (Zhang et al. 1997).

Stream flow data for the Niger River were obtained from NCAR's monthly flow rate archive (https://rda.ucar.edu/datasets/ds552.1) (Dai and Trenberth 2003). Station 9142 (Koulikoro; 12.887°N, 7.54°W) was used as it has the longest record among stations in the source region of the Niger River. The record extends from January 1902 to December 1990.

#### 4.2.2 Historical climate simulations

In this study, five models contributing to the IPCC AR5, and all of their ensemble members, are analyzed. See Table 1.1 for model details.

#### 4.2.3 Desert expansion

Two methods are used to quantify desert expansion during the 1902-2013 period. In both methods, a precipitation threshold is chosen to define the desert boundary; three threshold values – 100 mm $year^{-1}$ (or 0.274 mm $day^{-1}$), 150 mm $year^{-1}$ (or 0.411 mm $day^{-1}$) and 200 mm $year^{-1}$ (or 0.548 mm $day^{-1}$) – based on previous definitions of the annual-mean Sahara boundary (Breman and Dewit 1983; Tucker and Nicholson 1999) are used. The first two thresholds were considered so that sensitivity of the desert-area trend to the desert definition could be assessed; the third threshold is used only to enable comparison with Tucker and Nicholson (1999), who used a vegetation index to assess the size of the Sahara Desert over the satellite era.

Desert area is computed by taking an area sum after weighting each grid-cell area by the cosine of its latitude; the Grid Analysis and Display System (GrADS) function 'asum' was used. In the first method, referred to as the area-trend method, the desert area is computed each year in each of the four seasons and annually, with average rainfall less than the threshold defining deserts. The 1902–2013 linear trend in the computed area characterizes desert expansion/contraction over the twentieth century.

In the second method, referred to as the endpoint method, the precipitation climatology ($P_{clim}$) and the linear trend in precipitation ($Pt_{rend}$) over the 112-yr record are first computed at each grid point, seasonally and annually. These are used to create two maps, showing precipitation at the end (from the plus sign in the following expression) and at the beginning (from the minus sign) of the record:

$$P = P_{clim} \pm (P_{trend}) \times 56 years$$

The desert extent is then mapped in these synthetic 1902 and 2013 precipitation distributions at the endpoints of the record based on the chosen threshold, with the difference yielding desert expansion over the time period.

In both methods, the desert area computation is restricted to North Africa (northward of 58°N) to preclude inclusion of the Namib–Kalahari Desert, and to the west of 43°E to avoid inclusion of the Horn of Africa.

Each method has its advantages: The area-trend method is conceptually simple, but it does not reveal the desert advance and retreat regions. The endpoint method is slightly more complex but it easily outlines the desert advance/retreat regions. Both methods should yield similar results except, perhaps, when the analysis period is comparable to the embedded variability time scales—a condition met with

the AMO, especially when it is influential on regional hydroclimate. The aliasing of multidecadal variability into linear trends would be inevitable in this case but with the two methods having different exposure to aliasing from the inverted order of the area-computation and linear-trend operations. For both methods, the estimate of the size of the desert using a precipitation-based threshold is limited by the spatial resolution of the precipitation data set (0.5°). Increasing the resolution of this precipitation data set would increase the accuracy of the area of the desert.

The seasonal northern edge of the Sahara Desert was computed each year as follows: For each desert longitude (20°W–35°E), the nearest latitude north of 20°N where the seasonal precipitation threshold was met was determined. The latitudes were then averaged to obtain the northern edge of the Sahara Desert.

#### 4.2.3 Statistical significance

Statistical significance of individual linear trends at the 95% confidence level was assessed using the so-called AdjSE+AdjDF approach of Santer et al. (2000). This method employs an effective sample size based on the lag-1 autocorrelation coefficient of the regression residuals. The statistical significance of correlation coefficients was calculated using the method outlined in Ebisuzaki (1997), which is useful for time series with high serial correlation. Significance of the correlation coefficients is noted in the text.

## 4.3 Seasonal climatology

The seasonal cycle of rainfall over the African continent is shown in Figure

4.2. Rainfall is larger, not surprisingly, in the summer hemisphere: over tropical West Africa, the Sahel, and Ethiopia in boreal summer (JJA) and over the Congo and Zambezi basins in austral summer (DJF). The similarity of the March–May and September–November rainfall distributions—with equatorial Africa, especially the Congo basin, being the rainfall focus—reflects the similar insolation distribution over the continent at these times from the Sun being overhead twice at the equator each year, during the vernal (late March) and autumnal (late September) equinox. The Sahara Desert is, however, drier in spring than it is in fall, and the Namib–Kalahari Desert likewise is drier in its spring than fall. The strong latitudinal gradient in precipitation at the southern boundary of the Sahara is a notable feature in all seasons, with the movement of this gradient over time having implications for regional agricultural productivity.

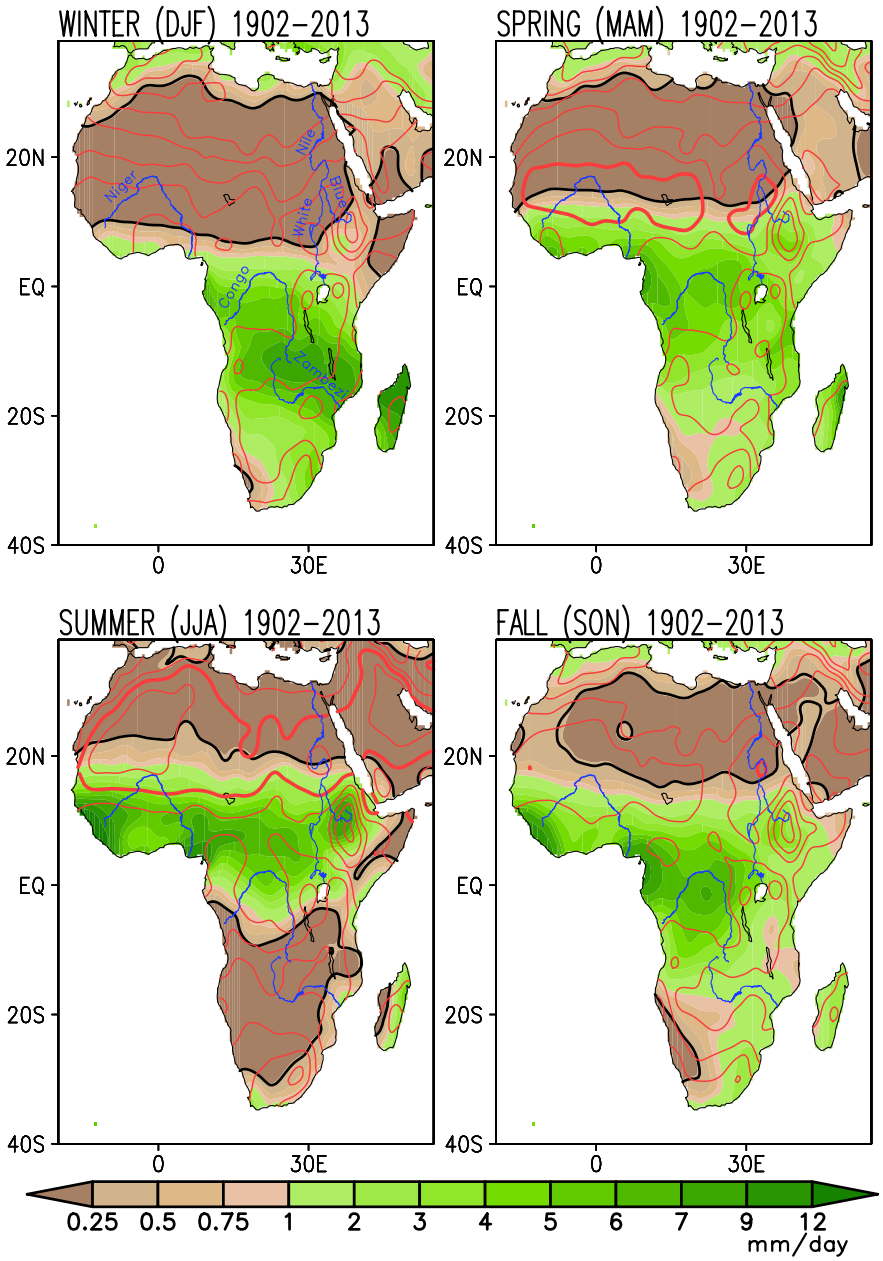


**Figure 4.4** Seasonally averaged precipitation (brown–green shading; mm day$^{-1}$) and surface air temperature (SAT; red contours; °C) for the period 1902–2013. Precipitation is from GPCC and SAT from the CRU TS4.00 dataset. Contour interval for SAT is 3.0°C. Fields are shown after nine applications of the 9-point smoother (smth9) in GrADS. Thick red contours indicate the 30°C isotherm, while thick black ones mark the 0.274mm day$^{-1}$ precipitation isoline.

The desert boundary, based on seasonally averaged rainfall threshold of 0.274 mm day$^{-1}$ (or 25 mm season$^{-1}$), is shown in thick black contours in Figure 4.4. The

Sahara expanse is largest in boreal winter and smallest in boreal fall (see Table 4.1); the larger threshold (0.411 mm $day^{-1}$ or 37.5 mm $season^{-1}$) yields the smallest expanse in summer; both analysis methods return the same seasons for maximum and minimum expanse (cf. Table 4.1). In winter, the dry region extends from ~10° to 30°N, but in summer the Sahel rainfall pushes the Sahara's southern edge closer to 20°N. Likewise, the Namib–Kalahari Desert in Southern Hemisphere Africa is most expansive in austral winter, consistent with the notion of the desert location under the descending branch of the meridionally overturning Hadley circulation; the Hadley descent is most intense in each hemisphere's winter (Nigam and Chan 2009).

The seasonal distribution of climatological SAT is also shown in Figure 4.4, using red contours. The warmest temperatures are found in boreal summer when SAT exceeds 33°C over western Saharan Africa. The coldest temperatures occur northward of the Atlas Mountains in Algeria and Morocco in boreal winter. A local minimum in SAT exists over Ethiopia in all four seasons due to the high elevation of the Ethiopian Highlands. The spring and fall distributions exhibit less similarity in SAT than in rainfall, especially over sub-Saharan Africa where SAT is notably higher in boreal spring, likely because of the preceding dry season (winter) and depleted soil moisture stores, which would preclude latent disposition of increased spring insolation.

## 4.4 Centennial trends in surface air temperature and precipitation

### 4.4.1 Seasonal SAT trends

The 1902-2014 SAT trend is obtained from the average trend in three independent analyses (CRU TS4.00, Berkeley Earth, and NASA GISS) of SAT

observations. First, the trend in each individual analysis is shown in Figure 4.5 for both winter and summer. Not surprisingly, modest differences are evident on regional scales (e.g., in the strength and location of austral winter warming over southern Africa). Likewise, boreal winter warming over Sudan has varied representation, being strong in the CRU TS4.00 analysis but not in others. Some of these differences, undoubtedly, arise from the spatiotemporal sparseness of the CRU and NASA GISS datasets (see Figure 4.1). A broader view, however, indicates consistency on the larger scales among the three trends.

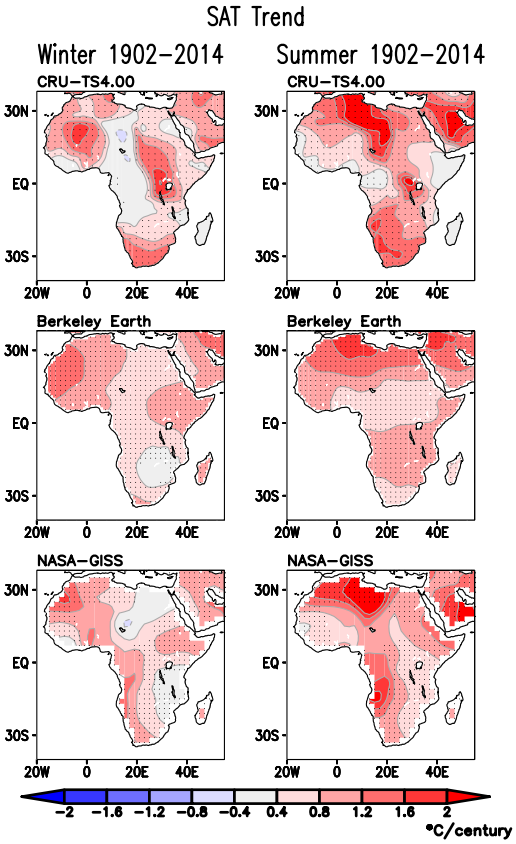


**Figure 4.5** Winter (DJF) and (center left) summer (JJA) linear trends in three independent analyses of observed SAT during 1902–2014: (top) the 0.5° resolution CRU TS4.00, (middle) the 1.0° resolution Berkeley Earth, and (bottom) the 2.0° resolution NASA GISS. Contour–shading interval and shading threshold is 0.5°C century$^{-1}$. Fields are displayed after 9, 1, and 1 application(s), respectively, of smth9 in GrADS. Trends significant at the 95% confidence level are stippled.

Figure 4.6 shows the average SAT trend from the three data sets over 1902-2014. Notable features include the following:

- Larger trends over Northern Hemisphere Africa in all seasons.
- A regional maximum over Sudan, particularly in spring when SAT trends are larger than 1.5°C century$^{-1}$; interestingly, this is the Nile River basin.
- A pronounced seasonality in trends over North Africa, near Algeria and Tunisia. Trends here range from 0.8°C century$^{-1}$ in winter to as much as 2.0°C century$^{-1}$ in summer.
- A comparatively muted seasonality in trends over Southern Hemisphere Africa except for Angola, Namibia, and Botswana where austral winter (JJA) warming is stronger than in other seasons.
- The similarity in boreal winter and fall SAT trends over much of the continent.

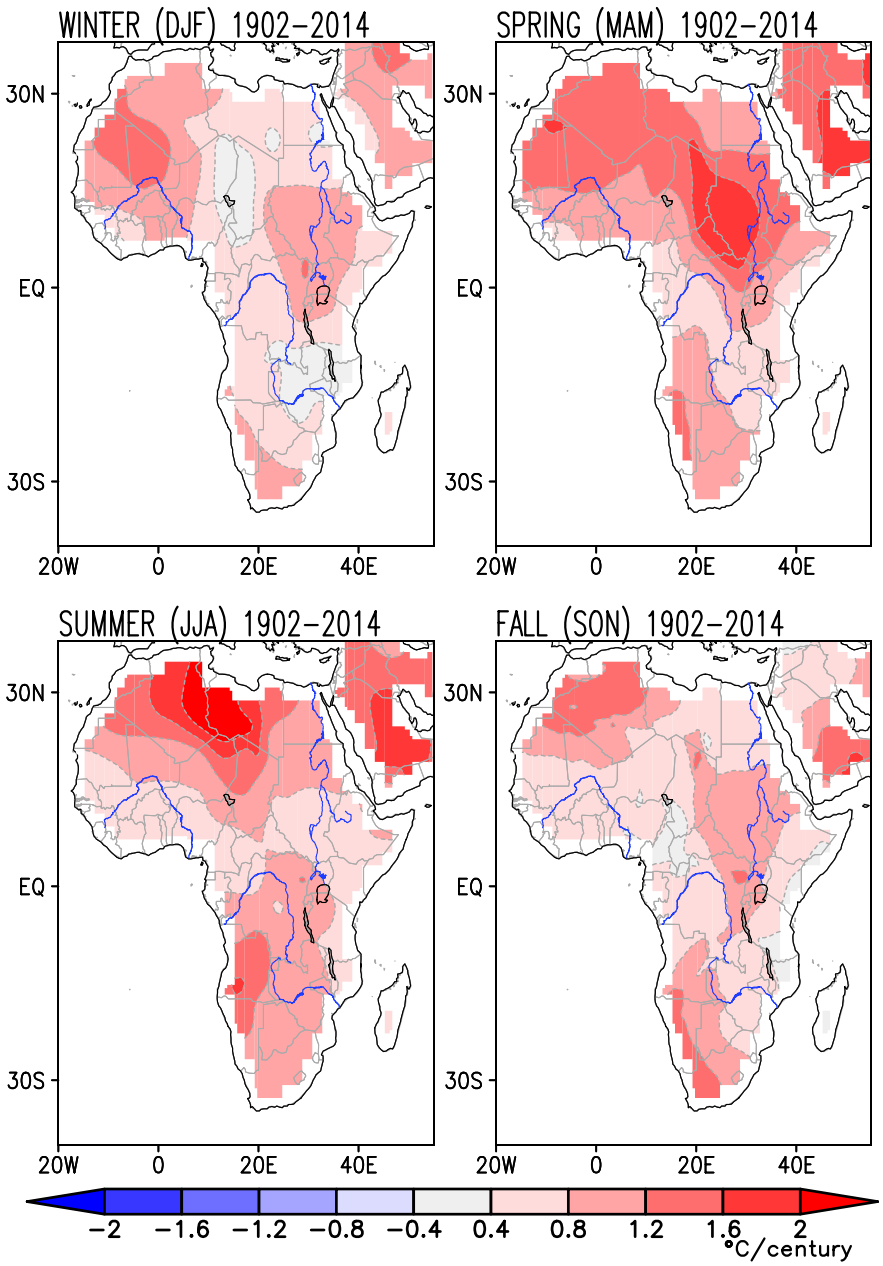


**Figure 4.6** Linear trends in near-surface air temperature over the African continent during 1902–2014. Average of the trends in three independent SAT analyses—CRU TS4.00, Berkeley Earth, and NASA GISS—is shown after each was interpolated to 0.5° resolution. Contour and shading are at 0.4°C century$^{-1}$ interval.

The seasonality of SAT trends can potentially modulate the amplitude of the seasonal cycle of SAT in the recent period. An increasing amplitude can worsen heat stress, as over central-southern Sudan (to the west of the White Nile) where

twentieth-century SAT trends are large, especially in spring when the SAT peaks climatologically as well (cf. Figure 4.4), leading to hotter springs and increased heat stress. Likewise, over northern Africa, including Algeria, Tunisia, and Libya, SAT trends are largest in summer, the season of greatest climatological SAT. In both these regions, the SAT trends amplify the seasonal cycle of regional SAT, intensifying heat extremes.

Figure 4.7 shows the seasonal trends in diurnal temperature range (DTR; the difference between daily maximum temperature, $T_{max}$, and daily minimum temperature, $T_{min}$) from CRU TS 4.00. Over the twentieth century, global surface warming has been broadly associated with larger increases in $T_{min}$ than $T_{max}$, or a decrease in DTR (Braganza et al. 2004). Changes in DTR can provide valuable information, as $T_{min}$ is largely a function of longwave radiative flux and $T_{max}$ is more closely related to shortwave radiative forcing (Lewis and Karoly 2013). DTR is strongly affected by cloud cover and soil moisture. Figure 4.7 shows that there has been a decreasing trend in DTR over Sudan, Mali and west Niger, with greater trends in $T_{min}$ than $T_{max}$ (consistent with the global-mean findings of Braganza et al. (2004)). Conversely, an increasing trend in DTR is seen over Morocco, East Niger and Chad, and Democratic Republic of the Congo. The decreasing DTR trend over Sudan is intriguing – trends in both DTR and SAT are greatest in spring (see Figure 4.6), potentially indicating a role for changes in cloud cover in affecting temperature trends in this region. Examining precipitation trends over these regions should provide more insight into this possibility; this is the focus of the next section.

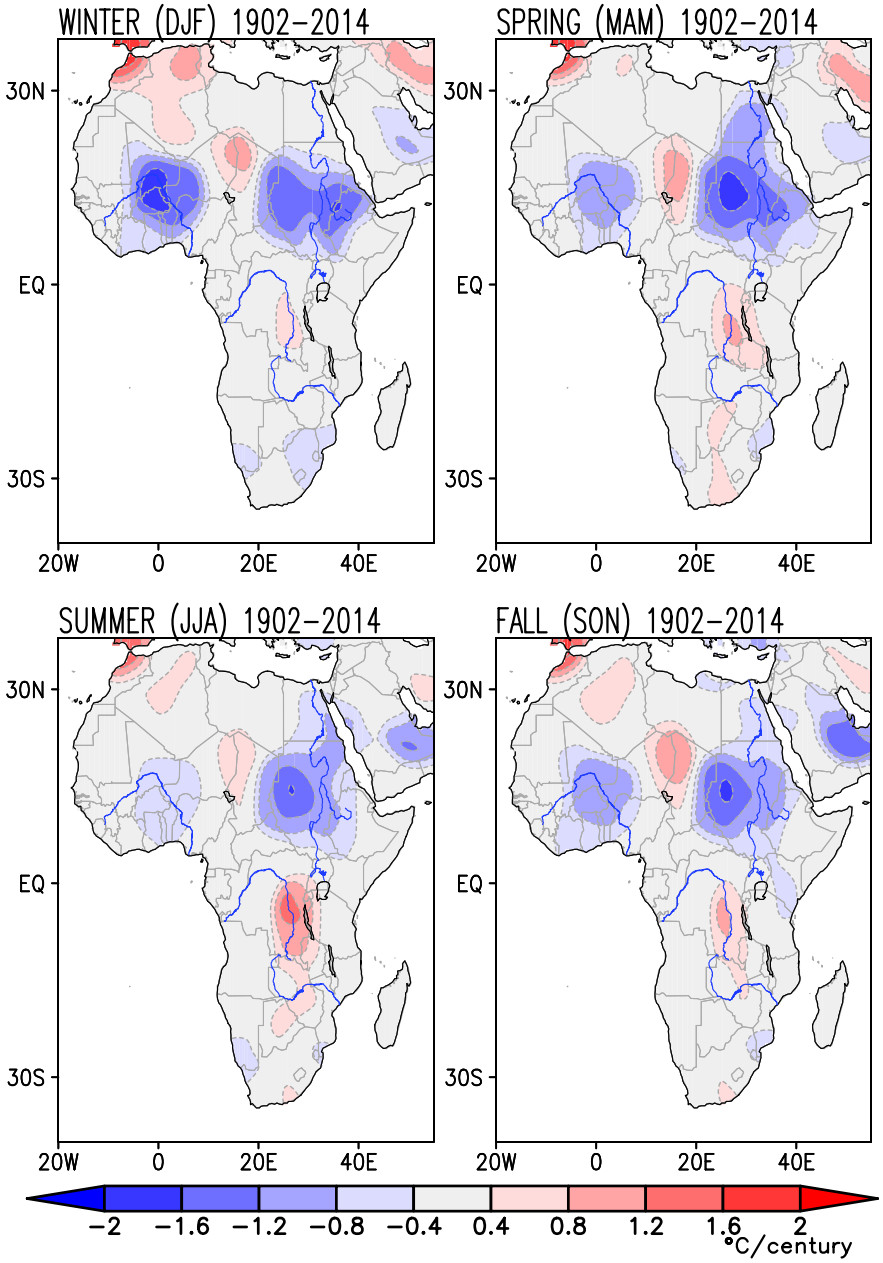


**Figure 4.7** Linear trends in seasonal diurnal temperature range (DTR; °C century$^{-1}$) over the African continent during 1902-2014, from the CRU TS 4.00 dataset. Contour and shading interval is 0.4 °C century$^{-1}$. Fields are shown after 9 applications of smth9.

### 4.4.2 Seasonal precipitation trends

The linear trend in seasonal precipitation over the twentieth century (1902–2013) is shown in Figure 4.8 against the backdrop of the climatological dry regions

(brown hatching). The centennial trends show interesting variations, corroborating the importance of seasonal analysis. For example, over Kenya and Tanzania, declining rainfall trends are present in boreal spring whereas increasing ones are present in fall and winter, each with socioeconomic implications. An annual-mean perspective, where offsetting seasonal trends average out, is not sufficient to understand the impact of climate change on a continent where the seasonal rhythm of rainfall is the pace maker.

The rainfall decline is notably intense, with no seasonal offsets, over tropical West Africa. The decline is broadly focused on the source region of the Niger River, extending across several Gulf of Guinea rim countries (Senegal, Gambia, Guinea-Bissau, Guinea, Sierra Leone, Liberia, and Cote d'Ivoire). The rainfall decline exceeds 1.0 mm $day^{-1}$ $century^{-1}$ here (i.e., a 10%–25% decline in seasonal rainfall over the course of the twentieth century). The boreal spring decline is most impressive, percent-wise, and must lead to an increasing delay in the build-up of Niger stream flow after the dry winter season.

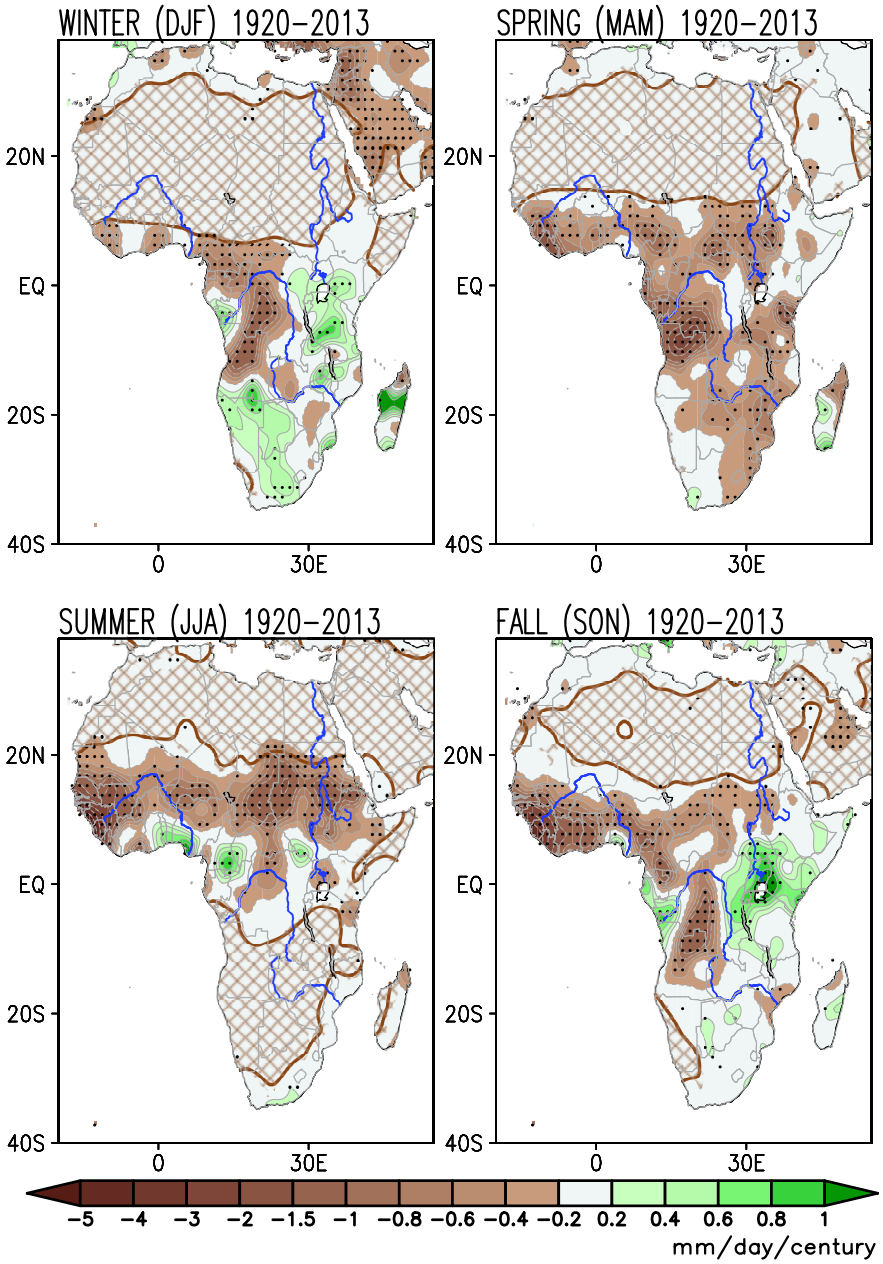


**Figure 4.8** Linear trends in seasonal precipitation over the African continent during 1902–2013, from the 0.5° resolution GPCC dataset (mm day$^{-1}$ century$^{-1}$). Thick solid brown contours mark the 0.274mm day$^{-1}$ climatological precipitation isoline, and brown hatching indicates regions where climatological precipitation is below 0.274mm day$^{-1}$ (or 100mm yr$^{-1}$)—a precipitation threshold used for defining the Sahara Desert. Trends significant at the 95% confidence level are denoted with black dots.

Figure 4.9 shows the monthly stream flow climatology (red line) and trends

(black bars) over the 1907–90 period at a monitoring station in the Niger River source region. Climatological stream flow is weakest in spring even though regional precipitation is not a minimum in this season (Figure 4.4) in part because spring rainfall is effectively used in recharging soil moisture after the dry season (boreal winter). Even otherwise, a 1–2-month lag of stream flow vis-à-vis regional precipitation is not uncommon because of the aggregation and drainage delays generated in large watersheds, and the temporal phasing of other surface water losses (e.g., evapotranspiration). The stream flow peaks in September, following the wet season (June–August; Figure 4.4), again with some delay. It is thus not surprising that the stream flow trend is most negative in fall— that is, following the season of most negative precipitation trends (summer, Figure 4.8). The decline in Niger River's source region stream flow in September is very steep: A $15m^3\ s^{-1}$ yearly decrease, or a $1500m^3\ s^{-1}$ centennial decrease where the climatological flow is ~$5000m^3\ s^{-1}$, represents a 30% reduction over the twentieth century. While declining precipitation trends in the proximity of the Niger River likely play a major role in the reduction of stream flow, other factors may also contribute. Increased evapotranspiration in this region or human intervention via dams and agricultural use could also cause a reduction in stream flow.

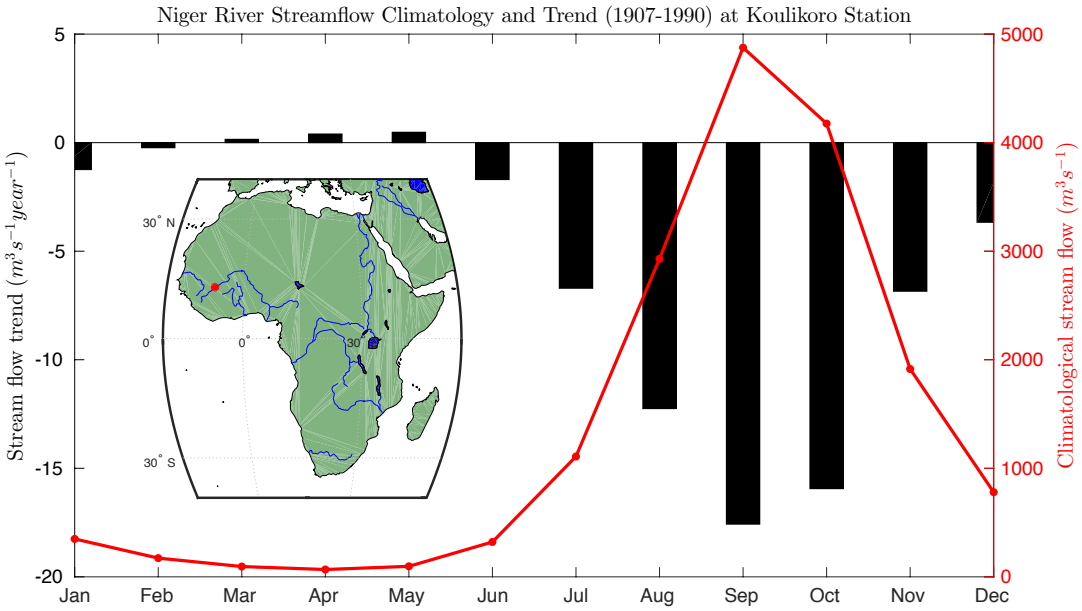


**Figure 4.9** Monthly stream flow climatology (red line; right axis; $m^3$ $s^{-1}$) and trend (black bars; left axis; $m^3$ $s^{-1}$ $yr^{-1}$) for the 1907–90 period at the Koulikoro monitoring station (12.8878N, 7.548W) in western Mali. The station location in the source region of the Niger River is shown using the red dot in the inset map.

Another region showing rainfall decline in all seasons is the Congo River basin, especially the part encompassing Angola and the Democratic Republic of the Congo. Rainfall decline here is impressive in the shoulder seasons (spring and fall), with trends exceeding 0.6 mm $day^{-1}$ $century^{-1}$ where seasonal rainfall is 6.0 mm $day^{-1}$. The thick brown lines in Figure 4.8 mark the climatological dry zones, facilitating a visual assessment of desert expansion–contraction over the twentieth century (the focus of section 4.5). Precipitation declines are also seen over Lake Chad in spring and summer; the shrinking of Lake Chad is a well-noted feature of African Climate Change (Gao et al. 2011) – see Okonkwo et al. (2015) for the century-long time series of the lake level.

The African Great Lakes region, especially Victoria and Tanganyika, is one of the few regions on the continent exhibiting increasing twentieth-century rainfall,

mostly in austral spring and summer. This is interesting because of the proximity of this region to the source of the Nile River, and implications for stream flow in the downriver region.

### 4.4.3 Annual SAT and precipitation trends

The advantages of a seasonal rather than an annual mean perspective in the context of centennial change in regional hydroclimate over Africa can be gleaned from a comparison of Figures 4.6 and 4.8 with their annual-mean counterparts. Figure 4.10 displays the linear trends in annual SAT and precipitation over Africa. While annual-mean trends clarify the regions of greatest warming and drying on the continent, they can mask notable subannual (i.e., interseasonal) variations in trends that can modulate the regional seasonal cycle: For example, Figure 4.10 shows maximum annual SAT trends over Sudan and northern Africa but the amplification of the seasonal cycle and related intensification of heat distress is only ascertainable from the structure of seasonal trends, as discussed in section 4.4.1. The annual perspective can sometimes be misleading as well, as in the case of precipitation trends over Kenya/Tanzania (Figure 4.8), which are notable in most seasons but offsetting, leading to an annual-mean trend of close to zero. The impact on agriculture, however, need not be negligible as it is sensitive primarily to the growing seasons' trends.

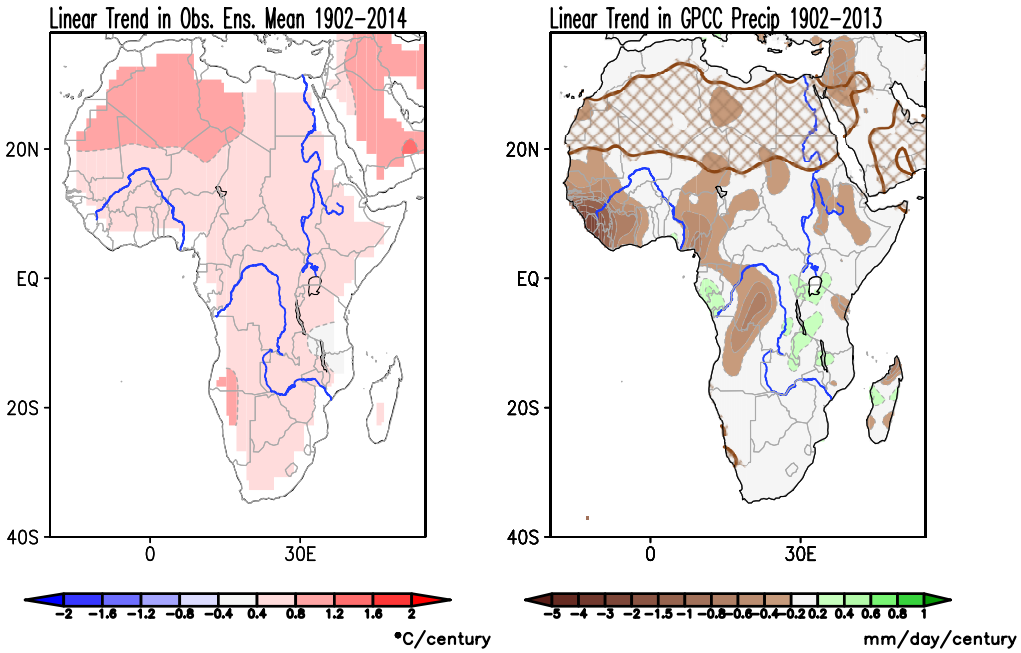


**Figure 4.10** Linear trend in annual-mean (left) SAT (°C century$^{-1}$) and (right) precipitation (mm day$^{-1}$ century$^{-1}$) over the 1902–2014 period (1902–2013 for precipitation). The SAT trend is the average of the trends in three independent analyses of SAT observations (as in Figure 4.6), while the precipitation one is based on the GPCC analysis (as in Figure 4.8). Thick solid brown contours mark the 100mm yr$^{-1}$ climatological annual-mean precipitation isoline, and brown hatching indicates regions where climatological annual-mean precipitation is less than 100mm yr$^{-1}$. Both datasets are at 0.5° resolution. Contour and shading interval is 0.4°C century$^{-1}$ for SAT and as indicated by the brown–green color bar for precipitation.

## 4.5 Change in the expanse of the Sahara Desert over the twentieth century

The overlay of twentieth-century precipitation trends on the climatological dry zones in Figure 4.8 suggests that the Sahara Desert has expanded both equatorward and northward. The Sahara's extent has been investigated using vegetation-zone boundaries as markers of desert expanse and its interannual variation (Tucker and Nicholson 1999; Tucker et al. 1991). Although interesting because of the implicit seasonal context, these studies analyzed short records such as the recent 10–17-yr-long satellite-era ones. Unfortunately, desert trends over such periods reveal little

about the secular changes in the Sahara because of the potential aliasing of decadal to multidecadal variability into short period trends. Still, the results of the current analysis are compared against those of (Tucker and Nicholson 1999) for the common overlap period in section 4.5.2 (Figure 4.15).

Here, we use the precipitation rate to demarcate the desert region. The use of precipitation rather than vegetation allows analysis of a longer record notwithstanding the spatiotemporal sparseness of the precipitation record in the early twentieth century. A direct relationship between precipitation and the vegetation index found in previous studies (Tucker and Nicholson 1999; Tucker et al. 1991) supports such a strategy. In Figure 4.8, a 100mm $yr^{-1}$ (or 0.274mm $day^{-1}$; one of the thresholds discussed in section 4.2.3) precipitation isoline demarcates the deserts, seasonally (and in Figure 4.10, annually). A light brown hatching of the regions where climatological precipitation is less than this value marks the desert expanse, which is monitored using the two methods discussed in section 4.2.3

### 4.5.1 The Sahara's advance

The twentieth-century change in the Sahara Desert's seasonal and annual extent is displayed in Figures 4.11 and 4.12; the change is estimated using the endpoint method. Brown shading, which represents the desert's advance over the century, shows significant northward creep in boreal winter albeit not uniformly across longitudes; hefty footprints over Libya and Algeria in the central sector, and over the western Sahara and Mauritania to the west, characterize the northward expansion in winter. The desert has encroached equatorward as well in winter, with notable intrusions in Nigeria, Cameroon, and the Central African Republic.

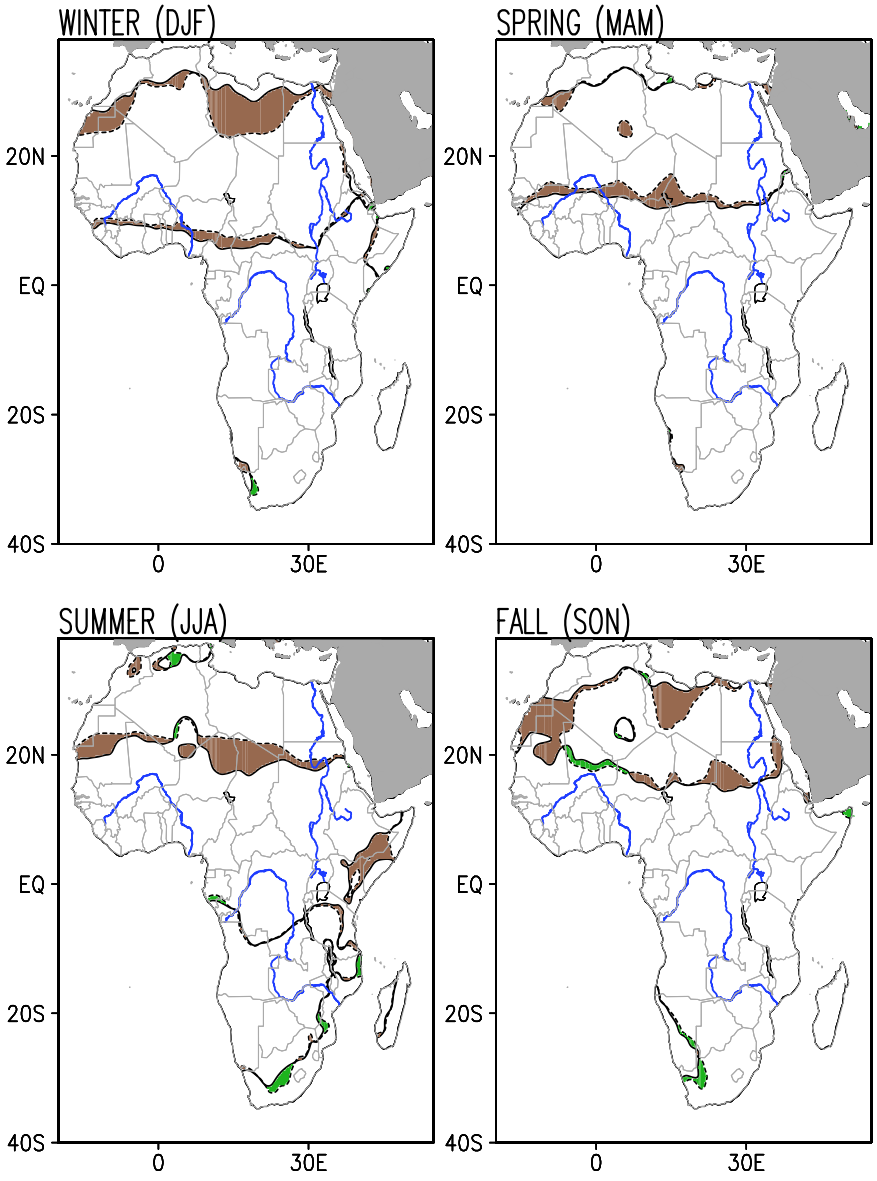


**Figure 4.11** Advance or retreat of the Sahara Desert over the 1902–2013 period, seasonally. The dashed (solid) brown lines denote the 0.274mm day$^{-1}$ precipitation isolines in the synthetic 1902 (2013) precipitation map obtained from the endpoint analysis. The brown (green) shaded areas denote desert advance (retreat).

The centennial change in the Sahara's summer extent is through the equatorward advance of its southern boundary (Figure 4.11) which is climatologically located at ~20°N because of robust summer rainfall in the northern tropics including the Sahel (0°–20°N; cf. Figure 4.4). Much as with the winter desert advance at the northern boundary, the southern advance is sectorally focused, with intrusions in

Mauritania to the west and Niger and Chad in the central sector. The countries most impacted by the Sahara Desert's seasonal advance are listed in Table 4.1.

**Table 4.1** Expansion of the Sahara Desert seasonally during 1902–2013, based on the movement of the 100 and 150mm $yr^{-1}$ precipitation isolines. The expansion is computed using both area-trend and endpoint methods; endpoint values are in parentheses. The areal values are rounded off to the nearest 1000 $km^2$ (which is about 1/3 of the 0.5° grid cell area at the equator).

| | **Thres-hold (mm year$^{-1}$)** | **Winter (DJF)** | **Spring (MAM)** | **Summer (JJA)** | **Fall (SON)** |
|---|---|---|---|---|---|
| **Climatological Sahara Extent (km$^2$)** | **100** | 13,686,000 (12,868,000) | 10,540,000 (9,979,000) | 7,725,000 (6,198,000) | 7,583,000 (6,163,000) |
| | **150** | 14,557,000 (13,872,000) | 11,420,000 (10,782,000) | 8,492,000 (7,351,000) | 8,736,000 (8,018,000) |
| **Sahara Expansion (km$^2$)** | **100** | 2,246,000 (2,348,000) | 1,287,000 (1,132,000) | 876,000 (1,594,000) | 1,354,000 (2,048,000) |
| | **150** | 1,800,000 (1,433,000) | 1,009,000 (627,000) | 847,000 (1,478,000) | 999,000 (1,366,000) |
| **Sahara Expansion (% of Climatological Area)** | **100** | 16% (18%) | 12% (11%) | 11% (26%) | 18% (33%) |
| | **150** | 12% (10%) | 9% (6%) | 10% (20%) | 11% (17%) |

| | | | | | |
|---|---|---|---|---|---|
| **Countries Affected (**obtainable only from the endpoint method; the ones in bold are most impacted**)** | | **Libya,** Egypt, Tunisia, Algeria, Morocco, **Western Sahara**, Mauritania, **Central African Rep**., **Cameroon**, Nigeria, Guinea, Cote D'ivoire, Ghana, Togo, Benin | Morocco, Sudan, **Chad, Niger**, Nigeria, Burkina Faso, **Mali**, Senegal, Guinea | **Mauritania**, Western Sahara, Mali, Algeria, **Niger**, **Chad**, Libya, Sudan | **Libya**, Egypt, Algeria, Morocco, **Western Sahara**, **Mauritania**, Niger, Chad, **Sudan** |

A similar demarcation of the Sahara Desert advance is obtained from the independently analyzed University of Delaware precipitation dataset (Willmott and Matsuura 2015) and shown in Figure 4.13, allaying dataset dependency concerns. The annual-mean desert advance (using the 100mm $yr^{-1}$ threshold; see Figure 4.12), provides context for the seasonal analysis and comports with the canonical desert definitions based on the annual-mean rainfall threshold (Tucker and Nicholson 1999). The annual-mean advance shows primarily southward creep relative to the annual-mean desert boundaries (see Figure 4.10).

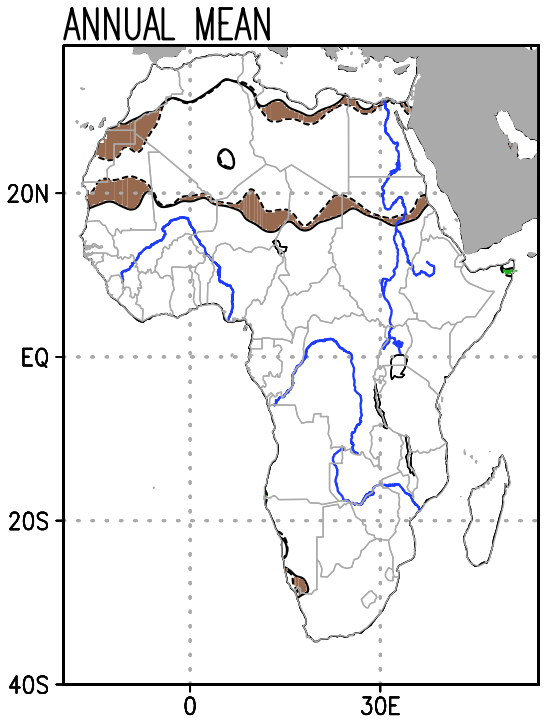


**Figure 4.12** As in Figure 4.11, but for the advance or retreat of the Sahara Desert over the 1920–2013 period, annually. Desert identification here is fully consistent with the canonical desert definition based on annual-mean rainfall: a 100mm $yr^{-1}$ threshold is used.

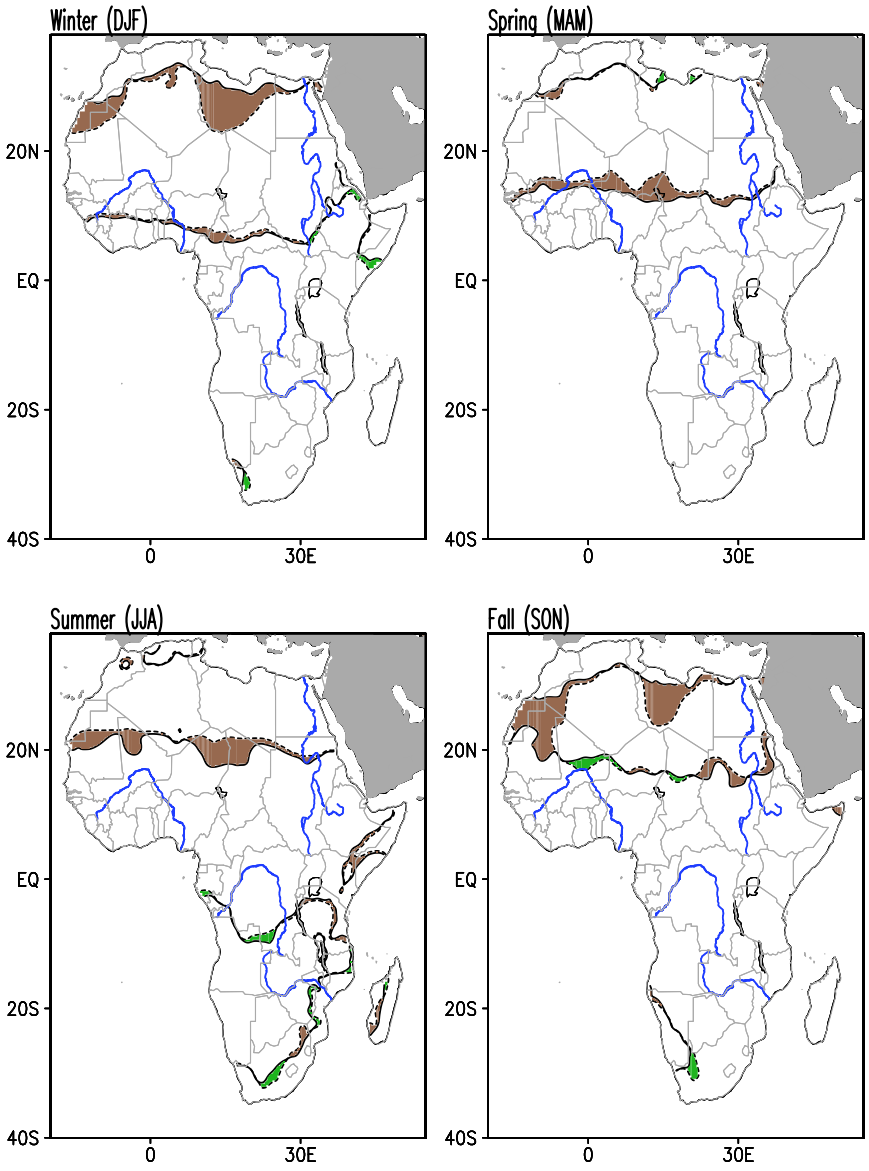


**Figure 4.13** As in Figure 4.11, but for the University of Delaware precipitation dataset.

### 4.5.2 The Sahara's expanse

A quantitative analysis of the centennial change in the Sahara Desert's seasonal and annual-mean expanse is reported in Table 4.1. The primary analysis is based on the area-trend method but the endpoint method that generated Figures 4.11 and 4.12 is also used with both desert definitions to assess the sensitivity of the desert

expansion to analysis methods. As noted above, the expansion has been largest (area-wise) in boreal winter (2,246,000 $km^2$, a 16% increase) and smallest in summer (876,000 $km^2$, an 11% increase) using the area-trend method with a 100mm $yr^{-1}$ threshold. Estimates of desert expansion from the endpoint method (noted in parentheses in Table 4.1), with the same threshold, yield maximum desert expansion in winter (2,348,000$km^2$, an 18% increase) and a minimum in spring (1,132,000$km^2$, an 11% increase). The endpoint method, however, yields significantly larger expansions in boreal summer and fall. As noted in section 4.2.3, the two estimates can differ when multidecadal variability is potentially aliased into centennial trends—the case in summer and fall when the 65–70-yr time scale AMO variability (Kavvada et al. 2013; Schlesinger and Ramankutty 1994) exerts strong influence on Sahel rainfall (Nigam and Ruiz-Barradas 2016; Zhang and Delworth 2006). Percent-wise, the desert expansion is largest in boreal fall from both methods.

The sensitivity of the desert expansion rate to the desert-defining precipitation-threshold is also reported in Table 4.1. A less stringent definition, based on a 150mm $yr^{-1}$ threshold, leads to more expansive deserts, not surprisingly, but also to smaller centennial expansions, indicating a tightening of the meridional precipitation gradient over the century. This is shown visually in Figure 4.14, which shows the twentieth-century change in the Sahara Desert's seasonal extent using the 150 mm $year^{-1}$ threshold. As Table 4.1 shows, with the less stringent threshold, percentages drop on both counts but the Sahara's expansion remains robust with the largest expansion, as before, in boreal winter (1,800,000 $km^2$, a 12% increase); this winter expansion, from the area-trend method, is largest both area- and percent-wise.

The weakest expansion again is in summer (847,000 km$^2$, a 10% increase). Results from the endpoint method using the larger threshold are qualitatively similar to those obtained with the lower one.

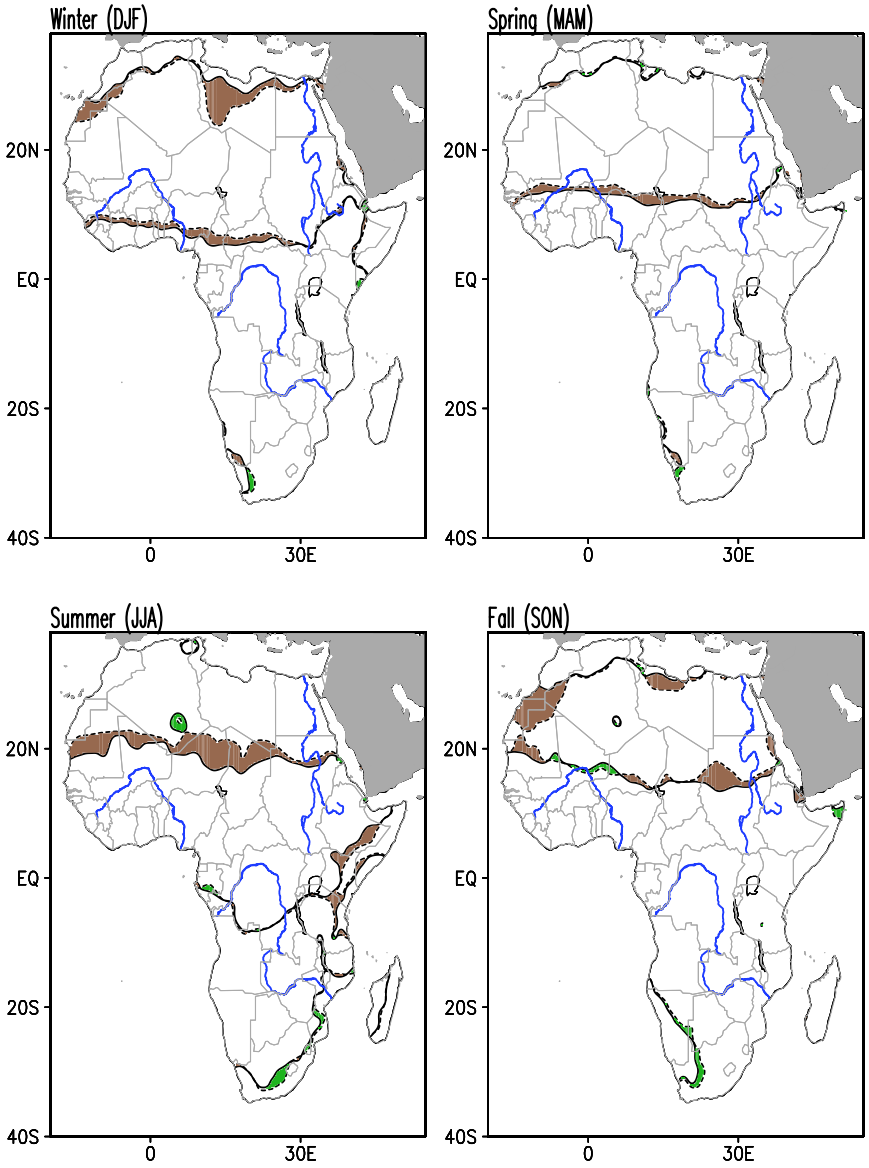


**Figure 4.14** As in Figure 4.11, but using the less stringent precipitation threshold of 150 mm year$^{-1}$.

The sensitivity analysis indicates that while desert expansion and the related area percentage vary somewhat with the desert definition and analysis method, one

can reasonably conclude that the Sahara Desert has grown larger, area-wise, more in winter than in summer; percentage-wise, the summer expansion can be larger in view of the smaller (nearly halved) climatological desert expanse in summer. The countries bearing the brunt of the Sahara's northwestward–northward advance in fall–winter are Libya, Mauritania, and Western Sahara; the southern advance principally impacts Niger, Chad, and Mauritania in summer, and Sudan in fall. One would be remiss to not note the summer desertification in the Horn of Africa, especially Ethiopia and Somalia. Notable against this backdrop of widespread desert advance (brown shading) over the northern continent is a sliver of green over Mali in fall, reflecting the Sahara's retreat.

The expansion of the Sahara Desert is also analyzed using the conventional annual-rainfall based desert definition. Given that this was the definition used in earlier studies of the size of the Sahara Desert (Tucker and Nicholson 1999; Tucker et al. 1991), a comparison is possible. Figure 4.15 shows the time series of the annual-mean Sahara expanse, computed using the area-trend method and a 200mm $year^{-1}$ threshold. The red line shows the size of the Sahara Desert reported in Tucker and Nicholson (1999) for 1980-1997 based on a satellite derived vegetation index. The 200mm $year^{-1}$ threshold, despite being the boundary of the Sahel rather than the Sahara, is used in their study because their vegetation index is not useful below this isoline. The interannual variability of the desert expanse is similar for the current analysis and that of Tucker and Nicholson (1999). For the common period of 1980-1997, the two time series are correlated at 0.81.

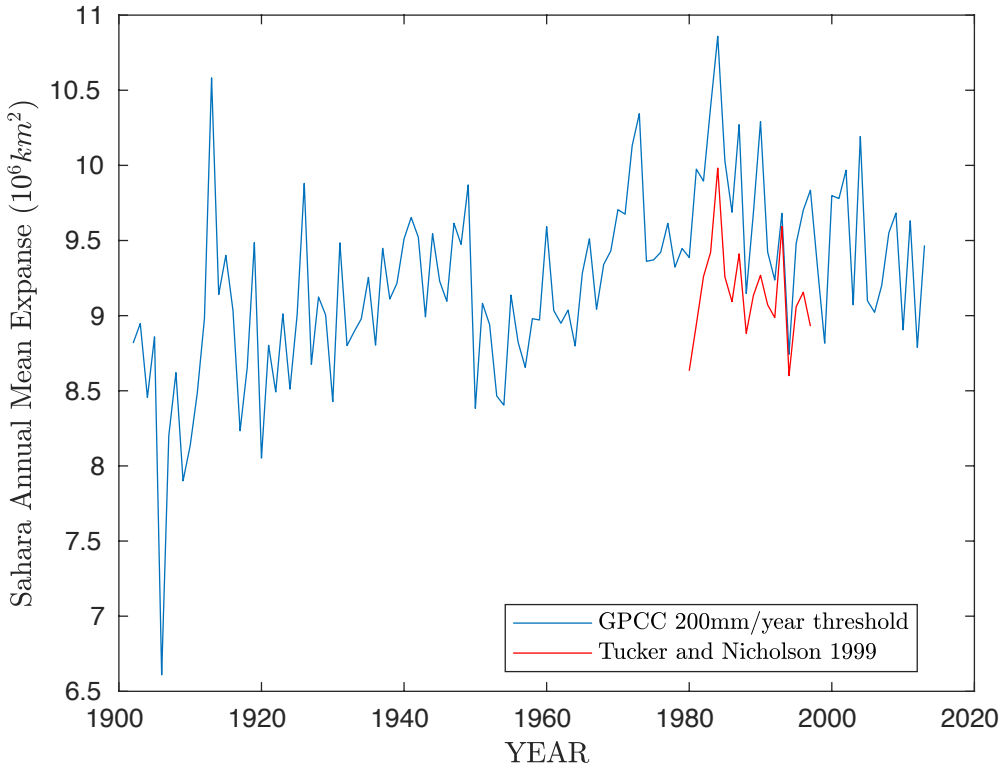


**Figure 4.15** Annual-mean expanse of the Sahara Desert (km$^2$). The blue line shows the expanse of the desert computed using the area-trend method and a 200 mm year$^{-1}$ threshold for 1902 to 2014. The red line shows the values for the size of the desert computed by Tucker and Nicholson (1999).

Table 4.2 notes the findings from the area-trend and endpoint methods for both the 100 and 150 mm yr$^{-1}$ annual-rainfall thresholds. A slightly shorter period, beginning in 1920, is analyzed in the annual case in order to focus on the relatively stable rain gauge network period (S. Nicholson 2018, personal communication; and see Figure 4.2). During 1920–2013, the Sahara expanded by over 700,000 km$^2$ (or ~7,600km$^2$ yr$^{-1}$) based on the 100 mm yr$^{-1}$ definition, indicating a ~10% expansion over its climatological area (7,426,000 km$^2$). The desert's southward creep (cf. Figure 4.12) is the major contributor (~554 000 km$^2$ or 7.5%) to the expansion; the northward advance (182,000 km$^2$) contributes the remaining 2.5%. The linear trend in

the Sahara Desert's expanse is sensitive to the analysis period from the potential aliasing of multidecadal variability, as noted earlier.

**Table 4.2** Expansion of the Sahara Desert annually during 1920-2013, based on the movement of the 100 and 150 mm $yr^{-1}$ precipitation isolines. All other formatting as in Table 4.1**.**

| | | |
|---|---|---|
| Climatological Sahara extent ($km^2$) | 100 mm $year^{-1}$ | 7,426,000 (6,890,000) |
| | 150 mm $year^{-1}$ | 8,528,000 (7,947,000) |
| Sahara Expansion ($km^2$) | 100 mm $year^{-1}$ | 711,000 (738,000) |
| | 150 mm $year^{-1}$ | 718,000 (549,000) |
| Sahara Expansion (% of climatological area) | 100 mm $year^{-1}$ | 10% (11%) |
| | 150 mm $year^{-1}$ | 8% (7%) |
| Countries Affected | | Libya, Egypt, Algeria, **Western Sahara**, **Mauritania**, **Mali**, Niger, **Chad**, **Sudan** |

Unlike northern Africa, the southern continent is devoid of any desert advance, in any direction or season. To the contrary, the Namib/Kalahari Desert is found retreating, albeit modestly, in austral winter (JJA) and spring (SON) when it is, climatologically, most expansive (cf. Figure 4.4).

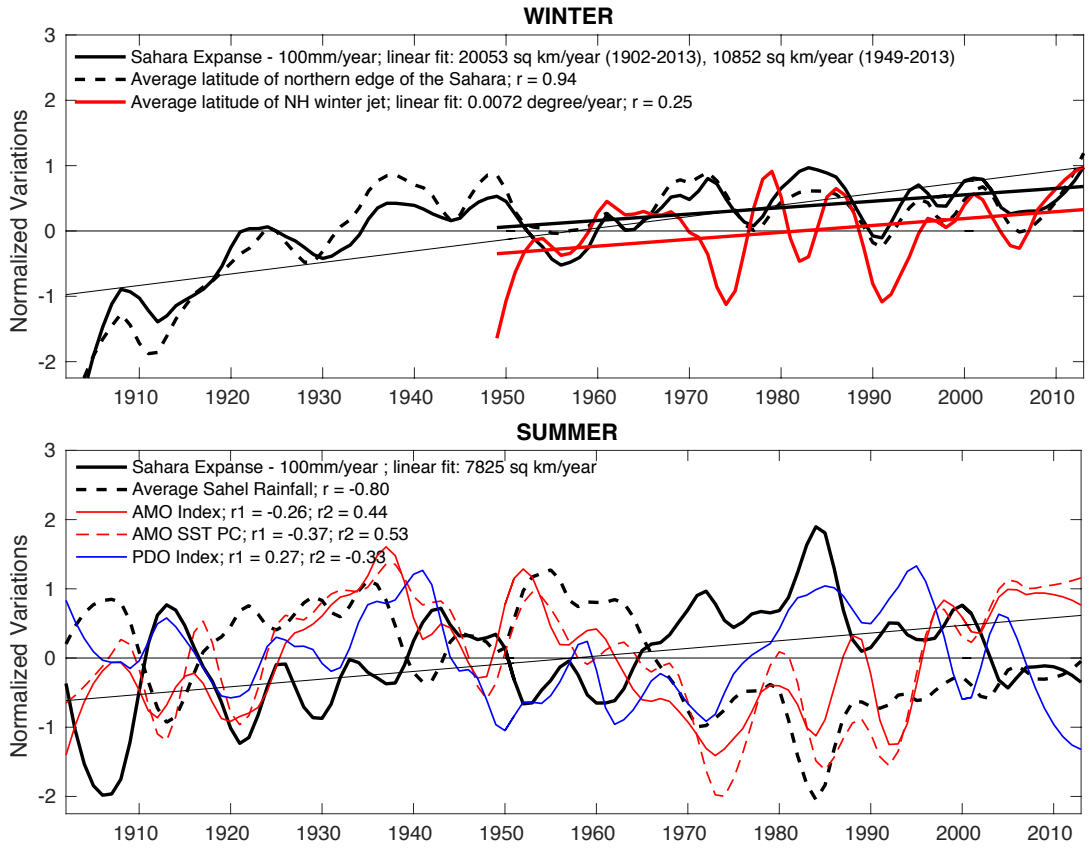


**Figure 4.16** The Sahara Desert's expanse during 1902–2013. The boreal (top) winter and (bottom) summer expanse is shown using the thick solid black line. The thin black straight line is the linear fit to the desert expanse over the entire period; it is the basis of the area-trend analysis reported in Table 4.1. The thick black line is the linear fit to the winter desert expanse during 1949–2013—the period for which the latitude of the winter subtropical jet is plotted (solid red line, top). The Sahara expanse trend is significant at the 95% level in winter (both periods) and summer. Indices of SST and rainfall variability with potential links to the Sahara Desert's summer expanse are shown in (bottom), along with their correlation coefficients. For each index, r1 (r2) is the correlation between the index and Sahara expanse (Sahel rainfall). The AMO and PDO are displayed using their common SST indices; an SST principal component (PC)-based AMO index is also shown. The rainfall over the Sahel is plotted as well. All time series depict normalized anomalies after 10% Loess smoothing; the time series for the latitude of the Northern Hemisphere (NH) subtropical jet was smoothed with a 20% Loess function. All time series are normalized by their standard deviations.

## 4.6 The Sahara's expanse: variation and potential mechanisms

The Sahara Desert's expanse during the 1902–2013 period, and not just at its

endpoints, is the focus of this section. The desert expanse in winter and summer is plotted in Figure 4.16, along with select indices of circulation and SST variability that can provide insights on causal mechanisms.

### 4.6.1 Winter Variations

The Sahara's winter expanse (Figure 4.16, top) is plotted together with the average latitude of the desert's northern edge using methods described in section 4.2.3. The location of the northern edge is of interest because the endpoint analysis (Figure 4.11) showed the twentieth-century expansion to be, principally, through the northern boundary. Not surprisingly, winter variations in the Sahara Desert expanse correlate well with the latitudinal position of the desert's northern boundary (Figure 4.16, top); r =0.94 (0.88) for smoothed (unsmoothed) indices; note that the high, statistically significant correlation emerges not just from similar upward trends but also from the correspondence in decadal variations. The linear fit to the Sahara's winter expanse is shown by the thin black line, which is the basis for the area-trend analysis (Table 4.1).

We hypothesize that the Sahara Desert's northward expansion in winter is due, largely, to the widening of the tropics (Seidel et al. 2008), based on canonical understanding of the desert's location (cf. section 4.3) relative to the descending branch of the Hadley circulation. As the descending branch terminus, which defines the width of the tropics, dynamically, is collocated with the core latitude of the subtropical jet in the upper troposphere (James 2003), the latter serves as a convenient proxy for the width of the tropics. Previous studies have shown that the core of the northern winter subtropical jet has moved poleward in recent decades (Archer and

Caldeira 2008). The 30°W–60°E sector-averaged latitudinal position of the jet in the NCEP-NCAR reanalysis (Kalnay et al. 1996), computed using these authors' method, is shown by the red line in Figure 4.16 (top), along with a linear fit to its variation. While both the Sahara's expanse and the subtropical jet-latitude depict upward trends—and nearly identical ones (0.98% and 1.05% $yr^{-1}$, respectively) when for the same period (1949–2013)—the two variations are modestly correlated (r=0.25; not significant at the 95% level), notwithstanding periods (1950–65 and 1985–2013) when they track each other closely. The similar upward trends over the recent 65-yr period lend credence to the hypothesis linking the Sahara's increasing winter expanse (and northern extent) to a secular change in the width of the tropics. The modest correlation between the two on decadal (and shorter) time scales, while detracting, attests to the influence of other processes on the desert expanse in winter, such as tropical SSTs and the North Atlantic Oscillation (through its impact on winter storm tracks; e.g., (Linkin and Nigam 2008)).

### 4.6.2 Summer Variations

Summer variations in the Sahara Desert's expanse, unlike winter ones, arise mainly from the north–south movements of its southern boundary, which borders the Sahel. The summer expanse (solid black line) exhibits both an upward trend, highlighted by the linear fit (thin black straight line), and notable decadal–multidecadal variations. As areal changes result from the equatorward advance or poleward retreat of the desert's southern edge, the Sahara's summer expanse should be inversely linked to Sahel rainfall (defined in section 4.2.1), which is plotted with a dashed black line. The inverse relationship can be visually discerned: for example, the

drying of the Sahel (a multidecadal decline in Sahel rainfall from the mid-1950s to the mid-1980s) is coincident with the Sahara's expansion; the full-period correlation (r=-0.80; significant at the 95% level) points to a strong inverse relationship. The anticorrelation allows tapping into extensive analyses of Sahel rainfall variability in the attribution of the summer waxing and waning of the Sahara Desert.

The Sahel rainfall has been linked to AMO variability among other processes, as noted in section 4.1. To assess links between AMO and the Sahara's extent, two markers of AMO variability are plotted in Figure 4.16 (bottom) along with their correlations to the Sahara's expanse and Sahel rainfall. The AMO SST principal component (dashed red line), obtained from an evolution-centric spatiotemporal analysis of seasonal SST anomalies in the twentieth century (Guan and Nigam 2009), shows higher correlations with both the Sahara's expanse (r=-0.37; significant at the 80% level) and Sahel rainfall (r=0.53; significant at the 95% level) in boreal summer.

Decadal SST variability in the Pacific basin, as typified by the Pacific decadal oscillation (Mantua et al. 1997), is also linked with Sahel rainfall (Nigam and Ruiz-Barradas 2016; Villamayor and Mohino 2015) albeit not as strongly as the AMO. The PDO index, shown in Figure 4.16 (solid blue line), is correlated with Sahel rainfall and the Sahara's expanse at -0.33 (significant at the 90% level) and 0.27 (significant at the 75% level), respectively. A statistical link between the PDO and Sahel rainfall seems more intriguing than the rainfall's link with the AMO because the AMO SST anomalies are proximal, with their tropical footprints offering potential mechanisms for their influence. In contrast, the PDO SST anomalies are distant and focused in the midlatitudes, disadvantaging them from the influence potential perspective, especially

as only the tropical SST anomalies are generally viewed as influential on faraway regions. Interestingly, these disadvantages disappear once one recognizes that the PDO is not without tropical links Guan and Nigam (2008) showed the PDO counterpart in their spatiotemporal analysis [called by them Pacific decadal variability–North Pacific (PDV-NP)] to be linked with the tropical Indian and Pacific basin SSTs; see also Deser et al. (2004). The PDO's modest influence on Sahel rainfall, if realized through its tropical Indian Ocean footprints, would be consistent with the findings of Hagos and Cook (2008).

Secular change is often characterized using the century-long linear trends in observational records, as for the Sahara's expanse in Figure 4.16. The linear trend is however susceptible to the aliasing of multidecadal variability should the latter be prominently manifest in the record, as is the case in summer (cf. Figure 4.16).

The origin of the 112-yr linear trend (referred to as the secular trend) in the Sahara's summer expanse remains to be elucidated; the elucidation is challenging, especially, for an observational analysis. Trends on centennial and longer time scales can potentially result from the interaction of multidecadal variabilities (e.g., the PDO and AMO) and, of course, from the increasing concentration of greenhouse gases and aerosol loading (Held et al. 2006) and the related change in SST distribution (Nigam and Ruiz-Barradas 2016).

### 4.6.3 Annual-mean Variations – Role of Multidecadal Variability

The seasonally stratified analysis of hydroclimate trends—the focus of the study—was complemented by analyses of the annual-mean trends. The latter, more directly relatable to deserts in view of the canonical annual rainfall-based desert

definition, also revealed impressive expansion rates for the Sahara Desert over the twentieth century (Table 4.1). The rate is however sensitive to the analysis period, from exposure to the aliasing of multidecadal variability (e.g., AMO and PDO) and variability of the rain gauge network. Figure 4.17 plots the linear expansion rate of the Sahara Desert's annual expanse over two different multidecadal periods, both ending in 2013; the rates are quite variable, ranging from 9.9% to 23%, likely from the impact of the coarse rain gauge network in the early part of the 20th century.

The aliasing of multidecadal variability in the linear trend in the Sahara's annual-mean expanse is directly investigated during the relatively stable rain-gauge network period (1920 onwards) in Figure 4.17. The AMO and PDO influences are removed from the precipitation record via linear regression. The seasonally stratified precipitation fields are regressed onto the seasonal AMO and PDV-NP SST principal components (PCs, which are orthonormal; (Nigam et al. 2011)) over the full period (1902–2013). The influence of these multidecadal variability modes is computed by multiplying their time-independent regression coefficients by their time-varying PC, seasonally. The influence is then subtracted from the precipitation record, and the desert expanse recomputed. The annual-mean Sahara Desert expanse sans the multidecadal modes' influence is shown in Figure 4.17 by the red curve. The AMO's and PDO's influence is strong during the 1970s–90s when the red curve diverges from the black one; their contribution to the drying of the Sahel during the 1950s–80s is evident. The different linear trends of the two time series indicate that about two-thirds of the; 10% increase in the Sahara Desert's annual-mean expanse during 1920-2013 is attributable to multidecadal SST variability, and the remaining one-third to

the rising greenhouse gas concentrations and aerosol loadings, and other factors.

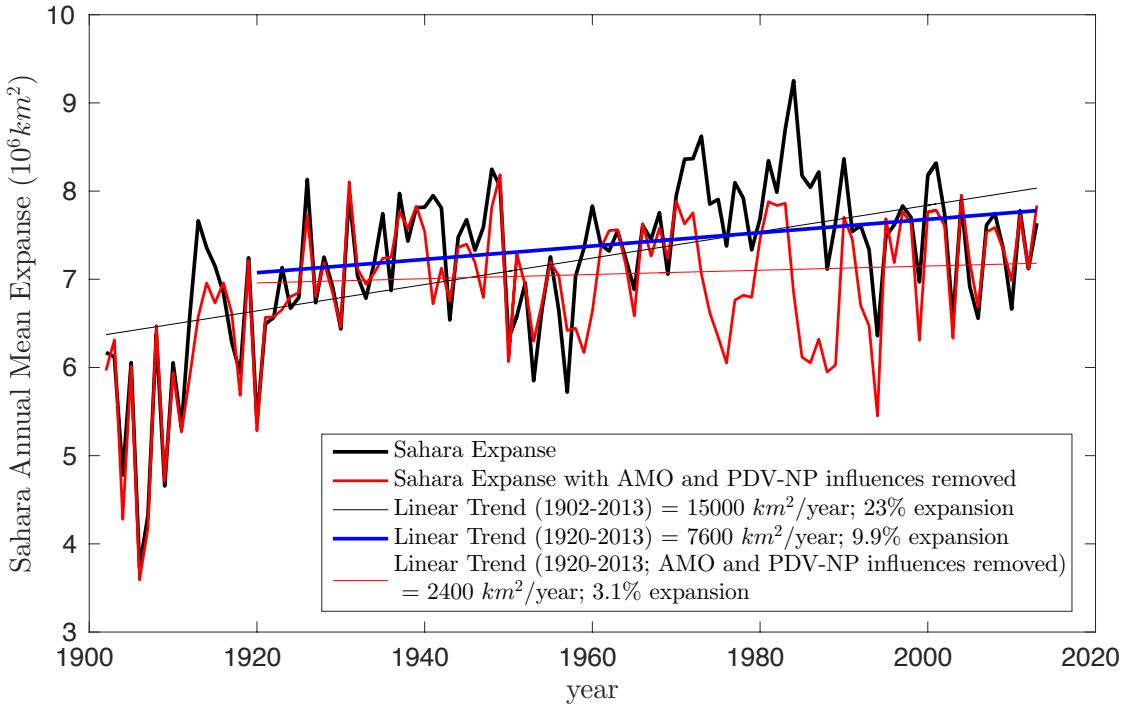


**Figure 4.17** Annual-mean Sahara Desert expanse (km$^2$; computed from the area-trend method). Linear trends are shown for 1902–2013 (thin black line) and 1920–2013 (thick blue line); the values are noted in the legend. The red curve and the corresponding 1920–2013 linear trend (thin red line) track desert expanse after removal of the AMO's and PDO's influence from the precipitation data set. The area-expansion percentages are all computed using the 1902–2013 climatological desert expanse.

## 4.7 Simulation of twentieth-century hydroclimate trends by IPCC-AR5 climate models

Climate system models contributing to the IPCC AR5 typically run in the projection mode, yielding 50–100-yr climate change projections for various greenhouse gas concentration scenarios. The very long-lead nature of climate projections and the implicit lack of exposure of climate-change modeling to the forecast-verification cycles make model evaluation (and improvement) challenging.

The few available options include assessment of the veracity of historical simulations by the same models, such as of the modeled twentieth-century secular trend in SAT for which validating observations exist. Related assessments at seasonal resolution accord additional precious evaluative opportunities—seized in this analysis—especially as the observed twentieth century SAT trends exhibit striking seasonality over many Northern Hemisphere continents (Nigam et al. 2017). Although characterization of projected climate change over Africa is beyond the scope of this study, an evaluation of historical simulations is important for providing weights for model projections during construction of the ensemble-averaged projection from a multitude of models that differ widely in their historical simulation capabilities.

The winter and summer simulations produced by five IPCC AR5 participant models (two U.S. and three European models) are analyzed. We chose not to analyze the entire CMIP5 model suite in the interest of an in depth analysis of each model's simulations, including all of its ensemble members. Examining models individually is important for determining which ones will likely provide reliable hydroclimate projections. The five chosen models were developed at the leading climate modeling centers in the United States and Europe, and have been extensively analyzed and used for mitigation and adaptation planning.

The SAT and precipitation trends over the 103-yr historical simulation period (1902–2004), averaged across ensemble members from each model, are shown in Figure 4.18; observed trends over the same period (i.e., the simulation target) are shown at the top of each column. The simulated SAT trends are varied and, mostly, inconsistent with the observed ones. For example, the observed trends in winter are

notable over the so-called Hump of Africa—the northwestern protrusion of the continent—but none of the simulated trends, except for NCAR's, have this focus. Likewise, summer SAT trends are noteworthy over the Mediterranean rim countries of Algeria, Tunisia, and Libya but absent in the majority of analyzed simulations, with the MPI, and to some extent NCAR, being the exceptions. The austral winter warming over southern Africa, in contrast, is reasonably captured in many simulations but not by GFDL's. Finally, the robust seasonality in observed SAT trends, for example, around Lake Chad but especially to its northeast, is not captured in most simulations.

The observed and simulated twentieth-century precipitation trends are displayed in the right columns of Figure 4.18. The austral summer trends consist, principally, of an east–west dipole over southern Africa, with wetting trends over the African Great Lakes. The trend structure is, to an extent, present in the NCAR simulation but in no other. The intense drying trend over tropical West Africa and the Sahel interior (the region around and to the east of Lake Chad, up to Ethiopia and Somalia) in boreal summer has no serious counterpart in the historical simulations except for NCAR's and, to an extent, GFDL's; the drying trends in other simulations are weak (in the noise range) and/or misplaced. Perhaps the historical simulations not examined in this analysis perform better as some investigators have found this simulation ensemble capable of reproducing the large-scale twentieth-century drying of the Sahel, including seasonal aspects (Biasutti 2013).

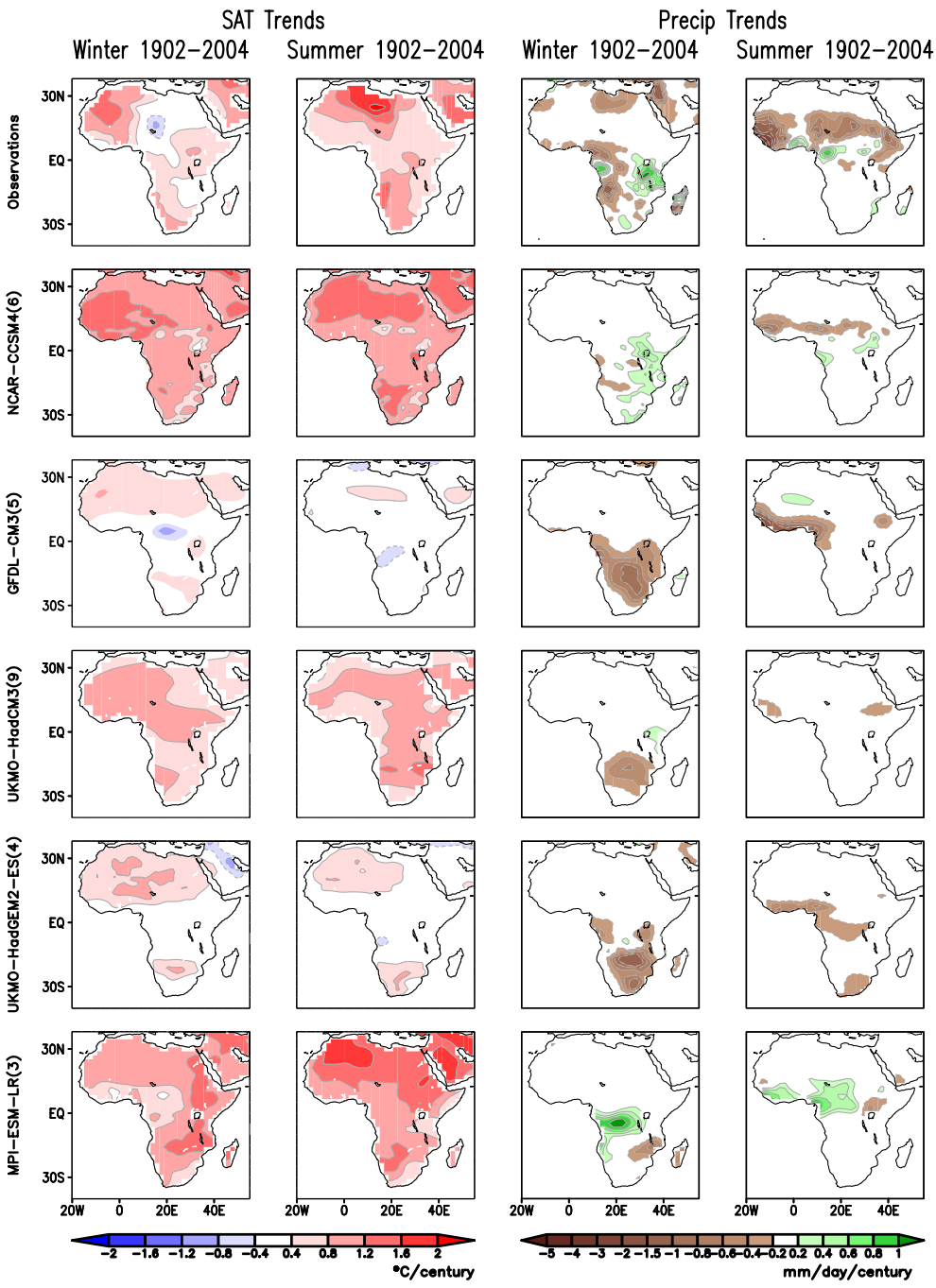


**Figure 4.18** The linear trend in boreal winter and summer (left) SAT and (right) precipitation averaged across all ensemble members of the model's twentieth-century (1902–2004) historical simulation produced for the IPCC AR5; simulations from five models are analyzed. (top) The observed SAT trend is the average of three independent analyses of SAT, while the observed precipitation trend is from the GPCC analysis. The number of ensemble members is indicated in parentheses next to the model's name.

## 4.8 Conclusions

The footprints of climate change over the African continent are widely noted (Niang et al. 2014) but even region-specific descriptions seldom stray from the annual-mean displays of hydroclimate trends—and this over the African continent, where the seasonal waxing and waning of the Sahara Desert and the complementary retraction and expansion of Sahel rainfall rule the northern continent. Southern Hemisphere Africa is also no stranger to the munificence of the seasonal cycle, which brings rainfall and life to vast stretches of the Namib–Kalahari Desert in austral summer. The utility of the seasonal perspective in climate change (i.e., seasonally stratified centennial trends in precipitation and near-surface air temperature) for long-term water resource management cannot, of course, be overstated.

The centennial SAT trends are larger over the northern continent, especially in the northwestern sector and North Africa (Algeria and Libya) where they are often greater than 1.6°C century$^{-1}$. The trends are furthermore pronounced in boreal summer, amplifying the regional seasonal cycle (i.e., making hot summers even hotter and exacerbating heat-related distress). Another focal point of large SAT trends over north Africa is the region to the west of the White Nile (central-southern Sudan). For context, these SAT trends are not much smaller than the largest SAT trends over North America (e.g., Nigam et al. (2017)) that are manifest over western-central Canada in winter.

Centennial precipitation trends, especially the drying ones, are notable over the tropical continent (i.e., in the region between the Sahara and the Namib–Kalahari deserts). River-basin-wise, impressive drying trends are found in the source region of

the Niger River from spring to fall (i.e., in the local rainy seasons); the decline is impressive because it represents a 10%-25% decline in seasonal rainfall over the course of the twentieth century. Another focal point of declining rainfall is the Congo River basin, and the Blue Nile source region around Lake Tana in Ethiopia (the latter in boreal summer, the peak rainfall season).

When viewed together, the key features of the centennial drying trends can be interpreted as the southward expansion of the Sahara Desert during boreal spring to fall, or alternatively, as the equatorward retreat of the northern edge of the Sahel rainfall belt. The winter rainfall decline in northern Africa, likewise, alludes to the Sahara's northward advance. We show that the Sahara Desert has expanded significantly over the twentieth century—by 11%–18% depending on the season—using conservative estimates from the area-trend method. In winter, the desert's northward advance arises from the secular expansion of the tropics and the resulting subtropical descent (and desertification). The southward expansion in summer is linked to the SST variability in the Atlantic and Pacific basins on multidecadal time scales, through the AMO's and PDO's impact on Sahel rainfall. On centennial time scales, the summer expansion is related to aliased multidecadal variabilities and the increasing concentration of greenhouse gases and aerosol loading (Held et al. 2006).

There are other interesting features such as the increasing rainfall trends over the African Great Lakes during austral spring and summer. Are these generated from trends in regional circulation and related moisture transports (and convergence) and/or from trends in the seasonal cross-equatorial transition/position of the intertropical convergence zone (ITCZ)? The positive (negative) rainfall trends over

southern (northern) equatorial Africa, including the African Great Lakes, are not inconsistent with the latter possibility. Regardless, these questions merit further analysis.

Finally, we show the twentieth-century historical simulations produced by several climate-system models whose climate projections informed the IPCCAR5 assessment in 2013 to be devoid of realistic centennial trends in regional hydroclimate over the African continent. Projections of African climate change from these models need to be interpreted with caution. Previous work has noted the lack of improvement in CMIP5 model performance over Africa (James et al. 2018). The seasonal characterization of centennial trends in observed hydroclimate moreover accords an opportunity for evaluation of climate projection models by expanding the phase space for model vetting.

# Chapter 5: Conclusion

## 5.1 Summary

The work described in this thesis is focused on hydroclimate changes over the twentieth century based primarily on observations of temperature and precipitation. These are used to characterize century-scale *seasonal* changes in temperature and precipitation over various continental regions and attribute mechanisms for these changes. Output from historical simulations from a subset climate models included in IPCC AR5 is also examined. The common theme of the three studies constituting this thesis is the examination of centennial climate changes through a seasonal lens – a new perspective that has not yet been exploited in climate change studies.

The first study focuses on the twentieth-century trends in SAT over Northern hemisphere continents. It is found that:

- A striking seasonality exists in SAT trends over Northern Hemisphere continental regions over the twentieth century, with strong warming in winter and spring and weak warming in summer and fall.
- The SAT trend seasonality is attributed to both dynamic and thermodynamic mechanisms. Dynamically, changes in circulation enhance SAT trends in winter through thermal advection. Thermodynamically, summer SAT trends are weakened due to increased latent processes (evapotranspiration) offsetting the trends.

- The SAT trends in historical twentieth-century climate simulations informing the IPCC AR5 show varied (and often unrealistic) strength and structure, and markedly weaker seasonal variation.
- Some historical simulations showed large intra-ensemble spread of winter SAT trends, which has implications for the detection of the secular warming signal.

Based on these findings, the next study examines the seasonality in *upper-air* temperature trends over North America to further probe the mechanisms of the SAT trend seasonality. The conclusions of this chapter are:

- The seasonality in temperature trends is strongest at the surface and decreases gradually throughout the troposphere. The seasonality resumes again in the stratosphere.
- The analysis of upper-air seasonal temperature trends offers support for both mechanisms. The nature of the vertical structure of seasonality (strongest and the surface and decreasing through the troposphere) supports a surface-based hypothesis, such as the land-surface-hydroclimate interaction one described in chapter 2. However, circulation clearly plays a role, as winter trends decrease throughout the troposphere while summer trends stay roughly the same.

Seasonal hydroclimate trends were then examined in a different region of the world. Twentieth century hydroclimate trends over the African continent are also

characterized by an interesting seasonality and thus are the focus of the third study described in this thesis. It is concluded that:

- There has been an amplification of the seasonal cycle of temperature over several regions, where the strongest twentieth-century SAT trends occur in the warmest season. This was observed most prominently in Sudan and Northern Africa.
- Precipitation trends are varied but notable declining trends are found in the countries along the Gulf of Guinea, especially in the source region of the Niger River in West Africa, and in the Congo River basin. Rainfall over the African Great Lakes – one of the largest freshwater repositories – has, however increased.
- The Sahara Desert has expanded significantly over the twentieth century, by 11%-18% depending on the season, and by 10% when defined using annual rainfall. The expansion rate is sensitively dependent on the analysis period in view of the multidecadal periods of desert expansion and contraction and the stability of the rain gauge network.
- The desert expanded southward in summer, reflecting retreat of the northern edge of the Sahel rainfall belt. The desert expanded to the north in winter, indicating a potential impact of the widening of the tropics.
- Evaluation of trends in precipitation and temperature from CMIP5 historical simulations shows that modeling hydroclimate change over the African continent remains challenging, warranting caution in the development of adaptation and mitigation strategies.

## 5.2 Discussion

In section 1.4, two motivating questions were provided for the work described in this dissertation. These are re-examined here.

1. *Can examining climate changes through a seasonal lens provide a new perspective to understand past changes and predict future ones? What can the seasonal variation of long-term trends reveal about mechanisms of climate change over continental regions?*

The common theme of the work described here is the seasonal stratification of century-scale hydroclimate trends. All studies sought to answer whether this lens offers a new perspective on climate changes. In general, the focus in prior literature has been on annual-mean temperature changes, and often those averaged on the hemispheric or global scale. However, the observed twentieth-century warming reveals seasonal and regional inhomogeneities (see Figure 1.1). It was found that the seasonal perspective does offer insights into long-term climate changes, given the different roles of dynamic and thermodynamic processes in different seasons.

Furthermore, particularly in regions dependent on agriculture, developing a firm understanding of long-term changes *seasonally* has great value for society (Chapter 4). The work described in this thesis is not the first to advocate for the seasonal perspective of climate changes (see Abatzoglou et al. (2014), Balling et al. (1998) and Feng (2013)). This thesis expands on these previous studies.

Given the establishment of the seasonal perspective as valuable for understanding observed hydroclimate changes, this thesis aimed to diagnose new mechanisms for

continental warming. By exploiting the relative levels of importance of circulation features and the hydrologic cycle in summer and winter, Chapter 2 determines mechanisms important for surface warming in the different seasons. This explanation is rooted entirely in the prevalence of circulation changes in mid-latitude winter, and the dominance of the hydrologic cycle in summer. Chapter 3 reinforces the importance of both mechanisms by examining the vertical structure of seasonal trends. Finally, in Chapter 4, changes in the size of the Sahara Desert are examined seasonally. This allowed for the diagnosis of mechanisms important for expansion in different seasons. Again this is reliant on the stronger relative influence of the Hadley circulation in winter and SST variability in summer.

2. *How well do current leading climate models capture the observed seasonality in twentieth century seasonal hydroclimate trends?*

Leading climate models were examined to determine whether they capture the observed seasonality in hydroclimate changes. In general, the subset of CMIP5 climate models examined here were unable to reproduce the observed features of seasonal hydroclimate over the twentieth century, either over Northern Hemisphere continents or over the African continent. Over Northern Hemisphere continents, although none of the models capture the observed seasonality of trends, two of the examined models (NCAR-CCSM4 and MPI-ESM-LR) produce fairly realistic simulations of winter trends. Does this indicate a reasonable representation of dynamic circulation trends in these models? Elucidating the reasons for the

deficiencies in the models will require future work; this is discussed in the following section.

## 5.3 Future Work

There are several areas where further research is needed. The future research needs can be divided into three categories: further mechanistic insights into observed century-scale trends, attribution for the deficiencies observed in CMIP5 simulations in terms of this metric, and the role of internal variability.

### 5.3.1 Mechanisms of Observed Trends

While the work described here aimed at elucidating mechanisms of twentieth century hydroclimate changes, some observed changes remain unexplained. Changes in both SLP and evapotranspiration were offered as mechanistic drivers of temperature changes in different seasons in Chapter 2, but the origin of these trends remains an open question.

The spatial pattern of trends in evapotranspiration (Figure 2.10) warrants an explanation. Is the increasing summer evapotranspiration over northern North America during the twentieth century (cf. Figure 2.10) a reflection of the greening of the boreal forests from increasing $CO_2$ concentration and warming temperatures (Myneni et al. 1997; Piao et al. 2006)? Would positive evapotranspiration trends be present even in the absence of the $CO_2$ fertilization of boreal forests? Evapotranspiration has the potential to be affected by radiation, temperature, wind speed, and precipitation. A recent study focused on station-based evaporation in the

Canadian Prairies, in the proximity of where the greatest century-scale evapotranspiration are observed (Figure 2.10), found increasing trends in some regions, and related them to wind speed and vapor pressure deficit (Burn and Hesch 2007). While the trends examined in this study were on a shorter time scale (30-50 years), similar mechanisms have the potential to be important for century-scale trends and are worthy of investigation in future work. Controlled experiments with climate system models could provide insight into the mechanisms once these models begin to portray the pronounced seasonality of the century-long SAT trends seen in nature.

The mechanisms causing the observed structure of SLP changes also remain to be understood. Over the twentieth century, there was a strengthening and shift of the Aleutian Low and a weakening of the Icelandic Low in Northern Hemisphere winter (see Figure 2.12). The deepening of the Aleutian Low has been attributed to an El-Nino-like warming of the tropical Pacific SSTs resulting from global warming (Gan et al. 2017). Decreasing Arctic Sea Ice is also known to have effects on atmospheric circulation, as summarized in Budikova (2009). Over a shorter time period (1963-2012), winter SLP trends were found to be due almost entirely to internal climate variability (Deser et al. 2016). Elucidating exact mechanisms driving the observed century-scale circulation changes will require further analysis.

Finally, the mechanisms generating the seasonality and regionality of the trends in temperature and precipitation over Africa warrants further analysis. This is particularly challenging given that observational records, especially of near-surface winds, evapotranspiration and soil moisture are sparse over the African continent. Furthermore, the IPCC-class climate system models are unable to simulate the

hydroclimate trends in historical simulations (Figure 4.17), precluding their use in attribution analysis. Recent work (using the VIC model) has pointed to the importance of evapotranspiration over Africa, indicating an inverse relationship between evapotranspiration and $T_{max}$ over the western Sahel (Marshall et al. 2012). This would be worthwhile to investigate in a future study, and will require a full analysis of the energy budget in this region.

### 5.3.2 CMIP5 Deficiencies

A common result seen in the analyses discussed here is that the examined subset of CMIP5 models are not able to reproduce the observed seasonality in hydroclimate trends over the twentieth century, either over North America or over Africa. As discussed in the introduction, there are a large variety of metrics that can be used to validate climate models, with different merit depending on the question to be answered (Baker and Taylor 2016).

In the case of temperature trends over North America, the seasonality was attributed to both dynamical changes in circulation and thermodynamic changes related to evapotranspiration (see Chapter 2). An open question is why the examined models were unable to simulate this: deficiencies in representation of circulation, issues with land processes or some combination of both?

CMIP5 models have been shown to have systematic biases in evapotranspiration over many regions, including western North America, where the ensemble was found to underestimate evapotranspiration and overestimate temperature during Northern Hemisphere summer (JJA) (Mueller and Seneviratne 2014). Interestingly, these biases were found to be slightly more pronounced in CMIP5 than in the earlier

CMIP3, indicating that model development does not lead to better performance for all variables (Mueller and Seneviratne 2014). Ruiz-Barradas and Nigam (2006) found some AR4 models to have issues with representing regional hydroclimate over North America. Figure 2.14 showed that the examined CMIP5 models do not produce realistic twentieth century seasonal precipitation trends over North America, indicating that evapotranspiration trends may be biased as well.

In terms of dynamical processes in the models, Wallace et al. (2012) concluded that AR4 models were not able to simulate the anthropogenically-forced circulation trends driving strong winter warming over 1965-2000. Further analysis will involve detailed investigation of centennial trends in evapotranspiration and SLP from the historical simulations.

The situation is more complicated over the African continent, where mechanisms driving observed changes in seasonal temperature and precipitation remain unclear (see section 6.3.1). It has been noted that the CMIP project has not yielded notable improvement over Africa, making evaluation of projections difficult (James et al. 2018).

### 5.3.3 Low-Frequency Internal Variability

The role of internal variability in twentieth century hydroclimate trends is the final area that requires further research. The large intraensemble SD of century-long SAT trends in some IPCC AR5 models (e.g., GFDL-CM3; see Figure 2.7) raises interesting questions. For example, analysis of the GFDL-CM3 implies that the unforced component may be overwhelming the twentieth century secular warming signal. Kumar et al. (2013) also noted the high intra-model spread in GFDL-CM3

temperature trends, characterizing it as an exception within the CMIP5 ensemble. However, if this model is semi-realistic, especially in generation of ultra-low-frequency variability, is the century-long (1902–2014) linear trend in observed SAT—a one-member ensemble of the climate record—a reliable indicator of the secular warming signal? Can the shorter recent period (1970–2014) exhibiting even larger linear SAT trends be reasonably referred to as the ‘‘accelerated warming’’ period, given the potential for increased aliasing of the multidecadal and ultra-low-frequency variability components into the 45-yr linear trend?

For trends over a shorter period (e.g., those discussed in Chapter 3), future work is needed to separate natural from forced variability. A useful tool for this problem is large-ensembles of climate model simulations. Deser et al. (2016) recently used the CESM Large Ensemble to conclude that SLP trends over the last 50 years are due almost entirely to internal variability. Although the century-scale trends were hypothesized to be long enough to avoid aliasing of internal variability, the possibility of low-frequency internal variability must be considered in future work.

# Bibliography


Abatzoglou, J. T., and K. T. Redmond, 2007: Asymmetry between trends in spring and autumn temperature and circulation regimes over western North America. *Geophysical Research Letters*, **34,** 5.

Abatzoglou, J. T., D. E. Rupp, and P. W. Mote, 2014: Seasonal Climate Variability and Change in the Pacific Northwest of the United States. *Journal of Climate*, **27,** 2125-2142.

Alexander, L. V., and Coauthors, 2014: Summary for Policymakers. *Climate Change 2013: the Physical Science Basis*, T. F. Stocker, and Coauthors, Eds., Cambridge Univ Press, 3-29.

Allan, R., and T. Ansell, 2006: A new globally complete monthly historical gridded mean sea level pressure dataset (HadSLP2): 1850-2004. *Journal of Climate*, **19,** 5816-5842.

Archer, C. L., and K. Caldeira, 2008: Historical trends in the jet streams. *Geophysical Research Letters*, **35,** 6.

Baker, N. C., and H. P. Huang, 2014: A Comparative Study of Precipitation and Evaporation between CMIP3 and CMIP5 Climate Model Ensembles in Semiarid Regions. *Journal of Climate*, **27,** 3731-3749.

Baker, N. C., and P. C. Taylor, 2016: A Framework for Evaluating Climate Model Performance Metrics. *Journal of Climate*, **29,** 1773-1782.

Balling, R. C., P. J. Michaels, and P. C. Knappenberger, 1998: Analysis of winter and summer warming rates in gridded temperature time series. *Climate Research*, **9,** 175-181.

Bauer, P., A. Thorpe, and G. Brunet, 2015: The quiet revolution of numerical weather prediction. *Nature*, **525,** 47-55.

Baxter, S., and S. Nigam, 2015: Key Role of the North Pacific Oscillation-West Pacific Pattern in Generating the Extreme 2013/14 North American Winter. *Journal of Climate*, **28,** 8109-8117.

Becker, A., P. Finger, A. Meyer-Christoffer, B. Rudolf, K. Schamm, U. Schneider, and M. Ziese, 2013: A description of the global land-surface precipitation data products of the Global Precipitation Climatology Centre with sample applications including centennial (trend) analysis from 1901-present. *Earth System Science Data*, **5,** 71-99.

Bednarz, E. M., A. C. Maycock, N. L. Abraham, P. Braesicke, O. Dessens, and J. A. Pyle, 2016: Future Arctic ozone recovery: the importance of chemistry and dynamics. *Atmospheric Chemistry and Physics*, **16,** 12159-12176.

Biasutti, M., 2013: Forced Sahel rainfall trends in the CMIP5 archive. *Journal of Geophysical Research-Atmospheres*, **118,** 1613-1623.

Biasutti, M., and A. Giannini, 2006: Robust Sahel drying in response to late 20th century forcings. *Geophysical Research Letters*, **33,** 4.

Boe, J., 2018: Interdependency in Multimodel Climate Projections: Component Replication and Result Similarity. *Geophysical Research Letters*, **45,** 2771-2779.

Bohlinger, P., B. M. Sinnhuber, R. Ruhnke, and O. Kirner, 2014: Radiative and dynamical contributions to past and future Arctic stratospheric temperature trends. *Atmospheric Chemistry and Physics*, **14,** 1679-1688.

Braganza, K., D. J. Karoly, and J. M. Arblaster, 2004: Diurnal temperature range as an index of global climate change during the twentieth century. *Geophysical Research Letters*, **31,** 4.

Breman, H., and C. T. Dewit, 1983: RANGELAND PRODUCTIVITY AND EXPLOITATION IN THE SAHEL. *Science*, **221,** 1341-1347.

Bromwich, D. H., J. P. Nicolas, A. J. Monaghan, M. A. Lazzara, L. M. Keller, G. A. Weidner, and A. B. Wilson, 2013: Central West Antarctica among the most rapidly warming regions on Earth. *Nature Geoscience*, **6,** 139-145.

Brutsaert, W., 2006: Indications of increasing land surface evaporation during the second half of the 20th century. *Geophysical Research Letters*, **33,** 4.

Budikova, D., 2009: Role of Arctic sea ice in global atmospheric circulation: A review. *Global and Planetary Change*, **68,** 149-163.

Burn, D. H., and N. M. Hesch, 2007: Trends in evaporation for the Canadian prairies. *Journal of Hydrology*, **336,** 61-73.

Busby, J. W., K. H. Cook, E. K. Vizy, T. G. Smith, and M. Bekalo, 2014: Identifying hot spots of security vulnerability associated with climate change in Africa. *Climatic Change*, **124,** 717-731.

Canty, T., N. R. Mascioli, M. D. Smarte, and R. J. Salawitch, 2013: An empirical model of global climate - Part 1: A critical evaluation of volcanic cooling. *Atmospheric Chemistry and Physics*, **13,** 3997-4031.

Charney, J., 1975: Dynamics of deserts and drought in the Sahel. *Quarterly Journal of the Royal Meteorological Society*, **101,** 193-202.

Chou, C., J. C. H. Chiang, C. W. Lan, C. H. Chung, Y. C. Liao, and C. J. Lee, 2013: Increase in the range between wet and dry season precipitation. *Nature Geoscience*, **6,** 263-267.

Cohen, J., and Coauthors, 2014a: Recent Arctic amplification and extreme mid-latitude weather. *Nature Geoscience*, **7,** 627-637.

Cohen, N. Y., E. P. Gerber, and O. Buhler, 2014b: What Drives the Brewer-Dobson Circulation? *Journal of the Atmospheric Sciences*, **71,** 3837-3855.

Collins, J. M., 2011: Temperature Variability over Africa. *Journal of Climate*, **24,** 3649-3666.

Collins, W. J., and Coauthors, 2011: Development and evaluation of an Earth-System model-HadGEM2. *Geoscientific Model Development*, **4,** 1051-1075.

Compo, G. P., and P. D. Sardeshmukh, 2009: Oceanic influences on recent continental warming. *Climate Dynamics*, **32,** 333-342.

Compo, G. P., and Coauthors, 2011: The Twentieth Century Reanalysis Project. *Quarterly Journal of the Royal Meteorological Society*, **137,** 1-28.

Cook, K. H., and E. K. Vizy, 2015: Detection and Analysis of an Amplified Warming of the Sahara Desert. *Journal of Climate*, **28,** 6560-6580.

Cowtan, K., and R. G. Way, 2014: Coverage bias in the HadCRUT4 temperature series and its impact on recent temperature trends. *Quarterly Journal of the Royal Meteorological Society*, **140,** 1935-1944.

Dai, A., and T. M. L. Wigley, 2000: Global patterns of ENSO-induced precipitation. *Geophysical Research Letters*, **27,** 1283-1286.

Dai, A., and K. Trenberth, 2003: New Estimates of Continental Discharge and Oceanic Freshwater Transport. *Proceedings of the Symposium on Observing and Understanding the Variability of Water in Weather and Climate, 83rd Annual AMS Meeting*, 1-18.

DelSole, T., M. K. Tippett, and J. Shukla, 2011: A Significant Component of Unforced Multidecadal Variability in the Recent Acceleration of Global Warming. *Journal of Climate*, **24,** 909-926.

Delworth, T. L., and T. R. Knutson, 2000: Simulation of early 20th century global warming. *Science*, **287,** 2246-2250.

Deser, C., A. S. Phillips, and J. W. Hurrell, 2004: Pacific interdecadal climate variability: Linkages between the tropics and the North Pacific during boreal winter since 1900. *Journal of Climate*, **17,** 3109-3124.

Deser, C., L. Terray, and A. S. Phillips, 2016: Forced and Internal Components of Winter Air Temperature Trends over North America during the past 50 Years: Mechanisms and Implications. *Journal of Climate*, **29,** 2237-2258.

Dima, I. M., and J. M. Wallace, 2003: On the seasonality of the Hadley cell. *Journal of the Atmospheric Sciences*, **60,** 1522-1527.

Dong, B. W., and R. Sutton, 2015: Dominant role of greenhouse-gas forcing in the recovery of Sahel rainfall. *Nature Climate Change*, **5,** 757-U173.

Donner, L. J., and Coauthors, 2011: The Dynamical Core, Physical Parameterizations, and Basic Simulation Characteristics of the Atmospheric Component AM3 of the GFDL Global Coupled Model CM3. *Journal of Climate*, **24,** 3484-3519.

Douglass, D. H., J. R. Christy, B. D. Pearson, and S. F. Singer, 2008: A comparison of tropical temperature trends with model predictions. *International Journal of Climatology*, **28,** 1693-1701.

Dwyer, J. G., M. Biasutti, and A. H. Sobel, 2012: Projected Changes in the Seasonal Cycle of Surface Temperature. *Journal of Climate*, **25,** 6359-6374.

Easterling, D. R., and M. F. Wehner, 2009: Is the climate warming or cooling? *Geophysical Research Letters*, **36,** 3.

Ebisuzaki, W., 1997: A method to estimate the statistical significance of a correlation when the data are serially correlated. *Journal of Climate*, **10,** 2147-2153.

Eichelberger, S. J., and D. L. Hartmann, 2005: Changes in the strength of the Brewer-Dobson circulation in a simple AGCM. *Geophysical Research Letters*, **32,** 5.

Enfield, D. B., A. M. Mestas-Nunez, and P. J. Trimble, 2001: The Atlantic multidecadal oscillation and its relation to rainfall and river flows in the continental US. *Geophysical Research Letters*, **28,** 2077-2080.

Estilow, T. W., A. H. Young, and D. A. Robinson, 2015: A long-term Northern Hemisphere snow cover extent data record for climate studies and monitoring. *Earth System Science Data*, **7,** 137-142.

Evan, A. T., C. Flamant, M. Gaetani, and F. Guichard, 2016: The past, present and future of African dust. *Nature*, **531,** 493-+.

Feng, X., A. Porporato, and I. Rodriguez-Iturbe, 2013: Changes in rainfall seasonality in the tropics. *Nature Climate Change*, **3,** 811-815.

Fields, S., 2005: Spheres of influence - Continental divide - Why Africa's climate change burden is greater. *Environmental Health Perspectives*, **113,** A534-A537.

Flato, G., and Coauthors, 2014: Evaluation of Climate Models. *Climate Change 2013: the Physical Science Basis*, T. F. Stocker, and Coauthors, Eds., Cambridge Univ Press, 741-866.

Folland, C. K., T. N. Palmer, and D. E. Parker, 1986: SAHEL RAINFALL AND WORLDWIDE SEA TEMPERATURES, 1901-85. *Nature*, **320,** 602-607.

Free, M., 2011: The Seasonal Structure of Temperature Trends in the Tropical Lower Stratosphere. *Journal of Climate*, **24,** 859-866.

Free, M., D. J. Seidel, J. K. Angell, J. Lanzante, I. Durre, and T. C. Peterson, 2005: Radiosonde Atmospheric Temperature Products for Assessing Climate (RATPAC): A new data set of large-area anomaly time series. *Journal of Geophysical Research-Atmospheres*, **110,** 12.

Frierson, D. M. W., 2006: Robust increases in midlatitude static stability in simulations of global warming. *Geophysical Research Letters*, **33,** 4.

Fu, Q., S. Solomon, and P. Lin, 2010: On the seasonal dependence of tropical lower-stratospheric temperature trends. *Atmospheric Chemistry and Physics*, **10,** 2643-2653.

Fu, Q., P. Lin, S. Solomon, and D. L. Hartmann, 2015: Observational evidence of strengthening of the Brewer-Dobson circulation since 1980. *Journal of Geophysical Research-Atmospheres*, **120,** 10214-10228.

Gan, B. L., and Coauthors, 2017: On the Response of the Aleutian Low to Greenhouse Warming. *Journal of Climate*, **30,** 3907-3925.

Gao, H., T. J. Bohn, E. Podest, K. C. McDonald, and D. P. Lettenmaier, 2011: On the causes of the shrinking of Lake Chad. *Environmental Research Letters*, **6,** 7.

Garcia, R. R., and W. J. Randel, 2008: Acceleration of the Brewer-Dobson circulation due to increases in greenhouse gases. *Journal of the Atmospheric Sciences*, **65,** 2731-2739.

Garfinkel, C. I., M. M. Hurwitz, and L. D. Oman, 2015: Effect of recent sea surface temperature trends on the Arctic stratospheric vortex. *Journal of Geophysical Research-Atmospheres*, **120,** 5404-5416.

Gent, P. R., and Coauthors, 2011: The Community Climate System Model Version 4. *Journal of Climate*, **24,** 4973-4991.

Gevorgyan, A., 2014: Surface and tropospheric temperature trends in Armenia. *International Journal of Climatology*, **34,** 3559-3573.

Giannini, A., R. Saravanan, and P. Chang, 2003: Oceanic forcing of Sahel rainfall on interannual to interdecadal time scales. *Science*, **302,** 1027-1030.

Giorgetta, M. A., and Coauthors, 2013: Climate and carbon cycle changes from 1850 to 2100 in MPI-ESM simulations for the Coupled Model Intercomparison Project phase 5. *Journal of Advances in Modeling Earth Systems*, **5,** 572-597.

Gordon, C., and Coauthors, 2000: The simulation of SST, sea ice extents and ocean heat transports in a version of the Hadley Centre coupled model without flux adjustments. *Climate Dynamics*, **16,** 147-168.

Greve, P., B. Orlowsky, B. Mueller, J. Sheffield, M. Reichstein, and S. I. Seneviratne, 2014: Global assessment of trends in wetting and drying over land. *Nature Geoscience*, **7,** 716-721.

Guan, B., and S. Nigam, 2008: Pacific sea surface temperatures in the twentieth century: An evolution-centric analysis of variability and trend. *Journal of Climate*, **21,** 2790-2809.

——, 2009: Analysis of Atlantic SST Variability Factoring Interbasin Links and the Secular Trend: Clarified Structure of the Atlantic Multidecadal Oscillation. *Journal of Climate*, **22,** 4228-4240.

Hagos, S. M., and K. H. Cook, 2008: Ocean warming and late-twientieth-century Sahel drought and recovery. *Journal of Climate*, **21,** 3797-3814.

Haimberger, L., 2007: Homogenization of radiosonde temperature time series using innovation statistics. *Journal of Climate*, **20,** 1377-1403.

Haimberger, L., C. Tavolato, and S. Sperka, 2012: Homogenization of the Global Radiosonde Temperature Dataset through Combined Comparison with Reanalysis Background Series and Neighboring Stations. *Journal of Climate*, **25,** 8108-8131.

Hansen, J., R. Ruedy, M. Sato, and K. Lo, 2010: GLOBAL SURFACE TEMPERATURE CHANGE. *Reviews of Geophysics*, **48,** 29.

Harris, I., P. D. Jones, T. J. Osborn, and D. H. Lister, 2014: Updated high-resolution grids of monthly climatic observations - the CRU TS3.10 Dataset. *International Journal of Climatology*, **34,** 623-642.

Hartmann, D. L., and Coauthors, 2014: Observations: Atmosphere and Surface. *Climate Change 2013: the Physical Science Basis*, T. F. Stocker, and Coauthors, Eds., Cambridge Univ Press, 159-254.

Hassler, B., P. J. Young, R. W. Portmann, G. E. Bodeker, J. S. Daniel, K. H. Rosenlof, and S. Solomon, 2013: Comparison of three vertically resolved ozone data sets: climatology, trends and radiative forcings. *Atmospheric Chemistry and Physics*, **13,** 5533-5550.

Held, I. M., T. L. Delworth, J. Lu, K. L. Findell, and T. R. Knutson, 2006: Simulation of Sahel drought in the 20th and 21st centuries (vol 102, pg 17891, 2005). *Proceedings of the National Academy of Sciences of the United States of America*, **103,** 1152-1153.

Hoerling, M., J. Hurrell, J. Eischeid, and A. Phillips, 2006: Detection and attribution of twentieth-century northern and southern African rainfall change. *Journal of Climate*, **19,** 3989-4008.

Hoskins, B., 1996: On the existence and strength of the summer subtropical anticyclones - Bernhard Haurwitz memorial lecture. *Bulletin of the American Meteorological Society*, **77,** 1287-1292.

Hulme, M., R. Doherty, T. Ngara, M. New, and D. Lister, 2001: African climate change: 1900-2100. *Climate Research*, **17,** 145-168.

Ivy, D. J., S. Solomon, and H. E. Rieder, 2016: Radiative and Dynamical Influences on Polar Stratospheric Temperature Trends. *Journal of Climate*, **29,** 4927-4938.

James, I. N., 2003: Hadley Circulation. *Encyclopedia of Atmospheric Sciences*, J. R. Holton, Ed., Elsevier, 919-929.

James, R., and Coauthors, 2018: EVALUATING CLIMATE MODELS WITH AN AFRICAN LENS. *Bulletin of the American Meteorological Society*, **99,** 313-336.

Jones, P., 2016: The Reliability of Global and Hemispheric Surface Temperature Records. *Advances in Atmospheric Sciences*, **33,** 269-282.

Jones, P. D., D. H. Lister, T. J. Osborn, C. Harpham, M. Salmon, and C. P. Morice, 2012: Hemispheric and large-scale land-surface air temperature variations: An extensive revision and an update to 2010. *Journal of Geophysical Research-Atmospheres*, **117,** 29.

Kalnay, E., and Coauthors, 1996: The NCEP/NCAR 40-year reanalysis project. *Bulletin of the American Meteorological Society*, **77,** 437-471.

Karl, T. R., R. W. Knight, and J. R. Christy, 1994: GLOBAL AND HEMISPHERIC TEMPERATURE TRENDS - UNCERTAINTIES RELATED TO INADEQUATE SPATIAL SAMPLING. *Journal of Climate*, **7,** 1144-1163.

Kavvada, A., A. Ruiz-Barradas, and S. Nigam, 2013: AMO's structure and climate footprint in observations and IPCC AR5 climate simulations. *Climate Dynamics*, **41,** 1345-1364.

Knight, J. R., C. K. Folland, and A. A. Scaife, 2006: Climate impacts of the Atlantic Multidecadal Oscillation. *Geophysical Research Letters*, **33,** 4.

Knutti, R., 2010: The end of model democracy? *Climatic Change*, **102,** 395-404.

Knutti, R., and J. Sedlacek, 2013: Robustness and uncertainties in the new CMIP5 climate model projections. *Nature Climate Change*, **3,** 369-373.

Knutti, R., D. Masson, and A. Gettelman, 2013: Climate model genealogy: Generation CMIP5 and how we got there. *Geophysical Research Letters*, **40,** 1194-1199.

Kothawale, D. R., and H. N. Singh, 2017: Recent trends in tropospheric temperature over India during the period 1971-2015. *Earth and Space Science*, **4,** 240-246.

Kumar, S., V. Merwade, J. L. Kinter, and D. Niyogi, 2013: Evaluation of Temperature and Precipitation Trends and Long-Term Persistence in CMIP5 Twentieth-Century Climate Simulations. *Journal of Climate*, **26,** 4168-4185.

Kusunoki, S., T. Nakaegawa, O. Arakawa, and I. Yagai, 2009: Simulations of Land-surface Air Temperature and Land Precipitation in the Twentieth Century by the MJ98 AGCM. *Journal of the Meteorological Society of Japan*, **87,** 473-495.

Lanzante, J. R., S. A. Klein, and D. J. Seidel, 2003a: Temporal homogenization of monthly radiosonde temperature data. Part II: Trends, sensitivities, and MSU comparison. *Journal of Climate*, **16,** 241-262.

——, 2003b: Temporal homogenization of monthly radiosonde temperature data. Part I: Methodology. *Journal of Climate*, **16,** 224-240.

Lau, N. C., 1979: OBSERVED STRUCTURE OF TROPOSPHERIC STATIONARY WAVES AND THE LOCAL BALANCES OF VORTICITY AND HEAT. *Journal of the Atmospheric Sciences*, **36,** 996-1016.

Lawrence, D. M., and Coauthors, 2012: The CCSM4 Land Simulation, 1850-2005: Assessment of Surface Climate and New Capabilities. *Journal of Climate*, **25,** 2240-2260.

Lean, J. L., and D. H. Rind, 2009: How will Earth's surface temperature change in future decades? *Geophysical Research Letters*, **36,** 5.

Lewis, S. C., and D. J. Karoly, 2013: Evaluation of Historical Diurnal Temperature Range Trends in CMIP5 Models. *Journal of Climate*, **26,** 9077-9089.

Li, F., J. Austin, and J. Wilson, 2008: The strength of the Brewer-Dobson circulation in a changing climate: Coupled chemistry-climate model simulations. *Journal of Climate*, **21,** 40-57.

Lindzen, R. S., and A. Y. Hou, 1988: HADLEY CIRCULATIONS FOR ZONALLY AVERAGED HEATING CENTERED OFF THE EQUATOR. *Journal of the Atmospheric Sciences*, **45,** 2416-2427.

Linkin, M. E., and S. Nigam, 2008: The north pacific oscillation-west Pacific teleconnection pattern: Mature-phase structure and winter impacts. *Journal of Climate*, **21,** 1979-1997.

Lu, J. H., and M. Cai, 2009: Seasonality of polar surface warming amplification in climate simulations. *Geophysical Research Letters*, **36,** 6.

Maidment, R. I., R. P. Allan, and E. Black, 2015: Recent observed and simulated changes in precipitation over Africa. *Geophysical Research Letters*, **42,** 8155-8164.

Manabe, S., and R. J. Stouffer, 1980: SENSITIVITY OF A GLOBAL CLIMATE MODEL TO AN INCREASE OF CO2 CONCENTRATION IN THE ATMOSPHERE. *Journal of Geophysical Research-Oceans*, **85,** 5529-5554.

Mantua, N. J., S. R. Hare, Y. Zhang, J. M. Wallace, and R. C. Francis, 1997: A Pacific interdecadal climate oscillation with impacts on salmon production. *Bulletin of the American Meteorological Society*, **78,** 1069-1079.

Marshall, M., C. Funk, and J. Michaelsen, 2012: Examining evapotranspiration trends in Africa. *Climate Dynamics*, **38,** 1849-1865.

Martin, E. R., and C. D. Thorncroft, 2014: The impact of the AMO on the West African monsoon annual cycle. *Quarterly Journal of the Royal Meteorological Society*, **140,** 31-46.

McKinnon, K. A., A. Poppick, E. Dunn-Sigouin, and C. Deser, 2017: An "Observational Large Ensemble" to Compare Observed and Modeled Temperature Trend Uncertainty due to Internal Variability. *Journal of Climate*, **30,** 7585-7598.

McLandress, C., and T. G. Shepherd, 2009: Simulated Anthropogenic Changes in the Brewer-Dobson Circulation, Including Its Extension to High Latitudes. *Journal of Climate*, **22,** 1516-1540.

Meehl, G. A., J. M. Arblaster, and G. Branstator, 2012: Mechanisms Contributing to the Warming Hole and the Consequent US East-West Differential of Heat Extremes. *Journal of Climate*, **25,** 6394-6408.

Meehl, G. A., C. Covey, B. McAvaney, M. Latif, and R. J. Stouffer, 2005: Overview of the Coupled Model Intercomparison Project. *Bulletin of the American Meteorological Society*, **86,** 89-93.

Meehl, G. A., W. M. Washington, C. M. Ammann, J. M. Arblaster, T. M. L. Wigley, and C. Tebaldi, 2004: Combinations of natural and anthropogenic forcings in twentieth-century climate. *Journal of Climate*, **17,** 3721-3727.

Meehl, G. A., and Coauthors, 2009: DECADAL PREDICTION Can It Be Skillful? *Bulletin of the American Meteorological Society*, **90,** 1467-1485.

——, 2014: DECADAL CLIMATE PREDICTION An Update from the Trenches. *Bulletin of the American Meteorological Society*, **95,** 243-267.

Mitchell, D. M., 2016: Attributing the forced components of observed stratospheric temperature variability to external drivers. *Quarterly Journal of the Royal Meteorological Society*, **142,** 1041-1047.

Mitchell, T. P., and J. M. Wallace, 1992: THE ANNUAL CYCLE IN EQUATORIAL CONVECTION AND SEA-SURFACE TEMPERATURE. *Journal of Climate*, **5,** 1140-1156.

Mohino, E., S. Janicot, and J. Bader, 2011: Sahel rainfall and decadal to multi-decadal sea surface temperature variability. *Climate Dynamics*, **37,** 419-440.

Mote, P. W., 2003: Trends in temperature and precipitation in the Pacific northwest during the twentieth century. *Northwest Science*, **77,** 271-282.

Mueller, B., and S. I. Seneviratne, 2014: Systematic land climate and evapotranspiration biases in CMIP5 simulations. *Geophysical Research Letters*, **41,** 128-134.

Murphy, J. M., D. M. H. Sexton, D. N. Barnett, G. S. Jones, M. J. Webb, and D. A. Stainforth, 2004: Quantification of modelling uncertainties in a large ensemble of climate change simulations. *Nature*, **430,** 768-772.

Myhre, G., and Coauthors, 2014: Anthropogenic and Natural Radiative Forcing. *Climate Change 2013: the Physical Science Basis*, T. F. Stocker, and Coauthors, Eds., Cambridge Univ Press, 659-740.

Myneni, R. B., C. D. Keeling, C. J. Tucker, G. Asrar, and R. R. Nemani, 1997: Increased plant growth in the northern high latitudes from 1981 to 1991. *Nature*, **386,** 698-702.

Niang, I., and Coauthors, 2014: Africa. *Climate Change 2014: Impacts, Adaptation, and Vulnerability, Pt B: Regional Aspects: Working Group Ii Contribution to the Fifth Assessment Report of the Intergovernmental Panel on Climate Change*, V. R. Barros, and Coauthors, Eds., Cambridge Univ Press, 1199-1265.

Nicholson, S., 2000: Land surface processes and Sahel climate. *Reviews of Geophysics*, **38,** 117-139.

Nicholson, S. E., 2001: Climatic and environmental change in Africa during the last two centuries. *Climate Research*, **17,** 123-144.

Nicholson, S. E., and E. Kim, 1997: The relationship of the El Nino Southern oscillation to African rainfall. *International Journal of Climatology*, **17,** 117-135.

Nigam, S., and Y. Chao, 1996: Evolution dynamics of tropical ocean-atmosphere annual cycle variability. *Journal of Climate*, **9,** 3187-3205.

Nigam, S., and A. Ruiz-Barradas, 2006: Seasonal hydroclimate variability over north America in global and regional reanalyses and AMIP simulations: Varied representation. *Journal of Climate*, **19,** 815-837.

Nigam, S., and S. C. Chan, 2009: On the Summertime Strengthening of the Northern Hemisphere Pacific Sea Level Pressure Anticyclone. *Journal of Climate*, **22,** 1174-1192.

Nigam, S., and A. Ruiz-Barradas, 2016: Key role of the Atlantic multidecadal oscillation in twentieth century drought and wet periods over the US Great Plains and the Sahel. *Dynamics and Predictability of Large-Scale, High-Impact Weather and Climate Events*, J. Li, R. Swinbank, H. Volkert, and R. Grotjahn, Eds., Cambridge University Press, 255-270.

Nigam, S., B. Guan, and A. Ruiz-Barradas, 2011: Key role of the Atlantic Multidecadal Oscillation in 20th century drought and wet periods over the Great Plains. *Geophysical Research Letters*, **38,** 6.

Nigam, S., N. P. Thomas, A. Ruiz-Barradas, and S. J. Weaver, 2017: Striking Seasonality in the Secular Warming of the Northern Continents: Structure and Mechanisms. *Journal of Climate*, **30,** 6521-6541.

Okonkwo, C., and Coauthors, 2015: Combined effect of El Nino southern oscillation and Atlantic multidecadal oscillation on Lake Chad level variability. *Cogent Geoscience*, **1,** 18.

Omondi, P., L. A. Ogallo, R. Anyah, J. M. Muthama, and J. Ininda, 2013: Linkages between global sea surface temperatures and decadal rainfall variability over Eastern Africa region. *International Journal of Climatology*, **33,** 2082-2104.

Oort, A. H., and J. J. Yienger, 1996: Observed interannual variability in the Hadley circulation and its connection to ENSO. *Journal of Climate*, **9,** 2751-2767.

Pan, Z. T., R. W. Arritt, E. S. Takle, W. J. Gutowski, C. J. Anderson, and M. Segal, 2004: Altered hydrologic feedback in a warming climate introduces a "warming hole". *Geophysical Research Letters*, **31,** 4.

Philander, S. G. H., and Y. Chao, 1991: ON THE CONTRAST BETWEEN THE SEASONAL CYCLES OF THE EQUATORIAL ATLANTIC AND PACIFIC OCEANS. *Journal of Physical Oceanography*, **21,** 1399-1406.

Piao, S. L., P. Friedlingstein, P. Ciais, L. M. Zhou, and A. P. Chen, 2006: Effect of climate and CO2 changes on the greening of the Northern Hemisphere over the past two decades. *Geophysical Research Letters*, **33,** 6.

Ramaswamy, V., and Coauthors, 2001: Stratospheric temperature trends: Observations and model simulations. *Reviews of Geophysics*, **39,** 71-122.

Randel, W. J., and Coauthors, 2009: An update of observed stratospheric temperature trends. *Journal of Geophysical Research-Atmospheres*, **114,** 21.

Rayner, N. A., and Coauthors, 2003: Global analyses of sea surface temperature, sea ice, and night marine air temperature since the late nineteenth century. *Journal of Geophysical Research-Atmospheres*, **108,** 37.

Redmond, K. T., and J. T. Abatzoglou, 2014: Current Climate and Recent Trends. *Climate Change in North America*, G. Ohring, Ed., Springer Int Publishing Ag, 53-94.

Robeson, S. M., C. J. Willmott, and P. D. Jones, 2014: Trends in hemispheric warm and cold anomalies. *Geophysical Research Letters*, **41,** 9065-9071.

Rohde, R., and Coauthors, 2013: A New Estimate of the Average Earth Surface Land Temperature Spanning 1753 to 2011. *Geoinformatics & Geostatistics: An Overview*, **1,** 1-7.

Rowell, D. P., B. B. B. Booth, S. E. Nicholson, and P. Good, 2015: Reconciling Past and Future Rainfall Trends over East Africa. *Journal of Climate*, **28,** 9768-9788.

Ruiz-Barradas, A., and S. Nigam, 2005: Warm season rainfall variability over the US great plains in observations, NCEP and ERA-40 reanalyses, and NCAR and NASA atmospheric model simulations. *Journal of Climate*, **18,** 1808-1830.

——, 2006: IPCC's twentieth-century climate simulations: Varied representations of north American hydroclimate variability. *Journal of Climate*, **19,** 4041-4058.

Santer, B. D., and Coauthors, 2000: Statistical significance of trends and trend differences in layer-average atmospheric temperature time series. *Journal of Geophysical Research-Atmospheres*, **105,** 7337-7356.

——, 2013: Human and natural influences on the changing thermal structure of the atmosphere. *Proceedings of the National Academy of Sciences of the United States of America*, **110,** 17235-17240.

——, 2008: Consistency of modelled and observed temperature trends in the tropical troposphere. *International Journal of Climatology*, **28,** 1703-1722.

Sardeshmukh, P. D., G. P. Compo, and C. Penland, 2000: Changes of probability associated with El Nino. *Journal of Climate*, **13,** 4268-4286.

Schlesinger, M. E., and N. Ramankutty, 1994: AN OSCILLATION IN THE GLOBAL CLIMATE SYSTEM OF PERIOD 65-70 YEARS. *Nature*, **367,** 723-726.

Schneider, U., A. Becker, P. Finger, A. Meyer-Christoffer, M. Ziese, and B. Rudolf, 2014: GPCC's new land surface precipitation climatology based on quality-controlled in situ data and its role in quantifying the global water cycle. *Theoretical and Applied Climatology*, **115,** 15-40.

Schreck, C. J., and F. H. M. Semazzi, 2004: Variability of the recent climate of eastern Africa. *International Journal of Climatology*, **24,** 681-701.

Screen, J. A., C. Deser, and I. Simmonds, 2012: Local and remote controls on observed Arctic warming. *Geophysical Research Letters*, **39,** 5.

Seidel, D. J., Q. Fu, W. J. Randel, and T. J. Reichler, 2008: Widening of the tropical belt in a changing climate. *Nature Geoscience*, **1,** 21-24.

Seidel, D. J., N. P. Gillett, J. R. Lanzante, K. P. Shine, and P. W. Thorne, 2011: Stratospheric temperature trends: our evolving understanding. *Wiley Interdisciplinary Reviews-Climate Change*, **2,** 592-616.

Serreze, M. C., A. P. Barrett, J. C. Stroeve, D. N. Kindig, and M. M. Holland, 2009: The emergence of surface-based Arctic amplification. *Cryosphere*, **3,** 11-19.

Sheffield, J., and E. F. Wood, 2007: Characteristics of global and regional drought, 1950-2000: Analysis of soil moisture data from off-line simulation of the terrestrial hydrologic cycle. *Journal of Geophysical Research-Atmospheres*, **112,** 21.

Sheffield, J., G. Goteti, and E. F. Wood, 2006: Development of a 50-year high-resolution global dataset of meteorological forcings for land surface modeling. *Journal of Climate*, **19,** 3088-3111.

Sherwood, S. C., and N. Nishant, 2015: Atmospheric changes through 2012 as shown by iteratively homogenized radiosonde temperature and wind data (IUKv2). *Environmental Research Letters*, **10,** 7.

Solomon, S., J. Haskins, D. J. Ivy, and F. Min, 2014: Fundamental differences between Arctic and Antarctic ozone depletion. *Proceedings of the National Academy of Sciences of the United States of America*, **111,** 6220-6225.

Steinman, B. A., M. E. Mann, and S. K. Miller, 2015: Atlantic and Pacific multidecadal oscillations and Northern Hemisphere temperatures. *Science*, **347,** 988-991.

Stephens, G. L., and Coauthors, 2012: An update on Earth's energy balance in light of the latest global observations. *Nature Geoscience*, **5,** 691-696.

Stine, A. R., and P. Huybers, 2012: Changes in the Seasonal Cycle of Temperature and Atmospheric Circulation. *Journal of Climate*, **25,** 7362-7380.

Stine, A. R., P. Huybers, and I. Y. Fung, 2009: Changes in the phase of the annual cycle of surface temperature. *Nature*, **457,** 435-U431.

Stocker, T. F., and Coauthors, 2014: Technical Summary. *Climate Change 2013: the Physical Science Basis*, T. F. Stocker, and Coauthors, Eds., Cambridge Univ Press, 33-115.

Stolpe, M. B., I. Medhaug, and R. Knutti, 2017: Contribution of Atlantic and Pacific Multidecadal Variability to Twentieth-Century Temperature Changes. *Journal of Climate*, **30,** 6279-6295.

Taylor, K. E., R. J. Stouffer, and G. A. Meehl, 2012: AN OVERVIEW OF CMIP5 AND THE EXPERIMENT DESIGN. *Bulletin of the American Meteorological Society*, **93,** 485-498.

Thomas, N., and S. Nigam, 2018: Twentieth-Century Climate Change over Africa: Seasonal Hydroclimate Trends and Sahara Desert Expansion. *Journal of Climate*, **31,** 3349-3370.

Thompson, D. W. J., and S. Solomon, 2005: Recent stratospheric climate trends as evidenced in radiosonde data: Global structure and tropospheric linkages. *Journal of Climate*, **18,** 4785-4795.

Thompson, D. W. J., J. M. Wallace, P. D. Jones, and J. J. Kennedy, 2009: Identifying Signatures of Natural Climate Variability in Time Series of Global-Mean Surface Temperature: Methodology and Insights. *Journal of Climate*, **22,** 6120-6141.

Thorncroft, C.D., H. Nguyen, C.D. Zhang, P. Peyrille, 2011: Annual cycle of the West African monsoon: Regional circulations and associated water vapour transport. *Q.J.R. Meteorol. Soc.*, **137**, 129-147.

Thorne, P. W., J. R. Lanzante, T. C. Peterson, D. J. Seidel, and K. P. Shine, 2011: Tropospheric temperature trends: history of an ongoing controversy. *Wiley Interdisciplinary Reviews-Climate Change*, **2,** 66-88.

Thorne, P. W., D. E. Parker, S. F. B. Tett, P. D. Jones, M. McCarthy, H. Coleman, and P. Brohan, 2005: Revisiting radiosonde upper air temperatures from 1958 to 2002. *Journal of Geophysical Research-Atmospheres*, **110,** 17.

Trenberth, K. E., 2011: Changes in precipitation with climate change. *Climate Research*, **47,** 123-138.

Trenberth, K. E., and P. D. Jones, 2007: Observations: Surface and Atmospheric Climate Change. *Climate Change 2007: the Physical Science Basis*, S. Solomon, and Coauthors, Eds., Cambridge Univ Press, 235-336.

Tucker, C. J., and S. E. Nicholson, 1999: Variations in the size of the Sahara Desert from 1980 to 1997. *Ambio*, **28,** 587-591.

Tucker, C. J., H. E. Dregne, and W. W. Newcomb, 1991: EXPANSION AND CONTRACTION OF THE SAHARA DESERT FROM 1980 TO 1990. *Science*, **253,** 299-301.

Uppala, S. M., and Coauthors, 2005: The ERA-40 re-analysis. *Quarterly Journal of the Royal Meteorological Society*, **131,** 2961-3012.

Villamayor, J., and E. Mohino, 2015: Robust Sahel drought due to the Interdecadal Pacific Oscillation in CMIP5 simulations. *Geophysical Research Letters*, **42,** 1214-1222.

Vizy, E. K., and K. H. Cook, 2017: Seasonality of the Observed Amplified Sahara Warming Trend and Implications for Sahel Rainfall. *Journal of Climate*, **30,** 3073-3094.

Wallace, J. M., Y. Zhang, and J. A. Renwick, 1995: DYNAMIC CONTRIBUTION TO HEMISPHERIC MEAN TEMPERATURE TRENDS. *Science*, **270,** 780-783.

Wallace, J. M., Q. Fu, B. V. Smoliak, P. Lin, and C. M. Johanson, 2012: Simulated versus observed patterns of warming over the extratropical Northern Hemisphere continents during the cold season. *Proceedings of the National Academy of Sciences of the United States of America*, **109,** 14337-14342.

Wang, H. L., S. Schubert, M. Suarez, J. Y. Chen, M. Hoerling, A. Kumar, and P. Pegion, 2009: Attribution of the Seasonality and Regionality in Climate Trends over the United States during 1950-2000. *Journal of Climate*, **22,** 2571-2590.

Weare, B. C., and J. S. Nasstrom, 1982: EXAMPLES OF EXTENDED EMPIRICAL ORTHOGONAL FUNCTION ANALYSES. *Monthly Weather Review*, **110,** 481-485.

Williams, A. P., and C. Funk, 2011: A westward extension of the warm pool leads to a westward extension of the Walker circulation, drying eastern Africa. *Climate Dynamics*, **37,** 2417-2435.

Willmott, C. J., and K. Matsuura, 2015: Terrestrial Water Budget Data Archive: Monthly Time Series (1900-2014). 3.01 ed.

Willmott, C. J., C. M. Rowe, and Y. Mintz, 1985: CLIMATOLOGY OF THE TERRESTRIAL SEASONAL WATER CYCLE. *Journal of Climatology*, **5,** 589-606.

Young, P. J., K. H. Rosenlof, S. Solomon, S. C. Sherwood, Q. Fu, and J. F. Lamarque, 2012: Changes in Stratospheric Temperatures and Their Implications for Changes in the Brewer Dobson Circulation, 1979-2005. *Journal of Climate*, **25,** 1759-1772.

Zhang, L. X., and T. J. Zhou, 2013: A comparison of tropospheric temperature changes over China revealed by multiple data sets. *Journal of Geophysical Research-Atmospheres*, **118,** 4217-4230.

Zhang, R., and T. L. Delworth, 2006: Impact of Atlantic multidecadal oscillations on India/Sahel rainfall and Atlantic hurricanes. *Geophysical Research Letters*, **33,** 5.

Zhang, R., T. L. Delworth, and I. M. Held, 2007: Can the Atlantic Ocean drive the observed multidecadal variability in Northern Hemisphere mean temperature? *Geophysical Research Letters*, **34,** 6.

Zhang, Y., J. M. Wallace, and D. S. Battisti, 1997: ENSO-like interdecadal variability: 1900-93. *Journal of Climate*, **10,** 1004-1020.

Zhou, L. M., 2016: Desert Amplification in a Warming Climate. *Scientific Reports*, **6,** 13.